Modeling the Coupled Cyclic Translational and Rotational Responses of Skew Bridge Abutment Backfills

Nojoumi, Seyedali

2015

UNIVERSITY OF CALIFORNIA

Los Angeles

Modeling the Coupled Cyclic Translational and Rotational Responses of Skew Bridge Abutment Backfills

A dissertation submitted in partial satisfaction of the

requirements for the degree Doctor of Philosophy

in Civil Engineering

by

Seyedali Nojoumi

2016

ABSTRACT OF THE DISSERTATION

Modeling the Coupled Cyclic Translational and Rotational Responses of Skew Bridge Abutment Backfills

by

Seyedali Nojoumi

Doctor of Philosophy in Civil Engineering

University of California, Los Angeles, 2016

Professor Ertugrul Taciroglu, Chair

This study presents a macroelement model that can represent the passive reactions of the backfill of a skew abutment and the gapping behavior between the backwall and the bridge deck. The model is calibrated against e finite element models that were validated using data from field tests. The macroelement model is largely based on physical parameters including the backfill soil's internal friction angle and cohesion, backwall height, and skew angle. It accurately produces the normal and tangential reactions as well as the moment causes by the backwall rotation and its formulation is based on basic concepts of classical rate-independent plasticity. The model is computationally efficient, and thus, it is amenable to repetitive nonlinear time-history analyses required for performance-based seismic design.

The dissertation of Seyedali Nojoumi is approved.

Jonathan P. Stewart

Scott J. Brandenberg

Christopher S. Lynch

Ertugrul Taciroglu, Committee Chair

University of California, Los Angeles

2016

To:

My parents Latifeh and Fariborz, my beloved Mikaela, and my sister Lobat

پیشکش به:

مادر مهربانم لطیفه، پدرم فریبرز، دلبرم میکیلا، و خواهرم لعبت

Table of Contents

List of Figures

1.

2.

3.

4.

5.

List of Tables

2.

3.

4.

Acknowledgments

This study was funded in part by the California Department of Transportation (Caltrans) under Contract No. 59A0247 (and amendments thereto), and by Pacific Earthquake Engineering Research (PEER) Transportation Research Program under Grant No. UCLA-45782. I am grateful for this this financial support as well as various UCLA fellowships, and Teaching Assistant appointments throughout my Ph.D. studies.

Chapter 1

Introduction

1. Introduction

1.1 Overview and motivation for research

Abutments are bridge-supporting structures at the interface of the bridge deck and the soil embankment. Fig. 1.1 (left) displays the components of a seat-type abutment, which is a typical configuration in California, the United States in general, and many parts of the world (see, for example, NBI, 2002; Kawashima *et al.*, 2011; Mitoulis, 2012; Zakeri *et al.*, 2014). During strong seismic events, longitudinal motion of the bridge causes a collision between the deck and the abutment backwall—which is lightly reinforced and is designed to break—and plastic deformations are induced in the backfill. This mechanism is intended to dissipate energy, and concentrate or limit the seismic damage to the abutments (Caltrans SDC, 2010). Reversals of inertial forces can cause the deck to unseat from the abutment, and thus, sufficient seat-length is required. Seat-type abutments also feature exterior shear keys that are used to counter possible transverse deck movements. They are proportioned and detailed to act as fuses that will break off under the design earthquake (Kaviani *et al.*, 2014).

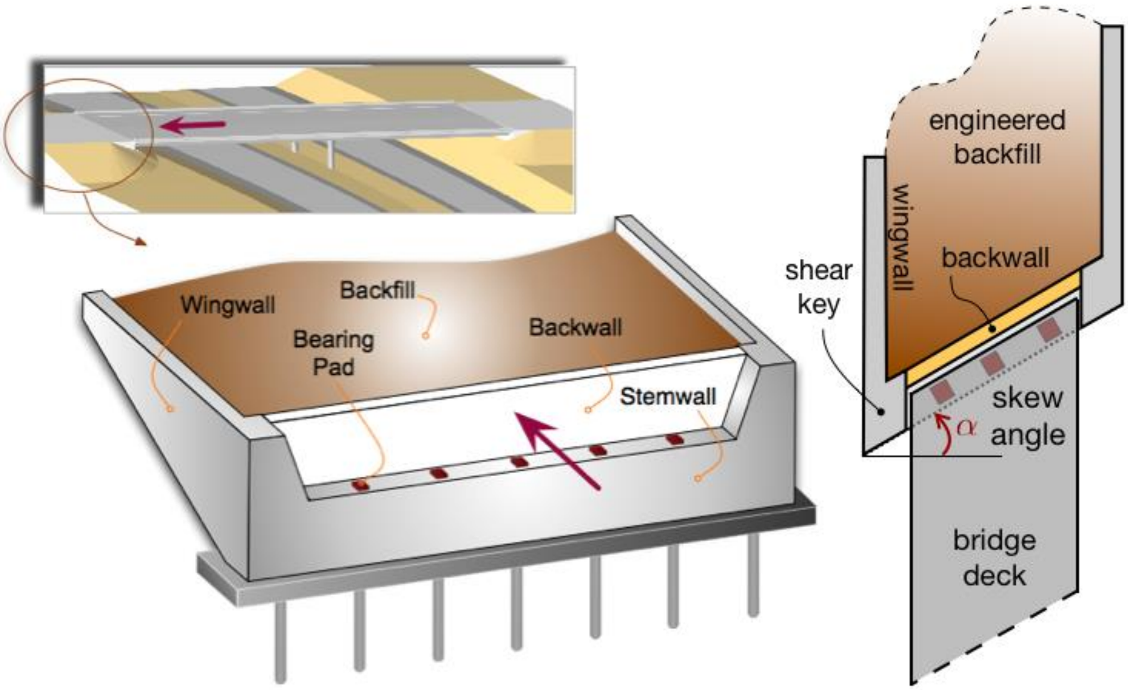

Fig. 1.1. The anatomy of a seat-type abutment (left), and plan view of a skew configuration (right).

The abutment-deck interaction becomes even more complex for "skew bridges" (Fig. 1.1, right). Bridges with skew-angled abutments are constructed to accommodate geometric constraints resulting from the alignment of a waterway or roadway crossing that occurs at an angle that is different from 90 degrees. A significant number of bridges are constructed with some skew (NBI, 2002).

The typical responses of a skew bridge abutment are schematically illustrated in Fig. 1.2, wherein the abutment reaction is decomposed into its normal and tangential components relative to the backwall. In the absence of skew, significant soil-backwall interaction occurs *only* in the normal. However, due to the interaction of the bridge superstructure with its abutment, seismic demands on the skew abutment are likely to include lateral translations coupled with torsional rotations in many cases (Fig. 1.2, middle). To date, *no validated or verified model has been proposed for predicting this backfill reaction under the full range of possible abutment motions*.

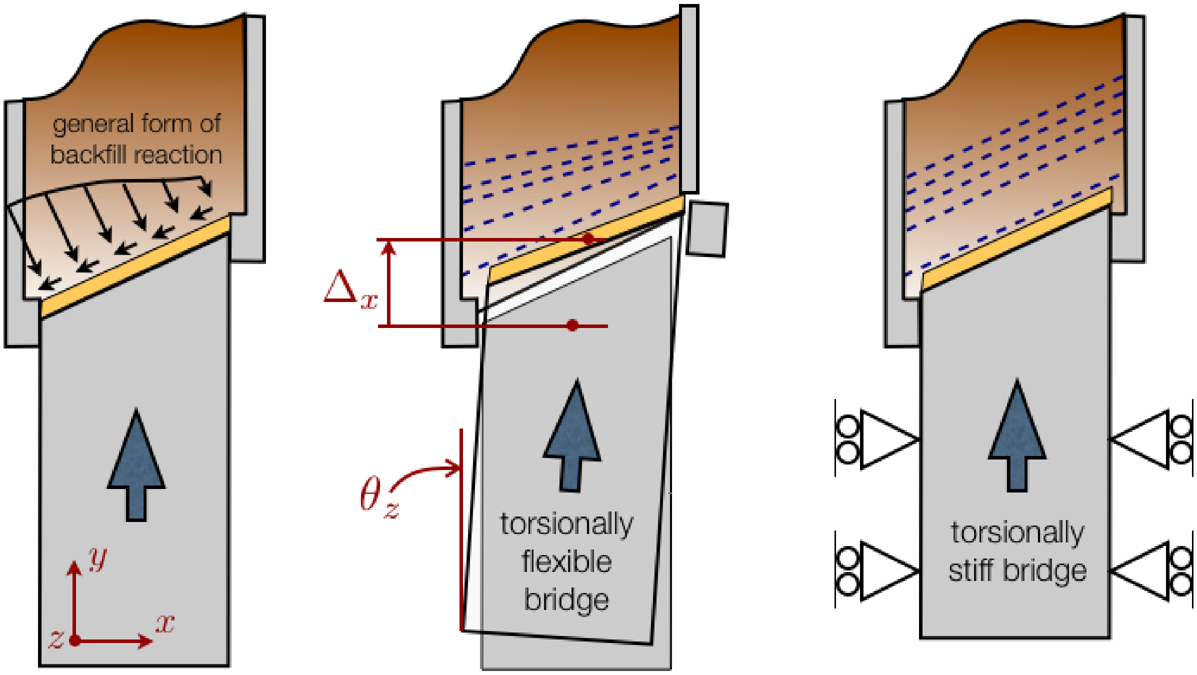

Fig. 1.2. Tangential and normal components of the backfill reaction (left). Deformation demands from translation and torsional rotations for torsionally flexible (middle) and stiff bridges (right).

While there are only scarce and very preliminary experimental results on skew abutments, there have been significant efforts undertaken to characterize the nonlinear load-deformation characteristics of *non-skew abutments* having cohesive or granular backfills (e.g., Romstad *et al.*, 1995; Shamsabadi *et al.*, 2007; Stewart *et al.*, 2007). This inventory of data has indeed been utilized directly to develop design/assessment guidelines for non-skew backwalls (for an overview see, for example, Shamsabadi *et al.*, 2010). Only recently, tests on reduced-scale models by Rollins and Jessee (2013) have offered quantified findings on the behavior of skew abutments—they tested skew abutments under only lateral translations (i.e., the case illustrated in Fig. 1.2, right). Additional testing is needed in order to examine the normal and tangential responses as a function of the skew angle, as well as demands associated with lateral displacements and torsional rotations of the backwall.

Current engineering practice for seismic design of bridges (Caltrans, 2006) is based on the displacement-performance philosophy, for which a complete horizontal load-displacement backbone curve of the abutment backwall is needed. There have been numerous attempts to characterize the response of skew bridges (for recent work in this area, see, for example, Abdel-Mohti and Pekcan, 2008; Kalantari and Amjadian, 2010; Dimitrakopoulos, 2011; Kaviani *et al.*, 2012, 2014; Omrani *et al.*, 2015). However, none the existing studies made use of a veritable model for the passive response of the skew abutment; instead, they relied on heuristic models.

1.2 Objectives and approach

Given the observations provided in the previous section, *the main objective of this research is to develop a model for skew abutments and to verify, improve, and generalize its predictive capabilities as much as possible.* The primary (and essential) tool that will be adopted for developing an accurate model for skew abutments is the three-dimensional finite element (FE) method. Similar studies were conducted for straight abutments using two-dimensional (plane-strain) FE models (see, for example, Shamsabadi *et al.*, 2010). Because the expected response of a skew abutment includes rotation about the vertical axis, only three-dimensional finite element models can be used in the present pursuit.

On that note, it is important to state here that while calibrated and validated continuum finite element models are highly valuable in their own right, they are too complex for routine analysis and design evaluations by practicing engineers. Nonlinear time-history analyses of a complete bridge including its (skew or straight) abutments using a three-dimensional continuum finite element model under multiple ground motions is not a practically feasible approach in quantify the broad range of seismic responses of bridges (see, for example, Mackie and Stojadinovic 2007; Aviram *et al.*, 2008; Kaviani *et al.*, 2014). As such, the development of a simpler—yet computationally efficient—macroelement model that accurately mimics the seismic response of skew abutments will be pursued in the present effort.

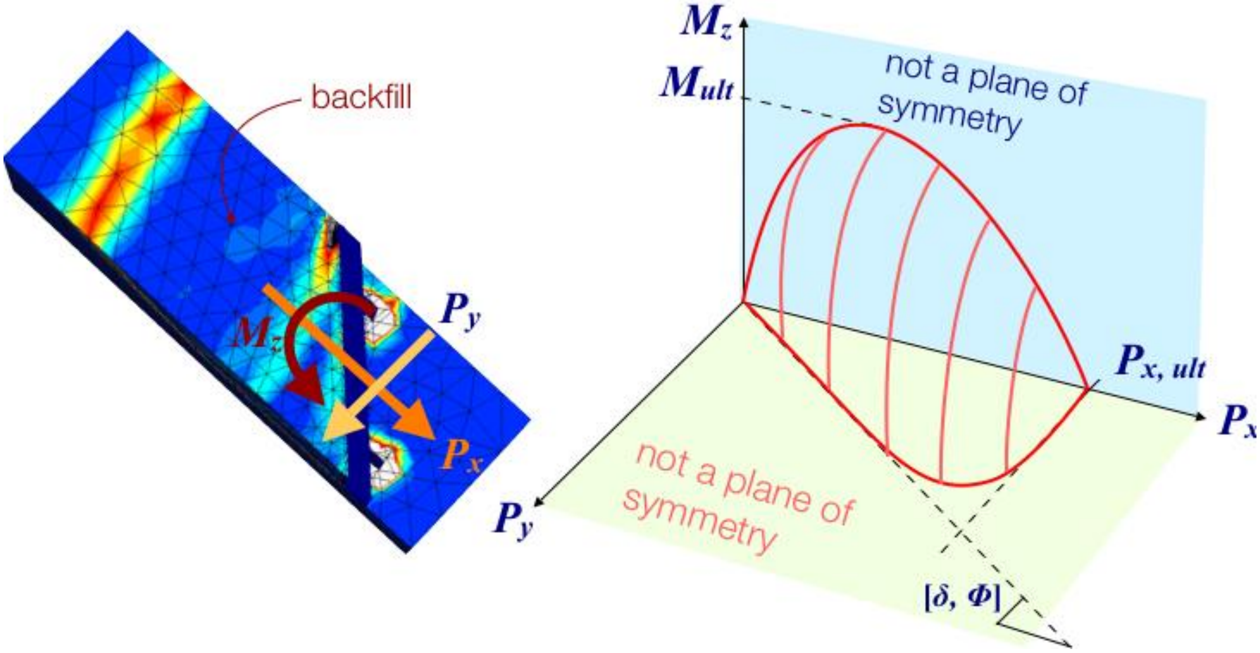

Figure 1.3 The reacting resultants (left) and the anticipated capacity surface (right) are illustrated for the *conceptual* resultant-based plasticity model that represents the inelastic response of a skew abutment.

Macroelement models are lumped, phenomenological representations of the complex behavior observed in soil-foundation-structure-interaction (see, for example, Boulanger *et al.*, 1999, Taciroglu *et al.*, 2006, Rha and Taciroglu 2007, for macroelements devised for pile-soil interaction). They offer a modular and intuitive structure that is composed of sub-elements, and each of these sub-elements represents a particular aspect of the overall behavior—which, in the case of skew abutments, are gapping, elastoplastic soil responses, wall-soil friction and slip, etc. The macroelement that will be developed in this research will be a resultant-based model (Fig. 1.3) that is grounded within the framework of classical rate-independent plasticity theory (Simo and Hughes, 1998). It will provide a skew-angled abutment's reaction forces and moments under longitudinal, transverse, and rotational motions of the bridge deck. The initial yield and ultimate surfaces of the resultant plasticity model will be probed using three-dimensional finite element models for a given soil condition, skew angle, and wall height. Parametric studies will be conducted in which the backfill's strength parameters, along with skew angle will be incrementally varied, and the influence of these variations on the ultimate and initial yield surfaces will be parameterized, yielding general versions of the model.

1.3 Outline of this dissertation

In **Chapter 2**, research objectives are further delineated, and a review of pertinent literature is provided. **Chapter 3** is devoted to a review of experimental studies on straight abutments—conducted at previously UCLA, UC-Davis, and elsewhere—and to validation studies carried out with data from these tests on FE models that will be subsequently used for macroelement model development. **Chapter 4** is dedicated to the development of a particularly important building block that is needed in the development of the general macroelement model. The said sub-model provides a bounded approximation of the lateral force-displacement backbone curve for a skew—yet non-rotating—abutment, given the physical parameters of the backfill (i.e., soil internal friction angle, density, etc.) and the geometric parameters of the abutment (i.e., backwall height and skew angle). In **Chapter 5**, this model is used in devising the general macroelement model that allows transverse translations as well as rotations of the abutment. This general model is then verified against 3D FEM simulations. A summary and an outlook for future studies are presented in **Chapter 5**.

Chapter 2

Literature Review

2. Literature Review

2.1 Incidence of skew

A bridge abutment system exhibits a complex nonlinear dynamic response under strong earthquake loading. The lateral force-deformation relationship between an abutment backwall and its backfill can dominate the seismic bridge performance, particularly of bridges with a modest number of spans (see, Kaviani *et al.*, 2012). The abutment-deck interaction becomes even more complex for "skew bridges." Because the incidence of bridges with skew angled abutments is quite high, it is imperative to devise accurate models to predict the effect of the skew angle of a bridge on its overall seismic response. Figure 2.1 displays a histogram of skew angles for bridges in California (NBI, 2002). This data indicates that, of the 23,000+ Caltrans bridges in the NBI database, more than 13,000 (i.e., more than half) have skewed abutments. Most short- and mid-span bridges in California have some skew angle, which can be as severe as 60 degrees, and ~90% of these bridges have seat-type abutments.

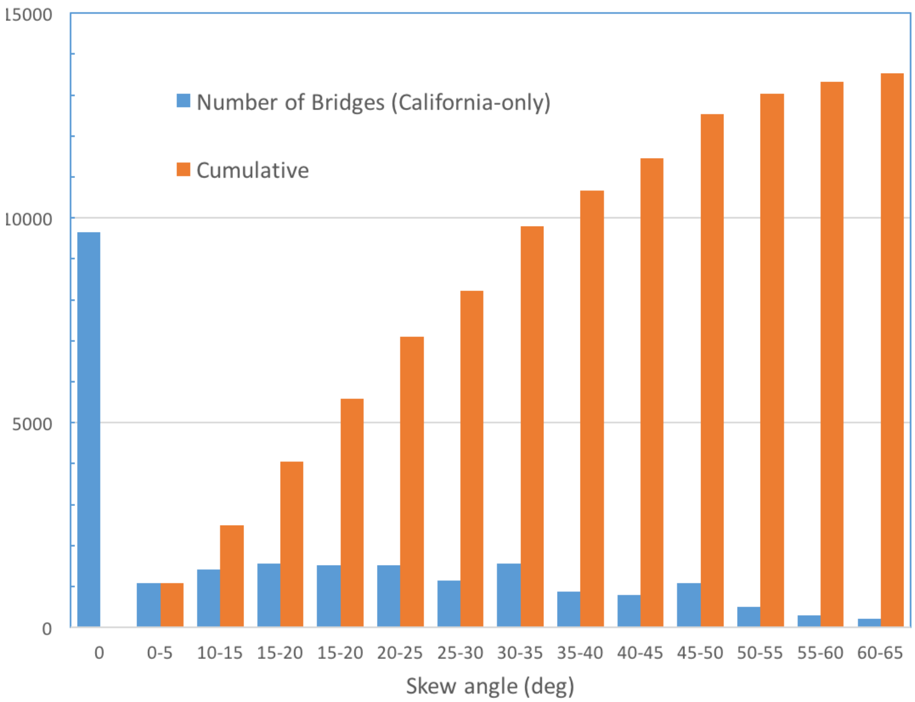

Figure 2.1 Distribution of skew bridges in California (source, NBI database, 2012; courtesy of B. Cetiner).

2.2 Field observations and previous studies on skew bridges

Observations from past earthquakes (Jennings *et al.*, 1971; Yashinsky *et al.*, 2010; Kawashima *et al.*, 2011) suggest that there are significant differences between the responses of straight and skewed bridges. A manifestation of this difference is the inherent tendency of the decks of skewed bridges to rotate about their vertical axes under seismic excitation, which can lead to decks unseating from their abutments, and ultimately, to collapse (Figure 2.2).

Figure 2.2 One of the many skew bridges that collapsed during the 2010 Maule, Chile, Earthquake seen on the right. The nearby bridge (partially seen on the left) that had straight abutments survived (Kawashima *et al.*, 2011).

Excessive deck rotations can also cause loss of bridge functionality and/or stability and significant downtime for repairs. Site investigation of the Foothill Boulevard Undercrossing located in California (34.25N and 118.5W), which has a skew angle of approximately 60°, showed that the deck had rotated in its horizontal plane, resulting in a permanent offset of approximately 7.5 cm (i.e., 0.9×10^{-3} rad. of deck rotation) in the direction of increasing skew angle during the 1971 San Fernando Earthquake (Jennings *et* *al.*, 1971). Reconnaissance reports of the 2010 Chile Earthquake (Yashinsky *et al.*, 2010; Kawashima *et al.*, 2011) state that skewed bridges in affected regions rotated, mainly about their center of stiffness, and that those with weak exterior shear keys suffered higher levels of damage due to transverse unseating. The primary causes of this excessive rotation are usually noted as one or more of the following:

- Eccentric passive resistance of the abutment backfill
- Pounding between the decks
- Pounding between the decks and an integral abutment (i.e., a relatively rigid wall).

The analytical/numerical studies on skew bridges to date have primarily focused on pounding/contact effects, and represented the abutment backfill response with linear springs and dashpots, or as a rigid boundary (see, for example, Maragakis and Jennings, 1987; Abdel-Mohti and Pekcan, 2010; Dimitrakopoulos, 2011). As such, these studies omit the primary function of the backfill, which is to dissipate energy through inelastic response so that the potential for damage in bridge superstructure and foundation elements are reduced—i.e., collapse is prevented and repairs are confined to the abutment (Caltrans SDC, 2010). Only a few attempts have been made for developing requisitely detailed (albeit non-validated) models in which soil inelasticity is accounted for (Shamsabadi *et al.*, 2006a,b; Kaviani *et al.*, 2012; 2014; Omrani *et al.*, 2015). Some of these earlier attempts are briefly described below.

The dynamic behavior of the skew bridges (magnitude-6.7) has received considerable attention following the 1971 San Fernando earthquake. Chen and Penzien (1977) studied the effect of seismic soil foundation-structure interaction on the global behavior of skew bridges using a finite element model. Their model included a linear elastic beam to represent the bridge deck and the bridge columns, and linear springs were used to represent the foundation flexibility. A three-dimensional linear continuum finite element was used to represent the backfill and the abutment wall. The elastic perfectly plastic Mohr-Coulomb yield criterion was used to represent the nonlinear abutment-backfill interface interaction. They concluded that the foundation flexibility and in particular the poundings between the bridge deck and the abutments have significant influence on the global response of the bridge structures and should be included in the bridge model.

Traditional bridge design practice evaluates dynamic performance of skewed bridges using spline models (Caltrans, 2010). The spline model is a collection of beam finite elements with cross-section properties adjusted from geometric data to match the flexural and inertial properties of the deck. Researchers have used both the simple spline models and the detail continuum finite element models. Maragakis and Jennings (1987) used a rigid beam element to model the bridge deck. Ghobarah and Tso (1974) used a spine-line model to represent the bridge deck, and columns, and concluded that the bridge collapse was caused by coupled flexural-torsional motions of the bridge deck, or by the excessive compression demands that resulted in column failures. Using simplified beam models, Maragakis and Jennings (1987) concluded that the angle of the skew and the impact between the deck and abutment govern the response of skewed bridges. Wakefield *et al. (*1991) conjectured that if the deck is not rigidly connected to the abutments, then the dynamic response of the bridge is dominated by planar rigid-body rotations of the deck rather than coupled flexural-torsional deformations.

In more recent studies, Meng and Lui (2000, 2002) proposed that the seismic response of a bridge is strongly influenced by the column boundary conditions and skew angle. By using a dual-beam stick model to represent the bridge deck, they showed that in-plane deck rotations are mostly due to abutment reactions. Using nonlinear static and dynamic analyses, Abdel-Mohti and Pekcan (2008) investigated the seismic performance of a three-span continuous RC box-girder bridge for abutment skew angles ranging between 0 and 60 degrees. They used detailed finite element as well as simplified beam-stick models, and concluded that simplified beam-stick models can capture the coupled lateral-torsional response of skewed bridges for moderate skew angles.

An approximate method for dynamic analyses of skewed bridges with continuous rigid decks was proposed by Kalantari and Amjadian (2010). They developed a three degree-of-freedom analytical model to determine the natural frequencies, mode shapes, and internal forces for short skewed bridges. Dimitrakopoulos (2011) investigated the seismic response of short skewed bridges with pounding deck-abutment joints, and proposed a "non-smooth" rigid-body approach to analyze their response. Dimitrakopoulos concluded that the tendency of skewed bridges to rotate after deck-abutment collisions is a factor of the skew angle, deck geometry, and the friction between the deck and abutment.

Shamsabadi *et al.* (2006a, b) modeled the skew abutment with inelastic springs. The backbone curves of these springs were heuristically adjusted through observations made in three-dimensional finite element simulations of the backfill response. Later, Kaviani *et al. (*2012, 2014) as well as Omrani *et al.* (2015) further developed and refined similar models, and applied a performance-based methodology to predict the response of various representative skew bridges. These studies quantifiably showed that the deck rotation and column drift ratio values, *and* the probability of collapse are higher for skew bridges than those for straight bridges; but a larger skew angle is not always worse.

Although these aforementioned studies resulted in a better understanding of the seismic behavior of skewed bridges, a broader and more accurately quantified understanding of their responses and collapse mechanisms is necessary. In particular, a validated model of the passive backfill response of skew-angled abutments is needed *to assess the very large inventory of skew bridges in the US and around the world* This model should not only be accurate, but also highly computationally efficient so that the requisite comprehensive parametric studies on skew bridges subject to broad suites of ground motions can be carried out.

2.3 Caltrans seismic design criteria for skew bridges

Section 7.8 of the 2010 Caltrans Seismic Design Criteria document describes the design standard for longitudinal abutment responses. The representation of lateral backwall-backfill behavior in the design standard consists of an elastic-perfectly-plastic spring, which provides a backbone curve (Fig. 2.3, left) suitable for static or pushover-type analyses. The properties of the abutment spring are K_{eff} and P_{bw}, which represent the effective abutment stiffness and capacity, respectively. In the current version of Caltrans SDC (2010) Both stiffness model parameters are derived from the experimental results of Romstad *et al.* *(*1995) and Stewart *et al.* *(*2007) for cohesive and granular backfill materials, respectively. Both of these abutment tests[1] were performed using 1.68 m (5.5 ft) tall walls.

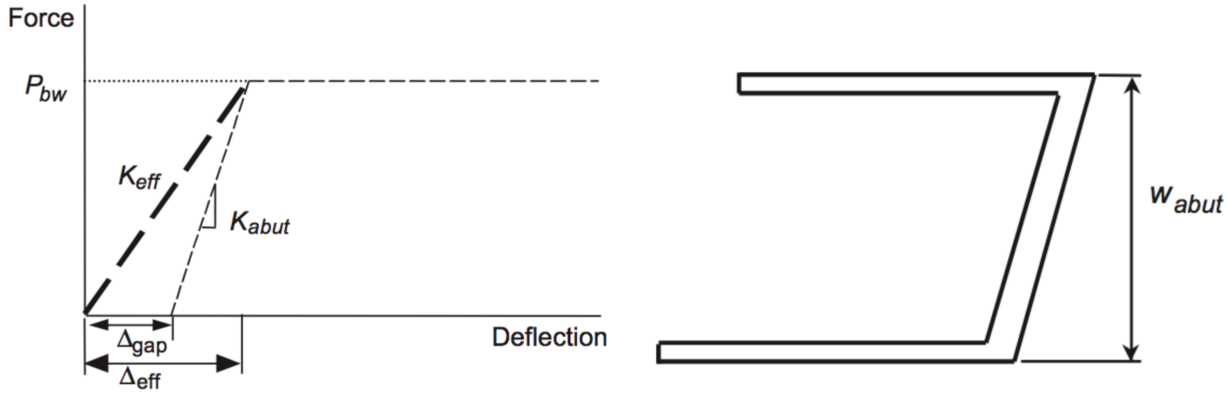

Figure 2.3 Backbone of lateral response for abutments (left), and effective abutment width for skew abutments (right) (Caltrans SDC 2010).

The effective stiffness is given as 290 kN/cm per meter of wall-width (i.e., 50 kip/in per foot of wall-width)—for fill material conforming to the requirements of Caltrans Standard Specifications; for material not in conformance with the Standard Specification, the stiffness value is halved (applied for clayey materials). For wall heights different from 1.68 m, the stiffness is proportioned to the actual backwall height as follows:

$$K_{abut} = \begin{cases} K_{eff,\,1.68} \times w \times \left(\dfrac{h}{1.68}\right) & \text{(m, kN)} \\ K_{eff,\,5.5} \times w \times \left(\dfrac{h}{5.5}\right) & \text{(ft, kips)} \end{cases} \tag{2.1}$$

---

[1] These two full-scale tests will be extensively discussed in Chapter 3, as they are utilized to validate the finite element models used in the present study.

where K_{eff} is the initial stiffness, $K_{eff,1.68}$ is the stiffness for a 1.68m wall height per unit width as given above, h is the backwall height, and w is the projected width of the backwall—for skew bridges $w = w_{abut}$ as shown in Fig. 2.3 (right). Note that the linear/proportional height adjustment factor implies a depth-invariant lateral stress distribution behind the backwall.

The capacity of the backwall spring is represented in stress units as 239 kPa (5.0 ksf) for the standard 1.68m (5.5 ft) backfill height. The capacity scaling law with the wall height is, again, linear:

$$P_{bw} = \begin{cases} A_e \times 239 \text{ kPa} \times \left(\dfrac{h_{bw}}{1.68} \right) & \text{(m, kN)} \\ A_e \times 5.0 \text{ ksf} \times \left(\dfrac{h_{bw}}{5.5} \right) & \text{(ft, kips)} \end{cases} \tag{2.2}$$

As indicated by the preceding discussion, present Caltrans SDC provisions are highly simplistic; and because they do not anticipate potential rotation of the bridge deck due to eccentric backfill reaction, it is not clear whether they are even conservative or not.

2.4 Macroelements models for soil-structure interaction

Macroelements are obtained by reducing or condensing the behavior of a subdomain or substructure. In soil-foundation-structure interaction (SFSI) problems, this subdomain is usually that of the soil. Macroelements for SFSI analysis usually strive to model the response adjacent to the structure (i.e., the near field)—which includes soil's inelastic reactions, and frictional contact and gapping between the soil and the foundation elements (see, for example, Taciroglu *et al.*, 2006). The remote soil domain (i.e., the far field) supplies the excitation and extracts energy from the overall system through radiation. These responses are usually substantially different for dynamic loading than those predicted for pushover or cyclic loading conditions utilized in simplified design procedures.

The macroelement concept has been utilized numerous times in past research on SFSI. In particular, *material nonlinearities* were investigated with the help of detailed finite element simulations (Borja *et al.*, 1994), as well as experimentally (Funston and Hall, 1967; Stokoe and Richard, 1974; Gazetas and Stokoe, 1991). In these studies, spring-dashpot assemblies or modification functions to the foundation impedance matrix were developed to model the mechanical interaction between a rigid-body and flexible ground. Nonetheless, these models were primarily phenomenological and were based on curve-fitting to numerical or experimental results for *ad hoc* scenarios. Therefore, they were highly dependent on the calibration conditions (Finn and Yogendrakumar, 1989). Attempts were also made to account for *geometric nonlinearities* associated with gap formation between the foundation and the soil (Wolf 1976; Wolf and Skriherud, 19778; Kobori *et al.*, 1982).

More recently, macroelements have been developed for shallow foundations on cohesionless (Nova and Montrasio, 1991; Paolucci, 1997) and cohesive soils (Crémer, 2001), and for pile foundations (Boulanger *et al.*, 1999; Taciroglu *et al.*, 2006; Rha and Taciroglu, 2007).

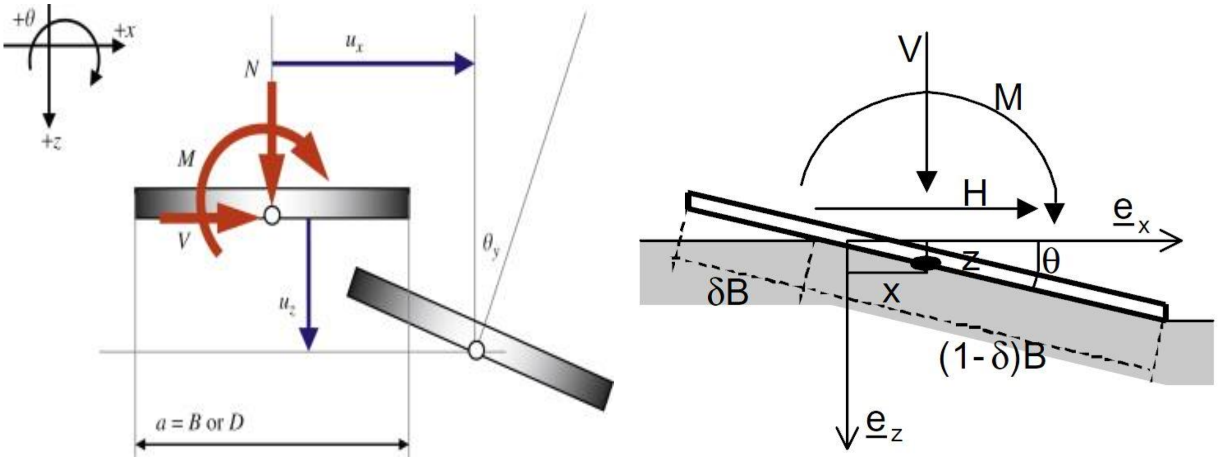

Figure 2.4 Rigid strip footing, occurrence of plate-soil separation (Nova and Montrasio, 1991).

The macroelement model that will be developed in this research similar to the original work of Nova and Montrasio (1991), who applied the concept of resultant-based plasticity to develop a reduced-order representation of soil reaction under a shallow footing. Based on number of experiments performed on a rigid strip foundation resting on a frictional soil and subjected to a vertical (*V*) and lateral forces (*H*) and moment (*M*), Nova and Montrasio formulated a global elastoplastic model with isotropic hardening for the entire soil–foundation system (Fig. 2.4). The model was written in terms of resultant vertical and horizontal forces and moment acting on the footing normalized by the maximum supported vertical force; and was used for the prediction of the footing displacements for quasi-static monotonic loading. The result was a rugby-ball-shaped ultimate surface, which is shown in Figure 2.5.

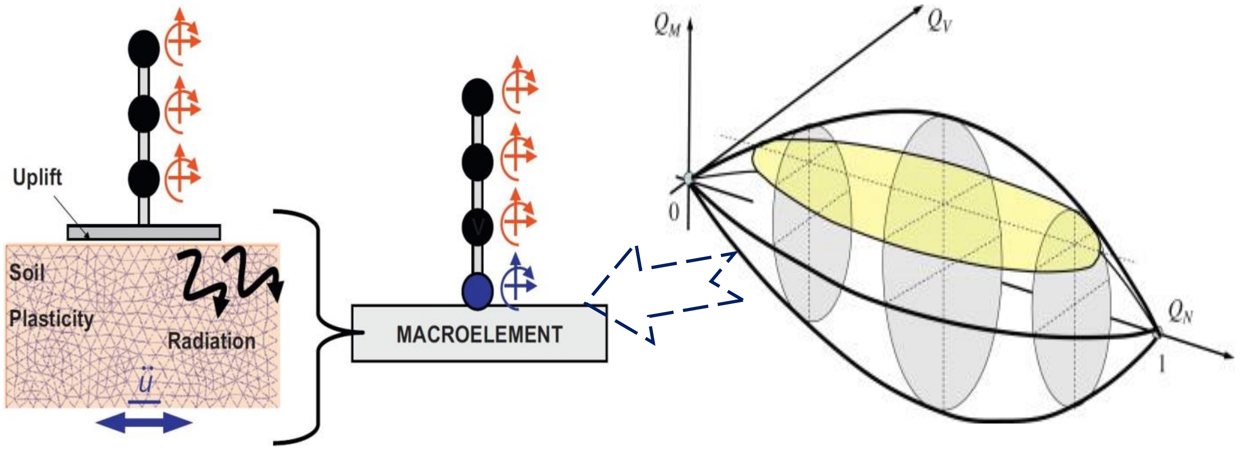

Figure 2.5 Generic soil–foundation–structure system subjected to dynamic loading and macroelement concept (left). Rugby-ball-shaped *surface of ultimate loads* (Nova and Montrasio 1999) describing the behavior of the macroelement (right) [figure adapted from Chatzigogos *et al.*, 2008].

This model was later incorporated into a macroelement model by Pecker and Davenne (2002), and a similar model with capabilities to explicitly account for gapping was recently proposed by Gajan and Kutter (2009). Other related efforts on macroelement models—which primarily focused on dynamic behavior—are briefly summarized in Table 2.1.

Table 2.1 Overview of existing macro-models for shallow foundations [reproduced from Chatzigogos *et al.*, 2008].

Authors	Year	Configuration	Description
Nova and Montrasio	1991	Strip footing resting on a purely frictional soil	Isotropic hardening plasticity model and non-associated flow rule. Application in the case of quasi-static monotonic loading
Paolucci	1997	Strip footing resting on a purely frictional soil	Perfect plasticity model with non-associated flow rule. Application to simple structures subject to seismic loading. Parametric studies
Pedretti	1998	Strip footing resting on a purely frictional soil	Hypo-plastic model for the description of the system response under cyclic loading. Consideration of uplift by reduction of elastic stiffness. Applications to structures subject to quasi-static cyclic loading
Gottardi *et al.*	1999	Strip footing resting on a purely frictional soil	Isotropic hardening plasticity model. Detailed description of the system ultimate surface (identified as the yield surface of the plasticity model) via ‘‘swipe tests’’. Application in the case of quasi-static monotonic loading
Le Pape and Sieffert	2001	Strip footing resting on a purely frictional soil	Elastoplastic model derived from thermodynamics principles. Rugby-ball-shaped yield surface and ellipsoidal plastic potential. Application to seismic loading
Cremer *et al.*	2001, 2002	Strip footing resting on a purely cohesive soil without resistance to tension	Non-associated plasticity model with isotropic and kinematic hardening coupled with a model for uplift. Application to seismic loading
Martin and Houlsby	2001	Circular footing resting on a purely cohesive soil	Non-associated plasticity model with isotropic hardening. Detailed description of the yield surface via ‘‘swipe tests’’. Application to quasi-static monotonic loading
Houlsby and Calssidy	2002	Circular footing resting on a purely frictional soil	Non-associated plasticity model with isotropic hardening. Detailed description of the yield surface via ‘‘swipe tests’’. Application to quasi-static monotonic loading
Di Prisco *et al.*	2003	Strip footing resting on a purely frictional soil	Hypo-plastic model for the description of the behavior under cyclic loading. Application to quasi-static cyclic loading
Cassidy *et al.*	2004	Circular footing resting on a frictional or cohesive soil	Fully three-dimensional formulation. Application to the offshore industry. Quasi-static monotonic loading
Houlsby *et al.*	2005	Strip or circular footing resting on cohesive soil. Frictional soil–footing interface	Decoupled Winkler springs with elastic perfectly plastic contact-breaking law derived from thermodynamics principles. Application to quasi-static cyclic loading
Einav and Cassidy	2005	Strip footing resting on cohesive soil. Frictional soil–footing interface	Decoupled Winkler springs with elastoplastic contact-breaking law with hardening derived from thermodynamics principles. Application to quasi-static cyclic loading
Grange *et al.*	2006	Circular footing on cohesive soil	Extension of the plasticity model of Cremer to purely three-dimensional setting. No separate uplift model included
Chatzigogos *et al.*	2009	Circular and squared footing resting on a frictional soil	New formulation for shallow. non-linear constitutive law written in terms of some generalized force and displacement parameters

2.5 Test data on skew abutments

As described in the introduction section, there have been a number of laboratory/field tests on straight abutments. These data sets will be reviewed later in Chapter 3, and will indeed be used in validating continuum finite element, semi-analytical models, as well as the special case of zero-skew of the macroelement model (in Chapter 5) that will be developed in the present study.

On the other hand, test data on skew abutments are extremely scarce. In fact, to the best of the author's knowledge, the only such data set is based on a series of laboratory tests on 1.67m × 6.5m backwall specimens with different skew angles that were carried out by Rollins and Jessee, (2013). In these tests, the skew wall was pushed into the backfill while transverse movements and rotations were suppressed. Measurements by Rollins and Jessee (2013) indicated a drop in the capacity of the lateral backfill reaction with increasing skew angle (see, Fig. 2.6). Later in this document (Chapter 4), it will be argued that such drops in lateral capacity are *not theoretically possible*, and the parameters and mechanisms that could have possibly led to the said observations will be discussed in detail in a quantitative manner later in §4.6.

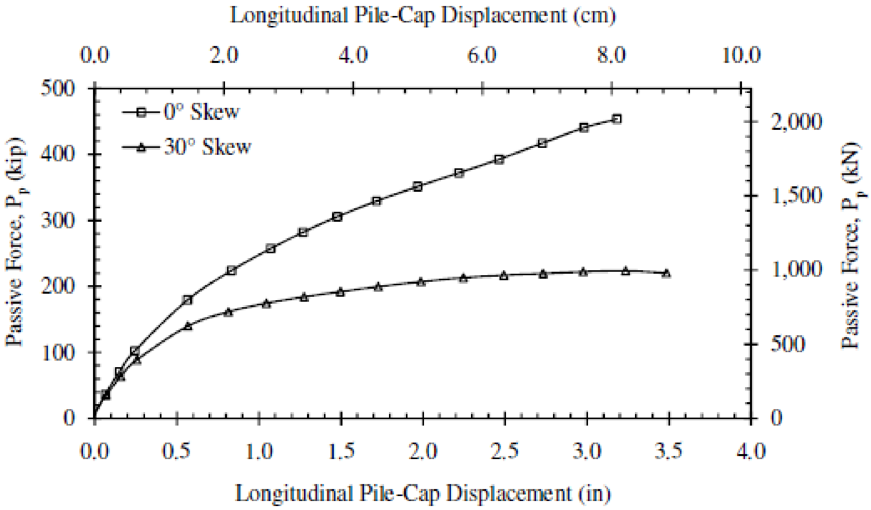

Figure 2.6 Force-Deflection curves results from a 1.67 m (5.5 ft.) high and 6.50 m (11.5 ft.) wide wall with 0-degree and 30-degree skew angles (Rollins and Jessee, 2013).

Chapter 3

Prior Studies on Straight Bridge Abutments and Validation of Finite Element Models

3. Prior Studies on Straight Bridge Abutments and Validation of Finite Element Models

3.1 Full-scale tests on straight abutments

Passive response of a backfill is a classical theme in geotechnical engineering research (Kramer, 1996), and first studies date back to Coulomb (1776) and Rankine (1857). Predictions from those earlier theoretical models and their subsequently enhanced versions (Terzaghi, 1934) have been tested numerous times—usually through laboratory-scale tests, or experiments performed on centrifuge models. A fairly detailed review of this literature may be found in the report by Stewart *et al. (*2007), and will be omitted here for brevity. The typical aim in these tests is to develop relationships for lateral pressure and displacement and to develop models that can predict these quantities based on fundamental properties of the system (i.e., soil strength parameters, wall and backfill geometry, etc.).

In this chapter, we review two recent test conducted on full-scale specimens, with the specific aim of quantifying passive backfill response for seat-type abutments. Conducted at UC-Davis (Romstad *et al.*, 1995) and at UCLA (Stewart *et al.*, 2007), these two tests were commissioned by Caltrans to quantify passive response of cohesive (UCD test) and granular (UCLA test) backfills that are commonly used in California's highway bridges. At the present time, provisions on abutments in the latest Caltrans Seismic Design Criteria document (Caltrans SDC, ver. 1.6) are based on the results of these two tests. There were also significant modeling efforts devoted to the generalization of the results from the UCLA and UCD tests (see, for example, Shamsabadi *et al.*, 2010; Khalili-Tehrani *et al.*, 2009, 2010, 2011). The validated models obtained in those previous studies by will form the basis of proposed studies on skew abutments. A review of these validation efforts is also provided in this Chapter.

3.1.1 Full-scale testing of an abutment with granular backfill

University of California, Los Angeles (UCLA) researchers (Stewart *et al.*, 2007) tested a 4.6 m wide, 1.67 m tall seat-type abutment wall with a silty sand backfill under one-way cyclic loading. The backfill was compacted to over 95% Modified Proctor relative compaction. The backwall was pushed horizontally between two wingwalls without any vertical movement. The one-way cyclic loading involved pushing the wall into the backfill by prescribed amounts, followed by unloading to nearly at-rest conditions, followed in turn by further pushing. Gapping at the wall-backfill interface was not allowed. Wingwalls were constructed using smooth plywood with plastic sheeting on the interior face to minimize friction, and thus, to impose a plane-strain condition. This test is hereafter referred to as the UCLA abutment wall test. The lateral capacity of the abutment backfill per unit wall-width was measured to be approximately 477 kN/m at a lateral displacement of 5 cm (3% of abutment height). The ultimate residual capacity was approximately 442 kN/m, which was reached at a lateral displacement of 8.5 cm. This corresponded to an ultimate residual capacity of 265 kN per 1 m^2 of wall area (i.e., 265 kPa). The initial (tangent) stiffness of the backbone curve was 345 kN/cm/m.

3.1.2 Full-scale testing of an abutment with cohesive backfill

University of California, Davis (UCD) researchers, Romstad *et al. (*1995) cyclically loaded a monolithic abutment to failure. This abutment wall was 3.05 m wide and 1.67 m tall. The sheared part of the backfill material in this test was Yolo loam, which was compacted to a minimum relative compaction of 90%. Based on strength testing on this material and other recommendations provided by of Romstad *et al. (*1995), subsequent analyses were carried out with $\phi=0$, and $c=100$. The ultimate passive pressure of the abutment was measured to be approximately 265 kPa (5.5 ksf), which was reached at a lateral displacement of 16.8 cm (10% of the abutment height). The secant stiffness at 50% of load capacity per unit width of the backwall was calculated to be approximately 145 kN/cm/m (25 kips/in/ft) (Shamsabadi *et al.*, 2007). This test is hereafter referred to as the UCD abutment wall test.

3.2 Numerical simulations of full-scale abutment tests

In what follows, the LSH and FE simulation models and their validation against the UCLA and UCD tests are described. For brevity, modeling details are provided for only the UCLA test—for the UCD test only input data and sample results are presented.

3.2.1 Simulation of the UCLA test with Log-Spiral Hyperbolic (LSH) model

The Log-Spiral Hyperbolic (LSH) model is a plane-strain model that was developed to estimate nonlinear force-displacement relationships for abutment walls based on the wall dimensions and backfill soil properties (Shamsabadi *et al.*, 2007). The model is based on a limit-equilibrium method for ultimate capacity that employs logarithmic spiral failure surfaces, coupled with a modified hyperbolic soil stress-strain relationship to evaluate load-deflection behavior. Unlike classical limit-equilibrium methods, shear resistance of the soil is not assumed to be simultaneously mobilized across the full failure surface in this approach, but varies as a function of the backfill's progressive failure and strain localization. Each progressive failure surface is associated with the mobilized shear resistance and strain of the backfill.

In an earlier study, Shamsabadi *et al.* (2007) verified the LSH model against nonlinear force-displacement measurements from several full-scale, centrifuge and small-scale laboratory tests on abutments and pile caps with a variety of backfills. Shamsabadi *et al.* (2010) compared LSH predictions to the results of the UCLA test and found that model predictions made using upper- and lower-bound strength parameters bracket the data.

Table 3.1 Parameters Used for the Simulation of UCLA Test with the LSH Model (Shamsabadi, 2009).

	Strength Parameters				Displacement Parameters		
	Unit weight, γ(kN/m^3)	Friction angle, ϕ	Cohesion, c (kPa)	Wall friction angle,δ	Failure ratio, R_f	Strain, ϵ_{50}	Poisson's ratio, ν
Lower **B**ound	20.0	40^o	14	20^o	0.97	0.0035	0.3
Upper **B**ound	20.0	39^o	24	20^o	0.97	0.0035	0.3

The total stress strength parameters (e.g., *c* and ϕ) used in the LSH simulation model for the UCLA tests are shown in Table 3.1, which were obtained through triaxial compression tests on several bulk samples from the abutment backfill (Stewart et al., 2007; Shamsabadi et al., 2010). Magnitudes of the remaining model parameters—i.e., failure ratio (R_f), strain at 50% of ultimate capacity ($\varepsilon_{□□}$), and Poisson's ratio (ν)—were set to values recommended by Shamsabadi *et al. (*2007). The wall-soil interface friction value (δ) given in Table 3.1 is generally consistent with test measurements by Stewart *et al. (*2007), who observed that this quantity varied with lateral displacement, and ranged between 13 and 20 degrees. The largest value that was observed at lateral displacements greater than 7.6 cm were chosen.

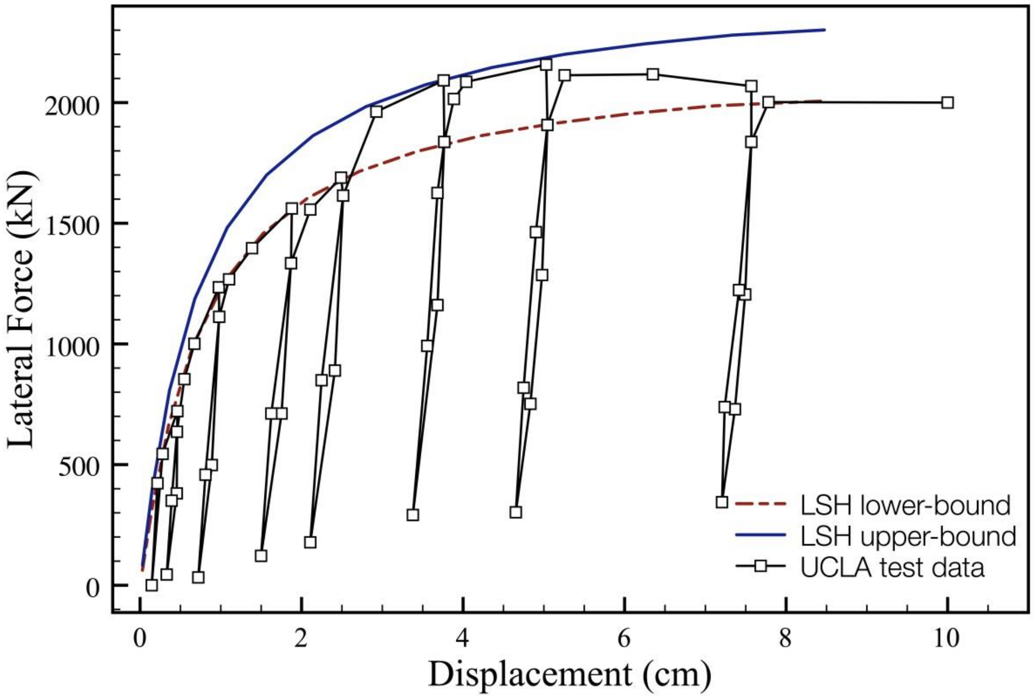

Figure 3.1 Measured and LSH-computed backbone curves of the UCLA abutment test (Shamsabadi *et al.*, 2010).

Figure 3.1 displays the simulated force-displacement backbone curves using the LSH model and the one-way cyclic curve recorded during the UCLA test (Stewart et al., 2007; Shamsabadi et al., 2010). As noted previously, responses predicted with the LSH model using the higher (UB) and lower (LB) soil strength parameters bracket the observed response very well.

3.2.2 Simulation of the UCLA test with finite element models

Software package PLAXIS (Vermeer & Brinkgreve, 1998) was used for the finite element simulations of the UCLA and UCD abutment tests. PLAXIS is capable of performing two- and three-dimensional analyses, and provides a sophisticated library of soil constitutive models.

Constitutive Model for the Backfill: A recent study that involved triaxial testing of abutment-backfill materials from many bridge sites in California revealed that the stress-strain backbone relationships are typically hyperbolic in shape (Kapuskar, 2005). These observations led to the selection of the "Hardening Soil (HS)" model available in PLAXIS for both two- and three-dimensional finite element simulations. This model is formulated within the framework of classical theory of plasticity; it features a yield cap and soil dilatancy effects (Schanz *et al.*, 1999). Figure 3.2 (left) displays the hyperbolic relationship that the HS model yields between the deviatoric stress (q) and axial strain (ε) in primary loading during a drained triaxial test. Here, q_f is the stress at failure, q_u is the asymptote of the hyperbolic curve (not shown on figure), and R_f denotes their ratio (i.e., $q_f = R_f\ q_u$).

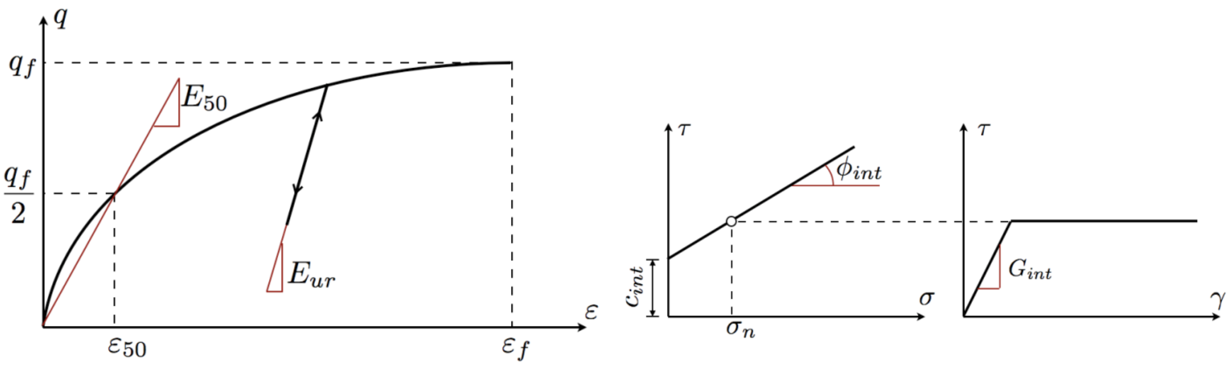

Figure 3.2 Stress-strain curve of the PLAXIS "Hardening Soil" model (left), and backwall-backfill interface relationship adopted in FE simulations (right) (Shamsabadi *et al.*, 2010).

Interface Elements: Zero-thickness finite elements available in PLAXIS were used to represent the frictional contact between the backwall and the backfill. Each interface element is defined by five node-pairs. A simple bilinear stress-strain relationship describes the response of the backfill-backwall interaction element, and a classical Coulomb criterion discerns elastic behavior—where small displacements can occur within the interface—and plastic slip. To wit, the interface remains elastic if the shear stress τ satisfies the inequality

$$\left|\tau\right| < \sigma_n \tan\phi_{\text{int}} + c_{\text{int}} \tag{3.1}$$

and the interface displays perfectly plastic behavior when

$$\left|\tau\right| = \sigma_n \tan\phi_{\text{int}} + c_{\text{int}} \tag{3.2}$$

where ϕ_{int} and c_{int} are the interfacial friction angle and cohesion, and σ_n and τ denote the normal (pressure) and shear stresses acting at the interface, respectively. The strength properties of interface elements are linked to those of the abutment backfill through a strength reduction factor ($R_{int} \leq 1$). Specifically, the interface properties are calculated through the relationships given as

$$c_{\text{int}} = R_{\text{int}}\, c, \quad \tan\phi_{\text{int}} = R_{\text{int}} \tan\phi \tag{3.3}$$

Figure 3.2 displays the strength-stress (τ□σ) and stress-strain (τ□γ) relationships of the interface elements. Once the specified shear strength is reached, shear stress remains constant as long as the interface slip rate remains positive. The PLAXIS default value for the interfacial shear stiffness is $G_{\text{int}} = R_{\text{int}}^2\, G$, where G denotes the backfill shear stiffness. This default setting was used in the simulations.

Finite element simulations of the test specimen were performed using both two- ***and*** three-dimensional models. The two-dimensional (plane-strain) finite element model comprised 15-node triangular continuum elements, and 5-node backwall-backfill interface elements as shown in Figure 3.3(a, b). The right and left vertical boundaries were placed at distances of 4.5H and 1H away from the backwall, respectively, where H denotes the backwall height. The bottom domain boundary was located at a depth of $2H$ below backfill ground-line. These distances were chosen through trial-and-error whereby the extent of the domain was increased until the changes observed in computed lateral load-displacement response became negligible. The bottom boundary was fixed in both directions in the model and the left and right sides of the soil domain were free to move vertically but were fixed in the horizontal direction.

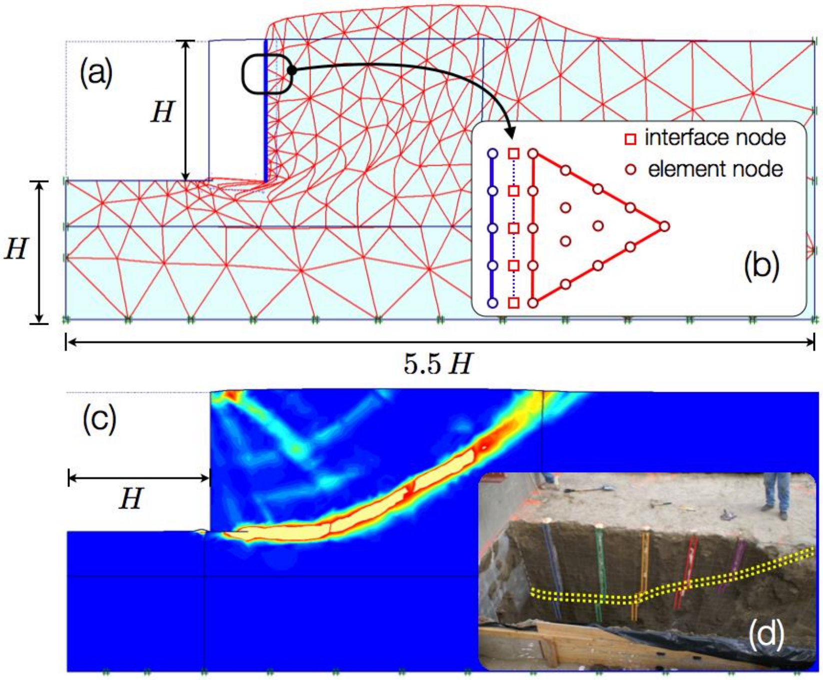

Figure 3.3 Plane-strain FE simulation of the UCLA test (a) original wall location and the deformed mesh; (b) interface elements used; (c) deviatoric shear strain distribution in soil; (d) observed failure surface (Shamsabadi *et al.*, 2010).

The aforementioned triaxial compression tests were used to estimate the previously defined loading stiffness (E_{50}), unloading stiffness (E_{ur}), and strength properties of the backfill soil. Specific values of the interface and HS model parameters used in the simulations of the UCLA test are given in Table 3.2. Following the PLAXIS manual, dilatancy angle was chosen to be $\psi = \phi$□□ (Vermeer and Brinkgreve, 1998). The value of the interface strength reduction parameter was chosen as $R_{int} = 0.50$, which is consistent with the experimental observation that indicated the interface friction angle (δ) to be half of the backfill friction angle (ϕ).

Table 3.2 Parameters Used in FE Simulations of the UCLA Abutment Test (Shamsabadi *et al.*, 2010).

Strength Parameters				Displacement Parameters				
Unit weight, Υ(kN/m^3)	Friction angle ϕ	Cohesion, c (kPa)	Dilatancy angle, ψ	R_{int}	R_f	E_{50}^{ref} (MPa)	E_{ur}^{ref} (MPa)	v
20.0	40^o	14	10^o	0.50	0.97	70	140	0.3
20.0	39^o	24	9^o	0.50	0.97	70	140	0.3

Each finite element simulation comprised two analysis steps: In the first step, gravity was applied and the wall was "at rest" (K_o condition); in the second step, the wall was pushed into the backfill with prescribed displacements until passive failure occurred. Figure 3.3(a) displays the deformed two-dimensional finite element mesh at the final stage of backfill failure. It reveals the formation of a passive wedge within the abutment backfill. The shear strain distribution throughout the backfill is shown in Figure 3.3(c); and the shape of the ultimate band of localized shear strain is consistent with that of a logarithmic spiral curve and the field observations (cf., Fig. 6d, Stewart *et al*., 2007; Shamsabadi *et al*., 2010).

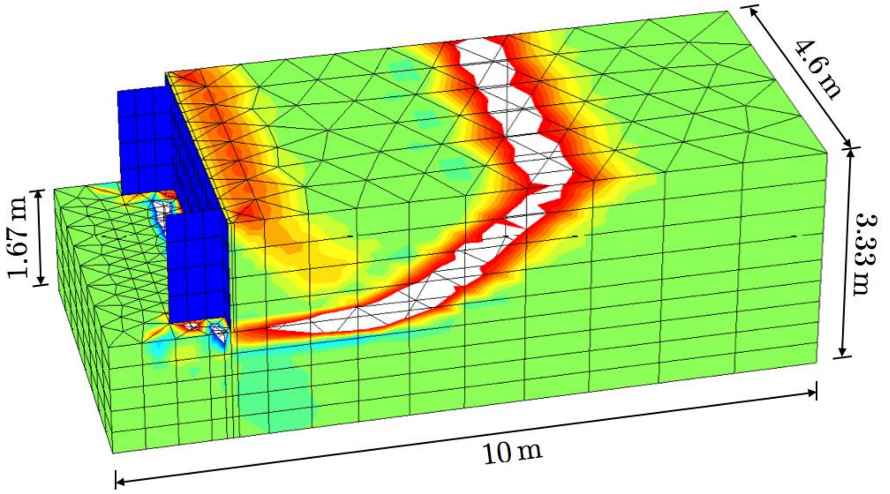

Figure 3.4 Three-dimensional FE simulation of the UCLA test and the deviatoric shear strain distribution (Shamsabadi *et al.*, 2010).

Additional simulations of the UCLA field test were performed using the three-dimensional finite element model shown in Figure 3.4. The extents of the domain at the left, right and bottom of the model matched those from the two-dimensional model, whereas the width was set to 4.6 m to match the UCLA test configuration. The backfill mesh comprised 15-node tetrahedral elements, and the abutment backwall was modeled using plate elements. The backwall was pushed along the longitudinal direction under load-control, and its motion was constrained along the vertical and transverse directions. Again, the ultimate band of localized shear strain is in agreement with the pattern and dimensions observed in the field.

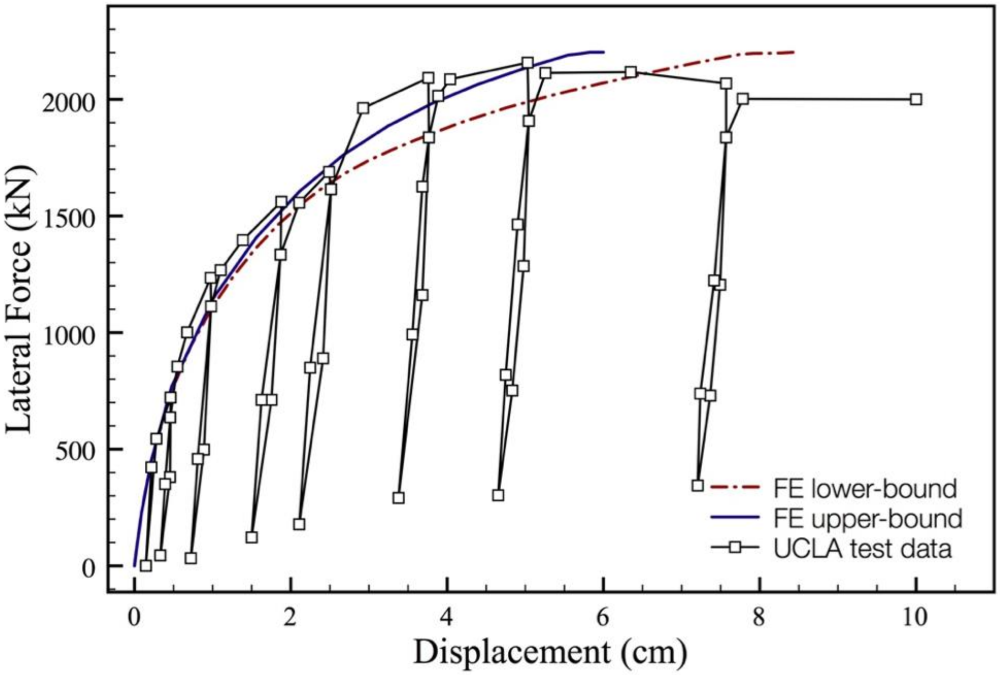

Figure 3.5 Measured and FE-simulated lateral load-deformation curves for the UCLA test (Shamsabadi *et al.*, 2010).

The lateral force-displacement backbone curves obtained in two- and three-dimensional simulations are nearly identical. Therefore, we present the results of only the three-dimensional finite element model of the UCLA test here. As it may be seen in Figure 3.5, the backbone curve obtained from the simulation using upper-bound backfill properties is in better agreement with the experimental curve. Both upper- and lower-bound models appear to slightly over-predict the residual capacity. This was expected, because the HS model employed in these simulations does not feature strain-softening effects.

3.2.3 Simulation of the UCD test with finite element and LSH models

Numerical simulations of the UCD test had been performed in similar fashion with those of the UCLA test. Table 3.3 displays the material data sets used for the LSH (top row) and Finite Element models (bottom row) of the UCD test. These data were selected based on the observation that the failure surface passed through the compacted Yolo loam backfill material with the aforementioned properties.

Table 3.3 Parameters Used in LSH/FE Simulations of the UCD Abutment Test (Shamsabadi *et al.*, 2010).

<table>
<tr><td colspan="6">Strength Parameters</td></tr>
<tr><td colspan="2">Unit weight, Υ (kN/m3)</td><td>Friction angle, ϕ</td><td>Cohesion, c (kPa)</td><td>Wall friction angle, δ</td><td>Dilatancy angle, ψ</td></tr>
<tr><td colspan="2">18.8</td><td>0^o</td><td>95.8</td><td>22^o</td><td>0^o</td></tr>
<tr><td colspan="6">Displacement Parameters</td></tr>
<tr><td>R_{int}</td><td>Strain, ε_{50}</td><td>Failure ratio, R_f</td><td>E_{50ref} (MPa)</td><td>E_{urref} (MPa)</td><td>Poisson's ratio, v</td></tr>
<tr><td>0.70</td><td>0.0075</td><td>0.95</td><td>14.4</td><td>43.1</td><td>0.45</td></tr>
</table>

The interface (wall) friction angle of 22^o is intended to represent the interaction between the pea gravel and concrete, and matches an assumed value from Romstad *et al. (*1995); there was no test data to support this value. Following the PLAXIS manual, dilatancy angle for the HS model was chosen to be ψ□□□0^o (Vermeer and Brinkgreve, 1998). There were no measurements of the interface friction/adhesion during the UCD test. As such, the value of the interface strength reduction parameter was chosen as $R_{int} = 0.70$ based on trial-and-error, which gave good matches with experimental (lateral load-displacement) data, as well as the LSH prediction, which is based on $\delta = 22^o$, and $c = 95.8$ kPa.

The domain extent and boundary conditions of the finite element models of the UCD test were identical to those of the UCLA test; except for the lateral extent (i.e., the width) of the three-dimensional mesh, which was set to be 3.05 m to match the UCD field-test configuration. Combined results of these simulations are displayed in Figure 3.6, where good agreement between measured data and simulation models can be observed.

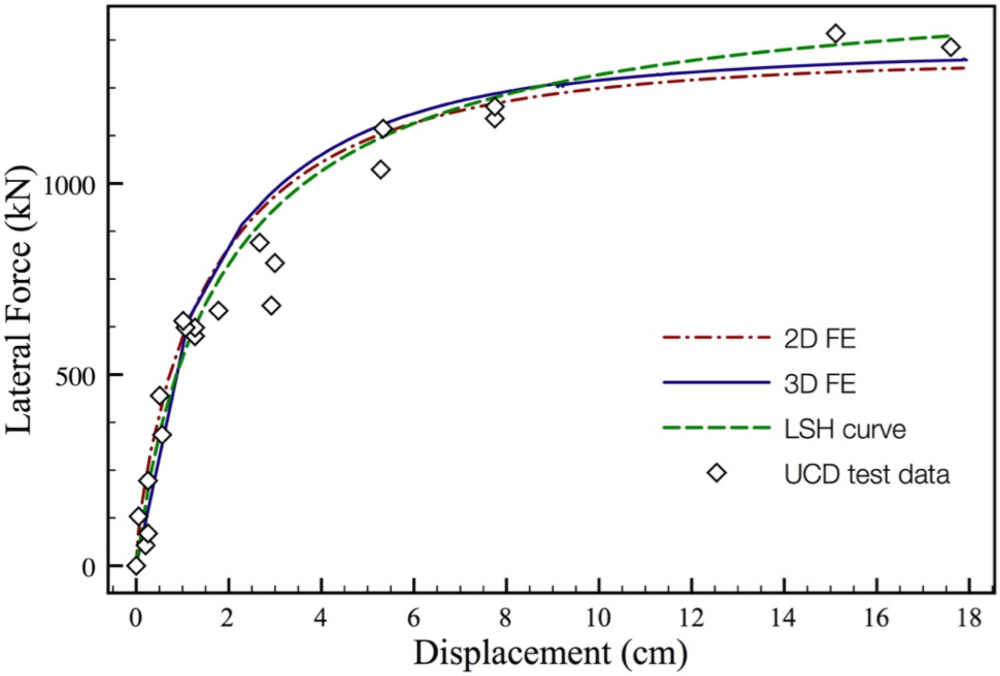

Figure 3.6 Measured and simulated lateral load-deformation curves for the UCD test (Shamsabadi *et al.*, 2010).

3.3 Extended hyperbolic force-displacement (EHFD) relationships

As demonstrated above by Shamsabadi *et al. (*2010), both LSH and FE models are capable of reproducing experimentally observed results. Nevertheless, neither model is readily amenable for routine design. This is because the construction of a finite element model of a bridge—complete with its abutment backfill—is laborious and computationally expensive; and the LSH model cannot directly be coupled with the structural model of a bridge. As such, Shamsabadi *et al. (*2010) proposed the use of a simple relationship between the lateral load per unit width of the abutment backwall (F) and the lateral displacement (y) for backfills tested by UCLA and UCD. They were also able to extend this relationship to different wall heights. This Extended Hyperbolic Force-Displacement relationship (EHFD) is given by

$$F(y)=\begin{cases}\dfrac{410.6y}{(H/1\text{m})+1.867y}\left(\dfrac{H}{1\text{m}}\right)^{1.56}, & y\le 0.05H \quad \text{(UCLA's silty sand backfill)},\\[2ex] \dfrac{249.1y}{(H/1\text{m})+0.8405y}\left(\dfrac{H}{1\text{m}}\right)^{1.05}, & y\le 0.10H \quad \text{(UCD's clayey silt backfill)}.\end{cases} \tag{3.4}$$

Figure 3.7 displays the backbone curves calculated using the EHFD relationship above along with the UCLA and UCD experimental data (for *H*=1.67 m) and LSH simulations for *H*=1.0-2.5 m. The agreement between the EHFD and LSH results is seen to be very good across the range of considered wall-heights and lateral displacements. The comparison with experimental data is also favorable.

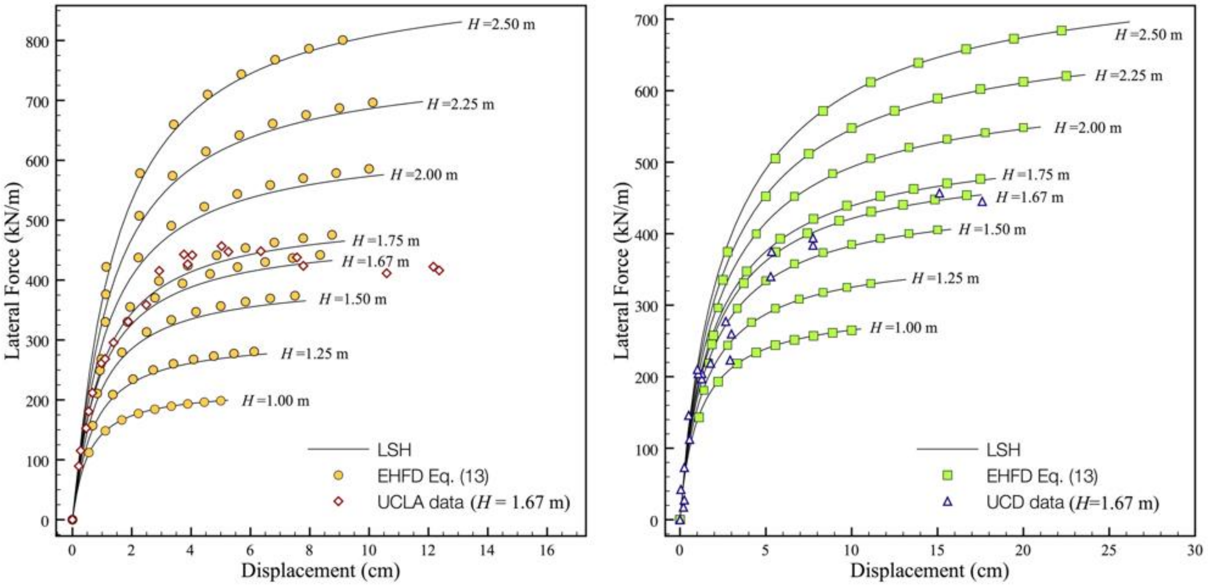

Figure 3.7 Measured and FE/LSH-simulated lateral load-deformation curves for the UCD test.

3.4 Description of the finite element models and their validation

The software package “Plaxis 3D Foundation” (Brinkgreve and Broere, 2008) was used for FE simulations of all the non-rotating walls in the present study. Test data by Stewart *et al.* (2007), henceforth referred to as the “UCLA test,” were used to validate various aspects of these FE models. All models featured 15-noded quadratic wedge elements to avoid locking. The models prepared for this study typically had approximately 50,000 elements (i.e., 360,000 degrees of freedom), which afforded adequate resolutions of the backfill failure mechanism. A representative model is shown in Fig. 3, which represents a bridge with a 60-deg skew, and 60 ft-wide deck. Other modeling details and the simulation results are presented next.

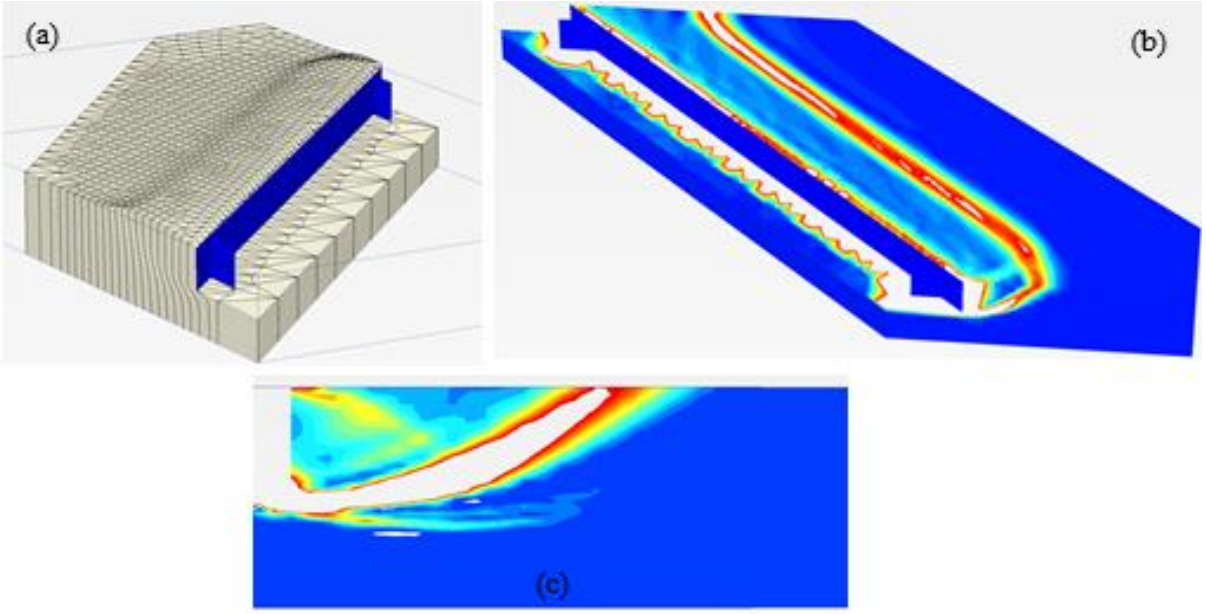

Figure 3.8 Typical finite element model used in the present study comprising 53,000 elements: (a) backfill deformations (exaggerated), (b) deviatoric strain distribution plot within the backfill, which indicates the failure surface formation, (c) the side-view of the same.

3.4.1 Constitutive model for the backfill

The soil constitutive model for the backfill is arguably the most critical ingredient of the FE simulations. In this study, the 'Hardening Soil' (HS) model available in Plaxis for both two- and three-dimensional FE simulations was chosen, because the HS model was observed to provide results that were more consistent with field test measurements than the basic Mohr-Coulomb and Drucker-Prager plasticity models. The HS model is an extension of the well-known hyperbolic model by Duncan and Chang (1970) for which the ceiling values for stress are described in similar fashion to the Mohr-Coulomb model, through the friction angle φ, the soil cohesion c, and the dilatancy angle ψ. On the other hand, the HS model requires three different input stiffness values—namely, the triaxial stiffness E_{50}, the triaxial unloading stiffness E_{ur}, and the oedometer loading stiffness E_{oed}. With these parameters, the model takes into account the dependence of stiffness moduli on the stress level (unlike the Mohr-Coulomb model, which neglects this variability), and all three moduli (E_{50}, E_{ur}, E_{oed}) grow with increasing pressure (Schanz *et al.*, 1999).

3.4.2 Interface elements

In order to model the frictional contact between the abutment backwall and the backfill soil, interface elements with eight-node pairs available in Plaxis 3D Foundation v.2 were used. Each interface element has zero thickness, and is defined by a simple bilinear stress-strain relationship, which describes the response of the backfill-backwall interaction element. This bilinear relationship comprises the classical Coulomb friction model combined with linear elastic loading/unloading rules, and is valid for small displacements and plastic-slip values. The maximum friction angle modeled the structural wall elements and the backfill soil model was 35 degree. The elements used were zero thickness 8 node, node paring the backfill and the structural elements. For further details on the interface elements used in Plaxis models one can refer to Shamsabadi et. al JBE 2010, and Plaxis 3D Foundation reference manual.

3.4.3 Validation of FE models with data from a full-scale abutment test

The material and interface model properties used in the present FE model had been validated by Shamsabadi *et al. (*2010) using data from the UCLA test. The calibrated material properties as well as comparisons with measured lateral load-deflection curves from the said validation effort will be repeated here for the reader’s convenience.

As described by Stewart *et al. (*2007), this test involved a 4.6m-wide, 1.67m-high seat-type abutment wall pushed against a silty sand backfill compacted up to over 95% modified Proctor relative compaction (ASTM, 2009). The wall was configured to mimic a seat-type abutment and loading was applied through a cyclic displacement control protocol. The backwall was pushed laterally between two plywood boards that allowed the creation of a plane-strain condition. Inclined actuators, which were providing the necessary lateral forces, were used to suppress any vertical movement. The loading protocol was designed to avoid any separation between the concrete abutment wall and the backfill soil. After the backfill capacity was reached, half of the backfill was excavated in order to visually identify the failure surfaces. The ultimate, hence the deepest, failure surface extended down from the bottom edge of the abutment wall and reached the backfill ground surface. The horizontal distance from the wall to where the failure surface met the ground surface extended to approximately three times the height of the backwall in a log-spiral shape.

The calibrated (Plaxis) HS model parameters for this test are shown in Table 3.4. Some of these parameters (cohesion, internal friction angle, density, elastic moduli) were obtained from laboratory (e.g., triaxial) testing, whereas the others were selected initially from literature-suggested values, and were subsequently iteratively adjusted.

Table 3.4 List of material parameters for Plaxis "Hardening Soil" and LSH models for the UCLA test.

<table>
<tr><th colspan="6">Strength Parameters</th></tr>
<tr><th>Unit weight, □□□(kN/m^3)</th><th colspan="2">Friction□□angle, □□ □□deg)</th><th>Cohesion, *c* (kPa)</th><th>Wall friction angle □deg)</th><th>Dilatancy angle (deg)</th></tr>
<tr><td>20</td><td colspan="2">40</td><td>14</td><td>20</td><td>10</td></tr>
<tr><th colspan="6">Other Parameters</th></tr>
<tr><th>R_{int}</th><th>Strain, □$_{50}$</th><th>Failure ratio, R_f</th><th>E_{50} (MPa)</th><th>E_{ur} (MPa)</th><th>Poisson's ratio, v</th></tr>
<tr><td>0.50</td><td>0.0035</td><td>0.97</td><td>70</td><td>140</td><td>0.3</td></tr>
</table>

The shapes and sizes of backfill failure surfaces, as well as the lateral load-displacement curves were well captured by the FE model (Figs. 4a, 5). The lateral total capacity of the abutment backfill was 2200 kN, which is approximately 477 kN/m (per unit wall width). Capacity was reached at a lateral displacement of 5 cm (3% of abutment height). The residual capacity was 442 kN/m and was measured at a lateral displacement of 8.5 cm (5% of abutment height). This brought about the residual capacity of 265 kPa (per unit wall area). Fig. 5 displays the computed lateral load-displacement backbone curve, which mimicked the UCLA test both for capacity and initial stiffness.

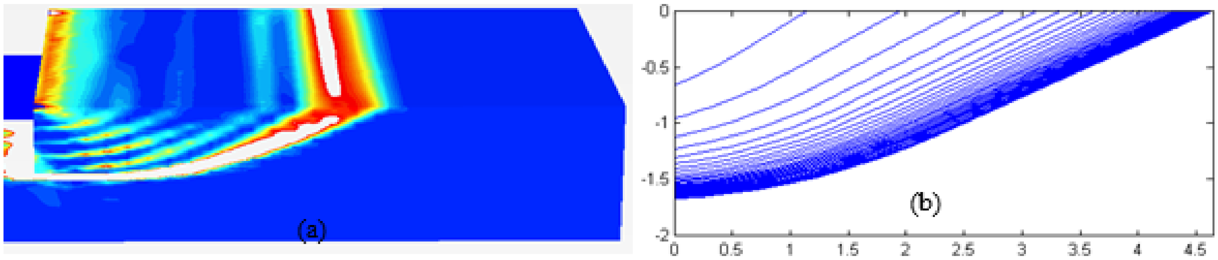

Fig. 3.9 (a) Incremental deviatoric strain distribution for a straight 15ft-wide wall obtained using Plaxis, and (b) failure surfaces obtained with the LSH model described in Shamsabadi *et al. (*2007).

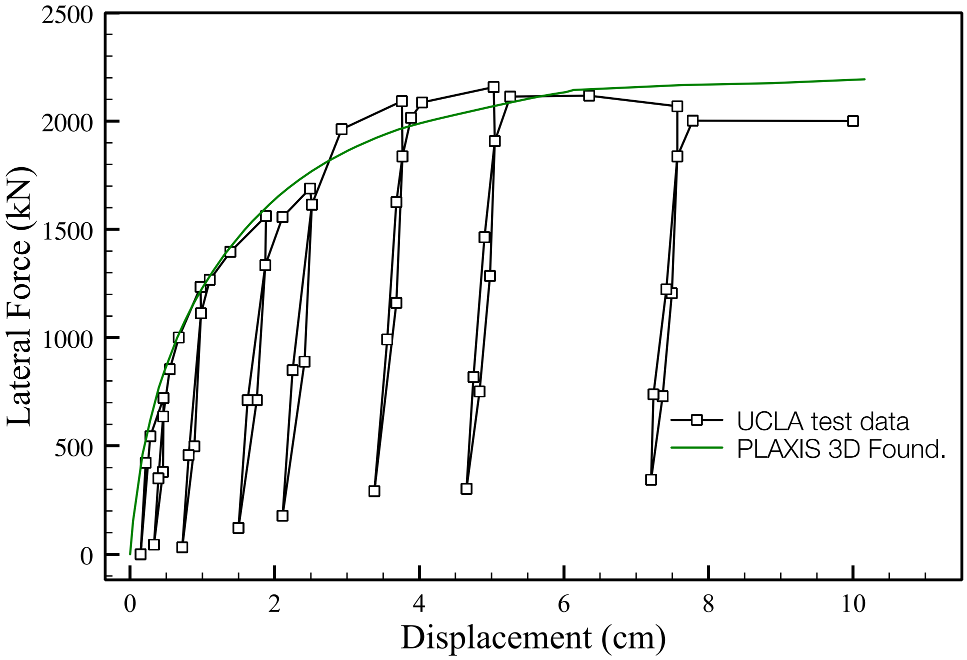

Fig. 3.10 UCLA full-scale test results (see Stewart *et al.*, 2007) for a 5.5ft-high wall and numerical results from Plaxis 3D Foundation.

3.4.4 Verification of FEM results with a semi-analytic limit equilibrium model

Using the validated FE model, several new FE models were generated. The new models were identical to the original model, except that they had different wall widths. The objective of this study was twofold: (*i*) to determine how the backbone curves change/scale with wall-width, and (*ii*) to verify the FE model against a well-established (and validated) limit equilibrium model that was devised for straight abutments.

The aforementioned limit equilibrium model is the Log-Spiral-Hyperbolic (LSH) model described in Shamsabadi *et al. (*2007). The LSH model is a plane-strain model that utilizes a kinematic hypothesis regarding the shape (a log-spiral curve) of the soil failure surface(s). This model was validated against various field and centrifuge test data (see Shamsabadi *et al.*, 2010). The specific material parameters of the LSH model for the UCLA test are also shown in Table 1. Figure 4b displays the mobilized failure surfaces computed using the LSH model for the UCLA test. These surfaces match very well with both Plaxis results and the measurements taken after the excavation of the backfill at the test site (see Stewart *et al.*, 2007). Deeper failure surfaces correspond to larger lateral wall displacements. As the lateral resistance approaches ultimate capacity in both LSH and Plaxis simulations, new failure surfaces form in the immediate vicinity of the previous ones with diminishing separation towards the ultimate failure surface; therefore the rupture lines are concentrated near the bottom-end of the backwall.

The LSH model calibrated for the UCLA test—which had a backwall width of 4.57 m (15 ft)—was then used in subsequent simulations wherein all model parameters were kept constant, except the wall width, which was varied from 4.57 m to 36.58 m. Widths less than 4.57 m were not explored because they are too narrow to encounter in actual bridges. A total of 47 such simulations were carried out in this backwall width range (more-or-less uniformly spaced). The same model matrix was also evaluated using Plaxis.

Figure 6 displays backbone curves for some of these simulations, wherein it can be seen that the results from LSH and Plaxis are very consistent. Furthermore, the shapes and extents of the failure surfaces predicted in both the LSH and Plaxis simulations are also consistent (as seen in Fig. 4, for example). In both LSH and Plaxis simulations, the ultimate failure surface is observed to intersect the ground line at approximately at 4.7 m away from the wall. This distance is more-or-less constant for *all* wall-widths. Since the wall-height was constant in all these simulations, which was 1.67 m (5.5 ft), it is fair to state the failure surface reaches the ground level at approximately 3 times the wall-height, regardless of the wall-width (at least for the present plane-strain case with UCLA soil—i.e., Table 3.1).

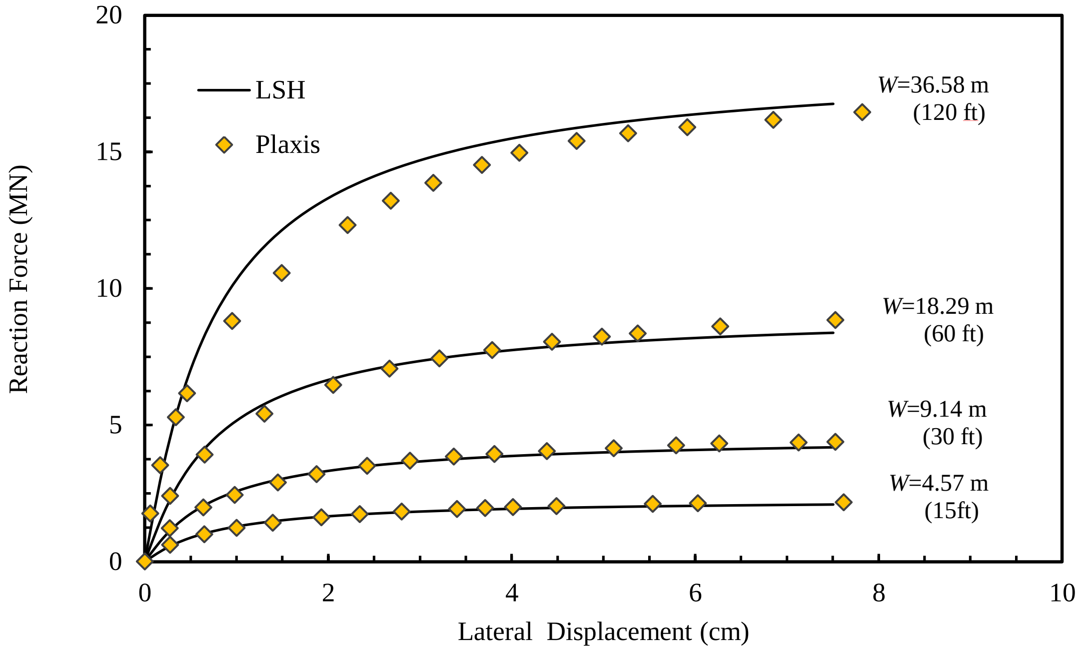

Fig. 3.11 Lateral load-displacement backbone curves obtained from FE simulations (Plaxis 3D Foundation) for straight abutments with different widths, and those obtained using the Limit State Hyperbolic (LSH) method.

The results of the aforementioned simulations suggest that FE Models can be used for geometries and loading conditions other than those that were tested, or simulated using LSH. In particular, with all other parameters being the same, it is fair to state that Plaxis will produce accurate predictions when the wall skew angle is changed from zero to other values. Such parametric studies will be presented next, and those results will be used to develop lateral load-deflection relationships for skew abutments.

Chapter 4

Behavior of Skew Bridge Abutments under Lateral Translations

4. Behavior of Skew Bridge Abutments under Lateral Translations

The objective that will be pursued in this chapter will be to tackle the relatively restricted case of the lateral—and *only* lateral—movements of a skew abutment's backwall. The objective is to obtain a closed-form expression for lateral behavior that is, by-and-large, based on physical parameters. This expression will be derived using verified and validated high-fidelity three-dimensional continuum Finite Element (FE) models described in the previous chapter. It is expedient to note here that while such a model (i.e., one that only applies to non-rotating backwalls) may appear too restrictive at first, it will be extremely useful in two ways: (*i*) it will enable the development of a more complex model that is based on resultant-based plasticity (described in Chapter 5), by serving as an anchor point in that model's yield function; and (*ii*) it will directly yield the lateral behavior of a skew abutment that belongs to a bridge that is torsionally stiff in plan (e.g., a bridge with multiple bents).

Based on parametric studies using the validated numerical models, a simple relationship will be devised using regression techniques, which quantifies the effects of the skew angle on the lateral load-displacement backbone curve (and, incidentally, the lateral capacity). The veracity of the proposed relationship will be assessed against 3D FE results through a series of *blind* predictions, for which the model matrix comprises different combinations of wall widths and skew angles. Because the scenario of a backwall translating only laterally (i.e., no rotations or sidesway) is very unlikely, even for torsionally stiff bridges, a series of additional sensitivity studies are carried out. These studies provide a quantified understanding of how small rotations and sidesways can affect the backbone curve, and shed light on some of the findings from the recent study by Rollins and Jessee (2013), which was also discussed previously in Chapter 2.

4.1. Response correlations between straight and skew abutments

Using the LSH model—or the EHFD model presented in Shamsabadi *et al.* (2010), which provides the backbone curve in closed-form for different backfill properties and backwall heights—it is possible to obtain the backfill reaction for straight seat-type abutments. The method that will be described below will seek to utilize this information in predicting the response of a skew abutment (for any skew angle) that has the same backfill and backwall height.

The method is based on a simple conjecture: A skew version of a straight abutment will have *lower* capacity if the skew abutment has the *same wall length* as the straight one; and a skew version of the a straight abutment will have *higher* capacity if the skew abutment has the *same deck-width* as the straight one. This is true for *any skew angle* as long as the backwall is not allowed to rotate about the vertical axis. These lower and upper capacity curves are henceforth referred to as the *lower-bound* (LB) and the *upper-bound* (UB) backbone curves, respectively.

The conjecture above means that the two skew configurations will *bracket* the backbone curve of a straight abutment. That is,

$$F_{\mathrm{L}}(\Delta) \le F_{\mathrm{Straight}}(\Delta) \le F_{\mathrm{U}}(\Delta), \quad \text{and incidentally (as } \Delta \to \infty) \quad F_{\mathrm{L}}^{\mathrm{ult}} \le F_{\mathrm{Straight}}^{\mathrm{ult}} \le F_{\mathrm{U}}^{\mathrm{ult}} \tag{4.1}$$

where F_{L} and F_{U} denote the lower and upper-bound lateral passive abutment reactions, and Δ denotes the lateral displacement. This conjecture is tested and demonstrated with three separate Plaxis simulations in Figure 4.2 using the UCLA test's backfill properties. The non-skew configuration's wall width was 9.1 m (30 ft), which corresponds to a typical two-lane bridge. The skew angles for both the upper and lower curves were set at 60 degrees.

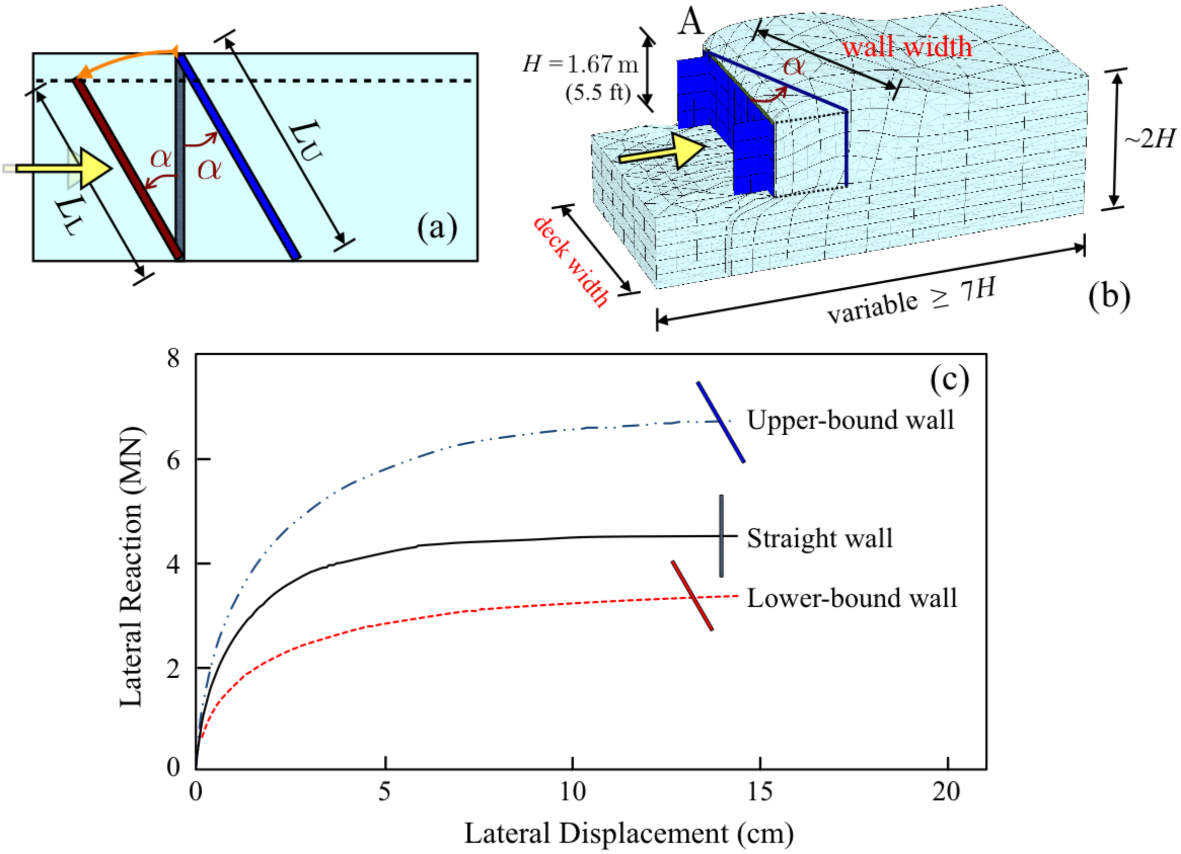

Fig. 4.1 (a) Schematic plan of the straight abutment and two bounding skewed models for α degrees in the generic configuration of (b) straight/skew abutment FE meshes; (c) backbone curves for a straight abutment (middle curve) with 9.1 m length, a 60-degree skew abutment with the same deck width (upper curve), and a 60-degree skew abutment with the same backwall width (lower curve) are also shown (all abutments have "UCLA backfill").

The veracity of the conjecture is further examined by carrying out parametric studies with various skew angles. The results (shown in Fig. 4.2 and Table 4.1) indicate that the conjecture is valid for skew angles ranging from 15 to 60 degrees and for any abutment width. As expected, Fig. 4.2 also demonstrates that the UB and LB curves approach the straight abutment curve as the skew angle decreases (obviously, for a 0-degree skew angle, all three curves are identical). An interesting observation is that the straight abutment curve appears to be *almost* an average of the UB and LB curves. Nevertheless, since this assertion is not necessarily correct for all skew angles (see the UB and LB capacities for the 60degskew walls shown in Fig. 4.2(b) as well as the values displayed in Table 4.1). As such, it is necessary to explore the optimal weight(s) for averaging the LB and UB curves.

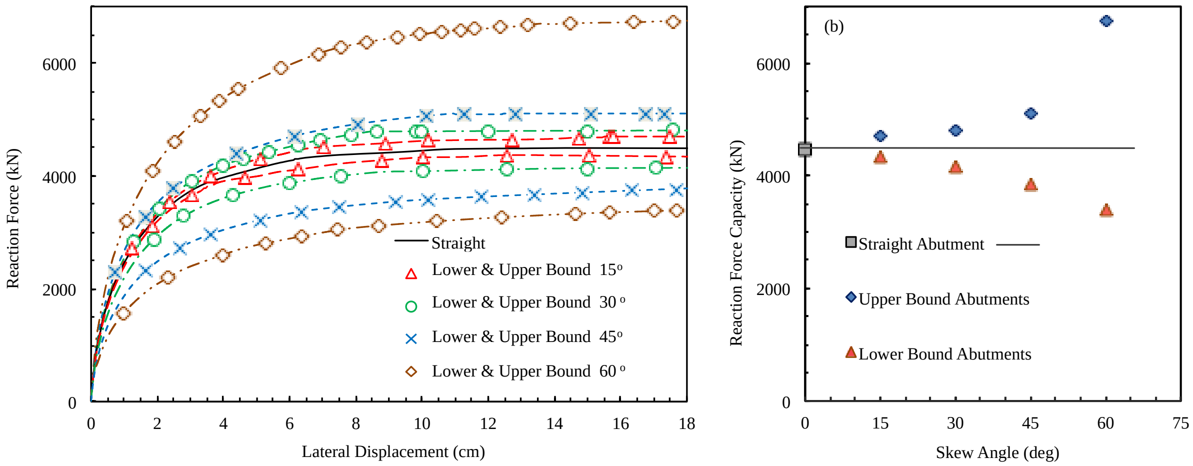

Fig. 4.2 Response for various skew angles of a 30 ft-wide abutment: (a) backbone curves, (b) capacities.

Table 4.1. Ultimate Capacities (kN) vs. different wall widths and skew angles for the study analysis matrix, including the nominal (0 degree skew wall) and the upper bound and lower bound limits for each skew angle.

α ***W***	**0°**		**15°**	**30°**	**45°**	**60°**
4.6m (15ft)	2157.5	**UB**	2313.2	2357.7	2735.8	3234.0
		LB	2081.9	2032.9	1783.8	1592.5
9.1m (30ft)	4470.6	**UB**	4693.1	4799.8	5102.3	6752.7
		LB	4350.5	4159.3	3856.8	3398.6
13.7m (45ft)	7001.8	**UB**	7357.7	7468.9	7891.5	10556.0
		LB	6254.4	6049.8	5947.5	4844.3
18.3 (60ft)	9390.6	**UB**	10044.5	10097.9	11254.4	14074.7
		LB	8887.9	8585.4	7664.6	7415.5
22.9m (75ft)	12228.6	**UB**	12677.9	13549.8	14653.0	16975.1
		LB	11886.1	11748.2	9243.8	8105.0
27.4m (90ft)	14470.6	**UB**	15062.3	15742.9	17139.7	21859.4
		LB	14012.5	13545.4	11752.7	11000.9
32m (105ft)	17268.7	**UB**	18669.9	19172.6	19715.3	24853.2
		LB	17086.3	15742.9	14653.0	14070.3
36.6m (120ft)	19105.9	**UB**	20649.5	22375.4	24377.2	26814.9
		LB	19008.0	17629.0	16014.2	12464.4

Before making any further progress, it is important to note that even if an optimal weight can be determined, it is not yet possible to obtain/predict the backbone curve (or capacity) of a skew abutment, given the backbone curve (or capacity) of a straight abutment, which is the objective here. To do so, we must first establish a relationship between the UB and LB backbone curves (and/or capacities). For this purpose, a second conjecture is put forth: *The capacities of the UB and LB curves scale linearly*. To wit,

$$\mathrm{CPW}(\alpha) \equiv \frac{F_{\mathrm{U}}^{\mathrm{ult}}}{L_{\mathrm{U}}} \approx \frac{F_{\mathrm{L}}^{\mathrm{ult}}}{L_{\mathrm{L}}} = \frac{F_{\mathrm{L}}^{\mathrm{ult}}}{L_{\mathrm{U}} \cos\alpha} \quad \Rightarrow \quad F_{\mathrm{U}}^{\mathrm{ult}} \cos\alpha \approx F_{\mathrm{L}}^{\mathrm{ult}} \tag{4.2}$$

where CPW(α) denotes *Capacity Per unit Wall-length* for a given abutment with α degrees of skew. If this conjecture is true, then it will be possible to relate the capacities of UB and LB backbone curves to each other.

This second conjecture can be tested by examining the variation of a dimensionless parameter, dubbed here as Mutual Capacity Ratio (MCR), which is defined as $\mathrm{MCR}_{ij}^{\alpha} \equiv \mathrm{CPW}_{i}^{\alpha} / \mathrm{CPW}_{j}^{\alpha}$. Ideally, if there are no distorting factors (e.g., the boundary effects due to the presence of wingwalls) then MCR_{ij} will be equal to 1 for any wall length (different values indexed by *i*'s and *j*'s here). Fig. 4.3 displays the MCR values computed for different wall-widths and skew angles, wherein the diagonal elements (MCR_{ii}) have unit values, by definition. As seen, the largest violations of the second conjecture are bounded from below and above by approximately 15%. For most of the important cases (i.e., backwall lengths larger than 15 m and skew angles less than 45 degrees) the second conjecture is even stronger (i.e., ±10% or less).

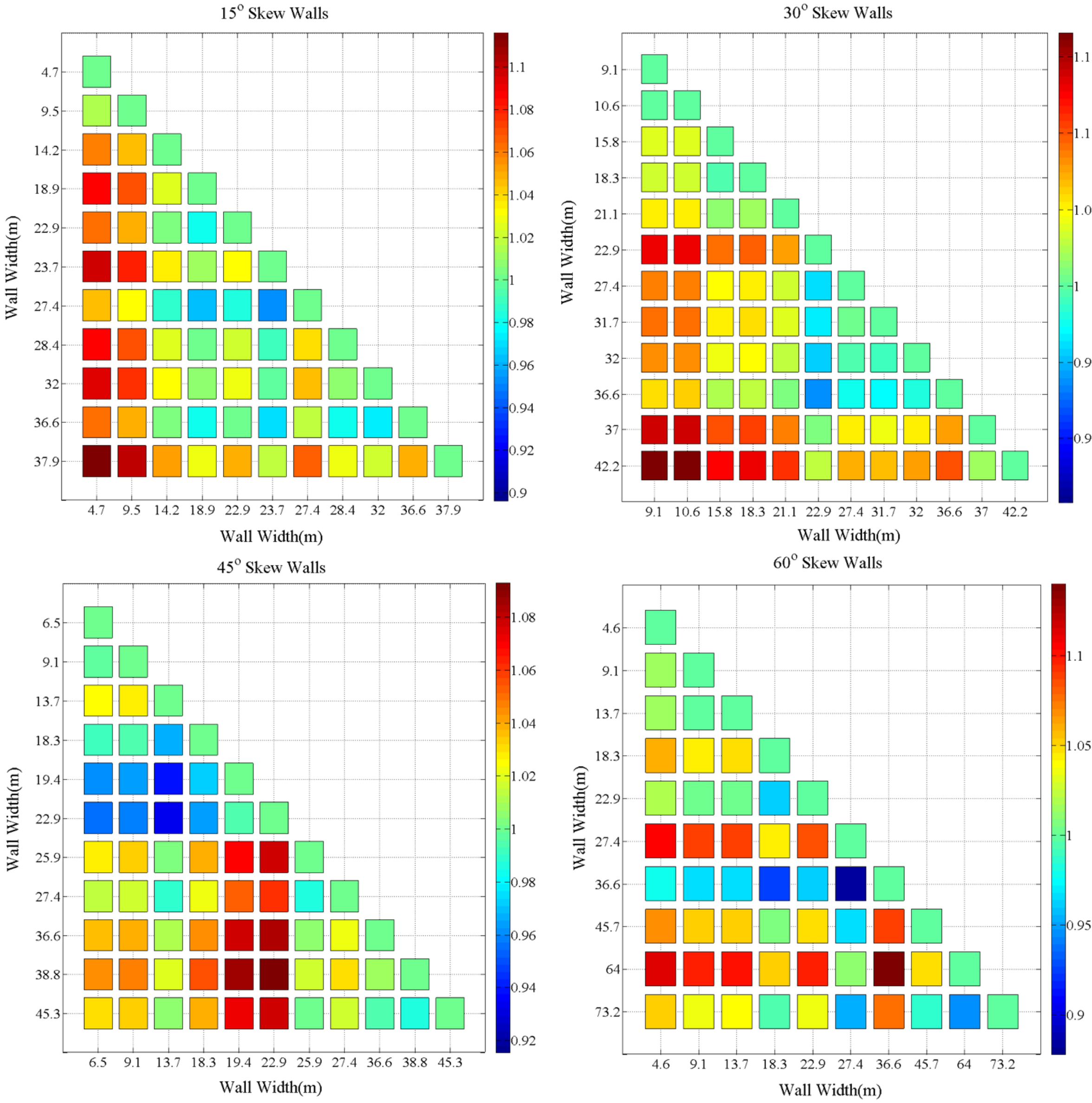

Fig. 4.3 Mutual Capacity Ratio (MCR) values for different skew angles.

4.1.1 Correlation parameter λ

With the two conjectures in hand, it is now possible to formulate a direct relationship between (*i*) the lateral capacities and load-displacement curve of a straight wall and (*ii*) the lateral capacities and load-displacement curve of a skew-angled version, given any angle *α*, in combination with height and backfill soil properties.

To achieve this, we first introduce the weight (or mixing) λ parameter. There will be two different versions of λ in this study: One obtained from capacity-only considerations, and another by considering the entire backbone curves. Starting with the capacity-based version, we define λ through the weighted sum:

$$F^{\text{ult}}_{\text{Straight}} \approx \lambda F^{\text{ult}}_{\text{L}} + (1-\lambda)F^{\text{ult}}_{\text{U}} \tag{4.3}$$

Eq. (4.3) also implies

$$\begin{aligned} & F^{\text{ult}}_{\text{Straight}} \approx \lambda \cos\alpha F^{\text{ult}}_{\text{U}} + (1-\lambda)F^{\text{ult}}_{\text{U}} = \left[1+(\cos\alpha-1)\lambda\right]F^{\text{ult}}_{\text{U}} \\ \Rightarrow \quad & F^{\text{ult}}_{\text{U}} \approx \left[1+(\cos\alpha-1)\lambda\right]^{-1} F^{\text{ult}}_{\text{Straight}} \end{aligned} \tag{4.4}$$

where the substitution was made from Eq. (4.2). Therefore, Eq. (4.4) represents a relationship between the capacity of a straight wall and a skew-angled version of it. Given the capacity of a straight abutment, a skew angle α, and appropriate value of the mixing parameter λ, Eq. (4.4) will yield the capacity of its skew-angled version. It is now only a matter of finding the appropriate values of λ, which inevitably vary with respect to wall width and skew angle. However, as discussed above in conjunction with the findings presented in Figure 4.2 and Table 4.1, it may be possible to obtain a single optimal value of λ that works well for *all* wall widths and abutment skew angles. This can simply be achieved by defining the minimization problem:

$$\min_{\lambda} e_{\text{ult}}(\lambda) \equiv \left(F^{\text{ult}}_{\text{Straight}} - \left[\lambda F^{\text{ult}}_{\text{L}}(\alpha) + (1-\lambda)F^{\text{ult}}_{\text{U}}(\alpha)\right]\right)^2 \tag{4.5}$$

This is a linear least-squares problem and the optimal λ value (denoted by λ^*) is simply,

$$\left.\frac{\partial e_{\text{ult}}}{\partial \lambda}\right|_{\lambda=\lambda^*} = 0 \quad \Rightarrow \quad \lambda^* = \frac{F^{\text{ult}}_{\text{Straight}} - F^{\text{ult}}_{\text{U}}(\alpha)}{F^{\text{ult}}_{\text{L}}(\alpha) - F^{\text{ult}}_{\text{U}}(\alpha)} \tag{4.6}$$

The approach presented above to determine a capacity-based optimal value for λ could also be applied equally to the *entire backbone curve*. In other words, a single/optimal value of λ can be obtained, which approximates the *entire* backbone curve of the skew abutment (not just its capacity value) using that of its corresponding straight abutment. This version of λ can be computed by minimizing

$$e_{\text{backbone}}(\lambda) \equiv \sum_i \Big(F_{\text{Straight}}(\Delta_i) - \big[\lambda F_{\text{L}}(\alpha, \Delta_i) + (1-\lambda) F_{\text{U}}(\alpha, \Delta_i) \big] \Big)^2 \tag{4.7}$$

where Δ_i denotes the discrete values of lateral displacement at which the nominal, upper and lower-bound backbone curves are sampled. Again, this is a linear least-squares problem. The optimal λ value (denoted by $\lambda^{\#}$) is simply,

$$\begin{aligned} &\left.\frac{\partial e_{\text{backbone}}}{\partial \lambda}\right|_{\lambda=\lambda^{\#}} = 0 \quad \Rightarrow \\ &\lambda^{\#} = \frac{\sum_i \Big(\big[F_{\text{Straight}}(\Delta_i) - F_{\text{U}}(\alpha, \Delta_i) \big] \big[F_{\text{L}}(\alpha, \Delta_i) - F_{\text{U}}(\alpha, \Delta_i) \big] \Big)}{\sum_i \big(F_{\text{L}}(\alpha, \Delta_i) - F_{\text{U}}(\alpha, \Delta_i) \big)^2} \end{aligned} \tag{4.8}$$

It is expedient to note here that all three curves in Eq. (4.8) are generated through 3D FE simulations with force-control and automated sub-incrementation to achieve convergence in equilibrium iterations. As such, they will not necessarily be sampled at identical displacement increments. Therefore, in order to achieve constant displacement increments, we carried out simple searches to bracket and linearly interpolate the needed capacities between those that were directly obtained from the 3D FE simulation.

Optimal λ values given by Eqs. (4.6) and (4.8) (i.e., capacity- and backbone-based, respectively) are shown in Figure 4.4. As suggested earlier, for both cases, most of the optimal λ values are clustered around 0.5. Also, according to the definition based on capacities only (Eq. 4.6), it is always guaranteed that the optimal value is bounded as $0 < \lambda^* < 1$. This is confirmed by results shown in Figure 4.4(b). On the other hand, for the backbone-based definition, there are cases in which $\lambda^{\#}$ can reach magnitudes higher than one. This means the straight abutment's backbone curve intercepts the upper-bound backbone curve somewhere before the plateau region. It is useful to note that this only occurred for the wall that had the lowest skew angle and the largest wall length (i.e., the 15^{o} and 40 m abutment in Fig. 4.4.a).

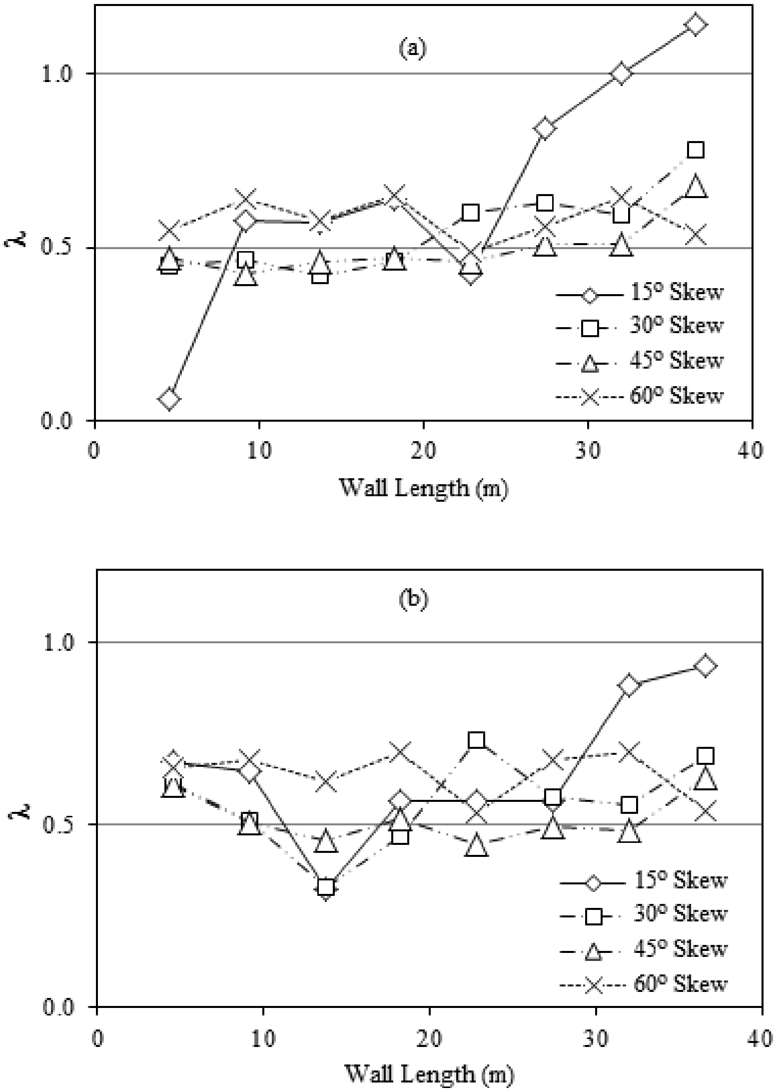

Fig. 4.4. Optimal λ values computed using least-squares minimization on (a) complete backbone curves, and (b) lateral capacities.

4.2 Sensitivity intervals

Optimal *λ* values shown in Figure 10 do not provide the full picture by themselves. It is also necessary to determine how sensitive the least squares fits are to variations in the values of *λ*. These sensitivities are computed and presented in the form of 90% and 95% *sensitivity intervals*. A 95% sensitivity interval indicates that the values of *λ* within this bracket produce a variation of ±2.5 at most, in the objective function value. The said intervals are shown in Figures 4.5 and 4.6 for the capacity- and backbone-based *λ* values, respectively.

As seen, for lower skew-angles the sensitivity intervals are larger, which implies that all three (UB, LB, and Straight) response curves are already very close to each other. It can also be deduced from these figures that there is no single *λ* value that falls within even the looser (i.e., 90%) sensitivity interval that provides a good fit for *all* skew angles and wall widths. Nevertheless, it is still possible to produce an acceptable single/constant *λ* value, as described next.

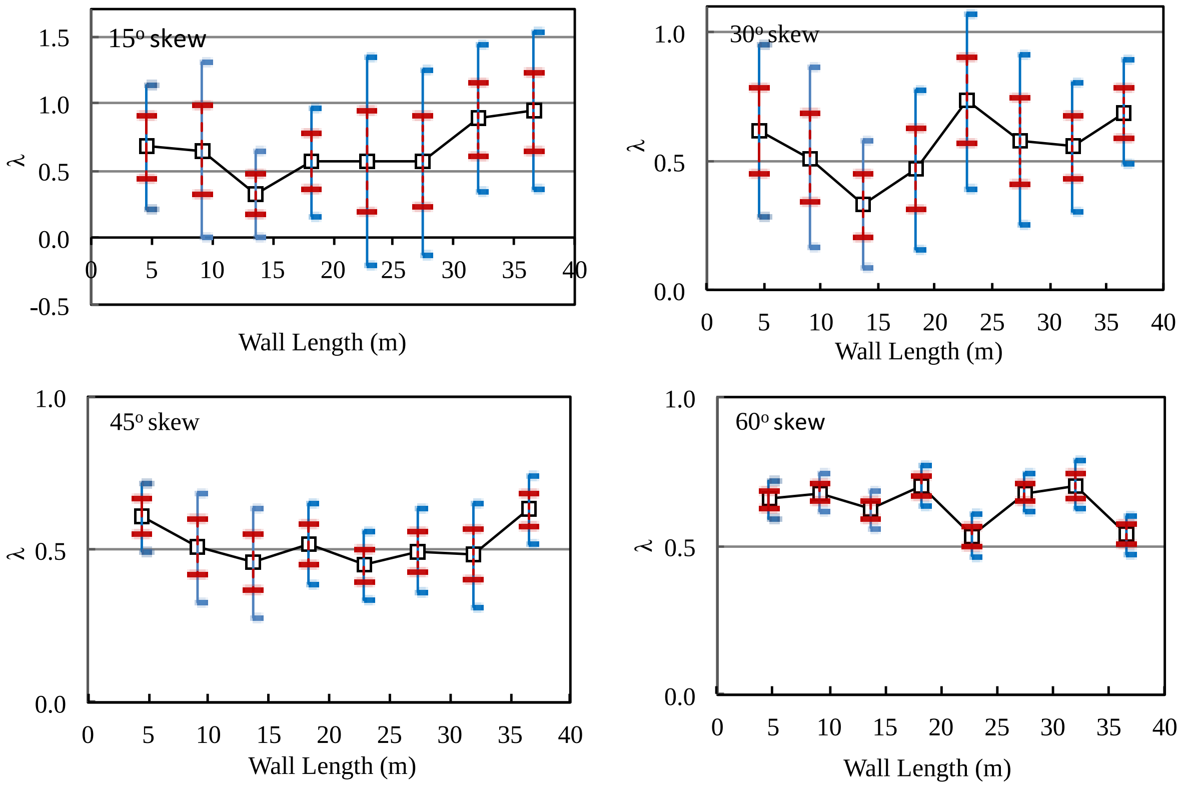

Fig. 4.5 Capacity-based λ values and their 90% and 95% sensitivity intervals.

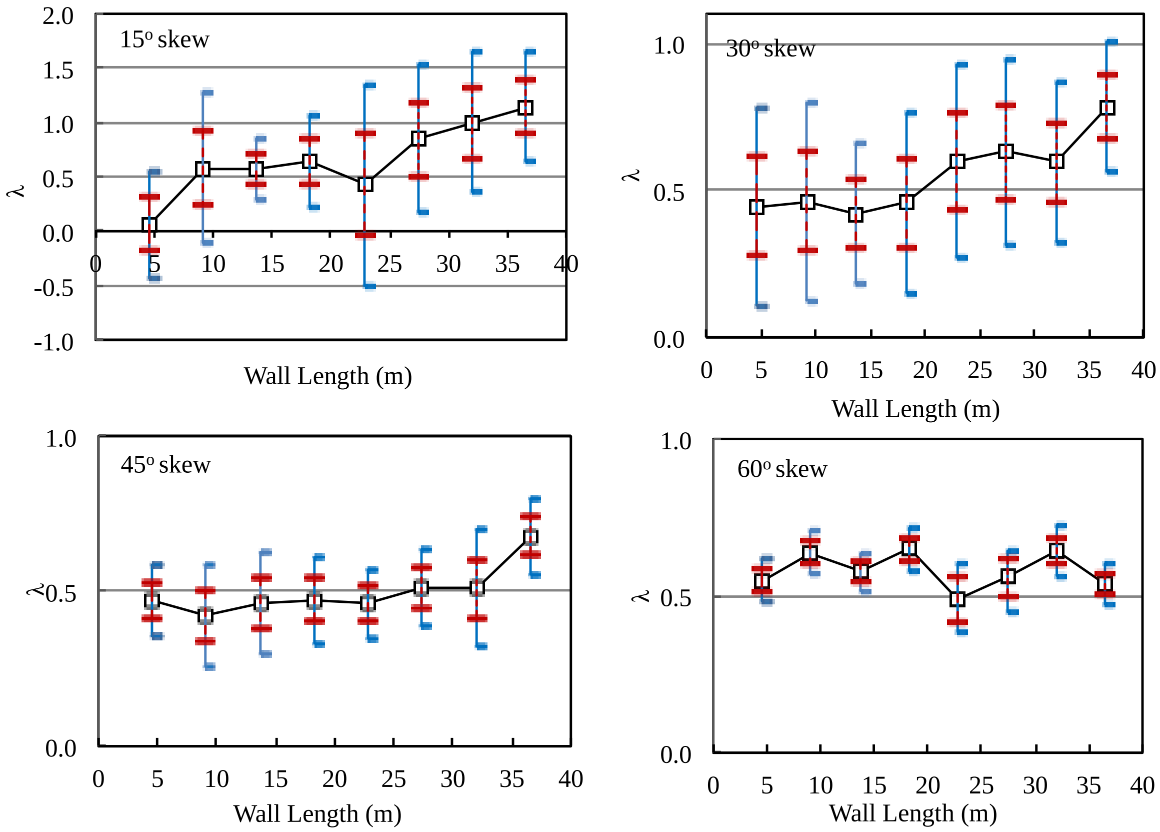

Fig. 4.6 The variation of λ's determined through least square minimization of the entire backbone curves and their 90% and 95% sensitivity intervals (i.e., broader and narrower brackets in the figure, respectively) with skew angle and wall width.

4.3 A recommended λ value for engineering practice

Although an optimal λ within the 90% confidence interval was not achieved, it is still possible to introduce a single/constant λ value that will provide the minimum possible error when estimating the capacity and backbone curve of a skew-angled bridge (i.e., a pareto-optimal λ). This value can be computed by using the optimal λ's (and their corresponding objective function values) obtained for each skew angle and abutment wall length combination. As stated earlier, this single λ value will not be within the 90% sensitivity interval for *all* cases, but it can be devised to work very well for most commonly encountered deck widths (> 10 m or 30 ft) and skew angles (< 45°).

To compute the pareto-optimal value of λ, we used three different minimization methods, results of which are shown in Figure 4.7. The curve marked as "L_1 norm" indicates the values of an error function, which was devised by simply adding the absolute values of the differences between the candidate pareto-optimal λ (the *x*-axis on Fig. 4.7) and those *optimal* λ values that are shown in Figure 4.5. The alternative approach was to relax the requirements and only to insist on minimizing the L_1-distance between the pareto-optimal λ and those λ values that resided within the 90% sensitivity interval (i.e., the L_1-distance for a candidate pareto-optimal λ is measured from the closest edge of this interval; and if candidate pareto-optimal λ is already within the interval, then its L_1-distance is set to zero). This objective function's value with respect to λ is marked as the "L_1 + Dead Zone minimization" on Figure 4.7. The third and final approach was to introduce a weighing scheme into the second method; and its objective function is given by,

$$e(\lambda) \equiv \sum_i w_i \left| \lambda - \lambda_i \right|, \qquad w_i \equiv 0.1 \Big/ \left(\lambda_i^{\text{90\%-ceiling}} - \lambda_i \right) \tag{4.9}$$

where $\lambda_i^{\text{90\%-ceiling}}$ denotes the ceiling value of the *i*-th optimal λ. This type of weight (w_i) gives more importance to narrower sensitivity brackets (while noting that the coefficient 0.1 is arbitrary and has no effect on the pareto-optimal λ value, and it is used merely to scale the objective function in Eq. 4.9).

The three approaches above yielded the pareto-optimal λ values as 0.550, 0.553, and 0.572, respectively. In view of many anticipated epistemic and aleatoric uncertainties associated with the present problem (e.g., uncertainties soil parameters and field compaction, finite element modeling errors, etc.), it is reasonable to round this number and use $\bar{\lambda}$ = 0.6 to predict the behavior of skew abutment walls using the curves estimated for straight abutments results (see, for example, Shamsabadi *et al.*, 2010; and Khalili-Tehrani *et al.*, 2010).

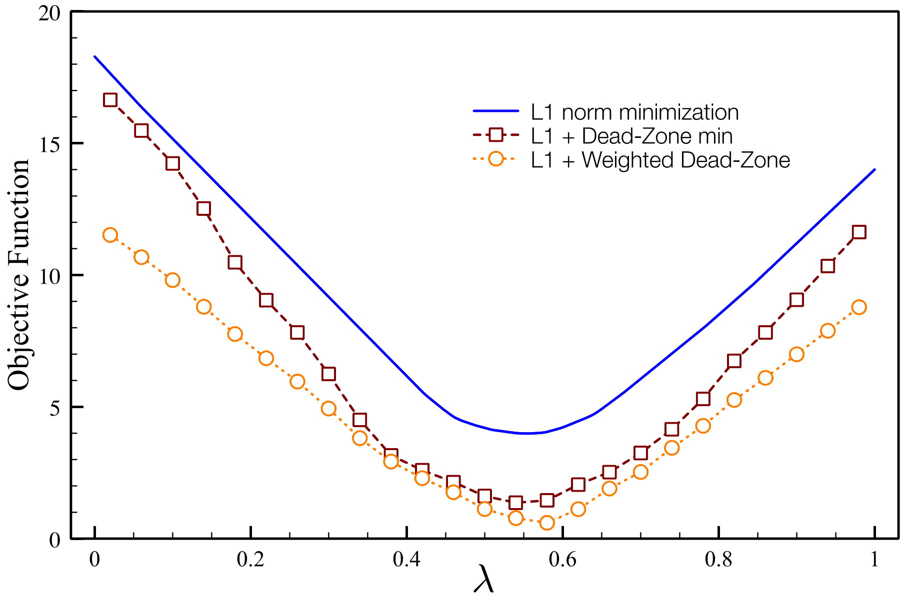

Fig. 4.7 Variation of L_1-norm, Dead-Zone L_1-norm, and weighted Dead-Zone L_1-norm objective functions with respect to λ. The pareto-optimal λ values correspond to the lowest point of each curve.

It should be noted that only the capacity-based optimal λ values (i.e., data from Figure 4.5) were used in the calculations above. Also, walls with 5 m wall-lengths as well as 60° skew angles were *all* included in the calculations. It goes without saying that a more accurate λ value (than 0.6) for a specific case can easily be obtained by finding the closest possible λ's from Figure 4.5 (or 4.6), and then by interpolating between these values.

4.4 Blind predictions

In order to assess of the accuracy of the proposed $\bar{\lambda} = 0.6$, some additional abutment configurations were studied. These are four *new* configurations that were not used as data in the optimization procedures described earlier, which include two wall lengths—i.e., medium (17.4 m) and wide (36.6 m)—and two skew angles—moderate (25°) and severe (55°). The results are shown in Table 4.3. For each case, the estimated upper and lower bound walls' capacities are calculated using the proposed $\bar{\lambda} = 0.6$ and Eq. (4), wherein the value $F_{\text{Straight}}^{\text{ult}}$ is computed using the LSH formulae described in Shamsabadi *et al. (*2010).

Another set of LB and UB estimates is provided by using λ values interpolated from data presented in Figure 4.5 (the interpolated λ's are shown in parentheses in Table 3). Also, exact values are calculated using FEM models for each case and displayed in Table 4.3 in order to gauge the accuracy of the aforementioned estimates. The relative error for each calculation is computed as $e_R = \left| F_{\lambda}^{\text{ult}} - F_{\text{FEM}}^{\text{ult}} \right| \Big/ F_{\text{FEM}}^{\text{ult}}$.

Table 4.2 Lateral capacity predictions for the blind tests to appraise the accuracy of using $\bar{\lambda} = 0.6$.

	Capacities (kN)												
α	0°			25°					55°				
Meth. / L_{wall}	LSH	FEM		LSH				FEM	LSH				FEM
				with $\bar{\lambda}$	e_R	with λ_{int}	e_R		with $\bar{\lambda}$	e_R	with λ_{int}	e_R	
36.6m **(120ft)**	17164	19105	**UB**	(0.6) 18186	12%	(0.77) 18498	11%	19359	(0.6) 25674	3%	(0.57) 25240	1%	24975
			LB	(0.6) 16482	7%	(0.77) 16768	6%	17797	(0.6) 14726	8%	(0.57) 14477	6%	13595
17.4m **(57ft)**	8153	8295	**UB**	(0.6) 8639	2%	(0.49) 8545	3%	8843	(0.6) 10956	7%	(0.65) 11279	4%	11746
			LB	(0.6) 7830	2%	(0.49) 7744	3%	7979	(0.6) 6284	2%	(0.65) 6469	1%	6391

As seen, the recommended $\bar{\lambda} = 0.6$ works nearly as well as the interpolated λ values. Moreover, the results appear to be adequately accurate with maximum relative error for predicted capacity being 12%. It is important to note that the values marked under the LSH columns are computed purely from closed-form formulae, i.e., by using Eq. (4), $\bar{\lambda} = 0.6$, and the formula provided for $F_{\text{Straight}}^{\text{ult}}$ in Shamsabadi *et al.* (2010)—or the more general version provided in Khalili-Tehrani *et al.* (2010)—which use the backwall height and soil data as input parameters. As such, these LSH calculations are instantaneous in comparison to 3D FEM simulations. Moreover, they can be used to obtain estimates of the complete backbone curves.

4.5 A sensitivity study on wall rotations and sidesway

In a recent study, Rollins and Jessee (2013) carried out a series of laboratory tests on skew angled abutments. In these tests, Rollins and Jessee kept the deck width constant, and pushed against compacted backfills, the compositions of which are similar to the soils considered in the present study, without allowing any rotations of the backwall. Their measurements indicated that the lateral capacity of the backfill decreased (quadratically) with respect to the skew angle. If indeed the abutment was not allowed to rotate (or sidesway) in these tests, then the results by Rollins and Jessee (2013) are in contradiction with the findings presented earlier in this study, since the simulations here indicated that the capacity should have increased!

Given this contradiction, we explored the sensitivity of the lateral capacities computed using the 3D FEM simulations with respect to small rotations and sidesways, in an attempt to understand the discrepancy between results obtained by 3D FEM simulations and the direct measurements by Rollins and Jessee.

For the sensitivity studies, we chose the deck-width and the abutment wall-height as 3.35 m and 1.67 m, respectively. These dimensions are larger than those tested by Rollins and Jessee (which were, respectively, 1.28 m and 0.91 m) and are incidentally identical to the wall tested by Stewart *et al.* (2007). The soil properties in the sensitivity simulations were the same as those presented earlier in Table 3.1, except the cohesion value was lowered to c = 7 kPa to match Rollins and Jessee’s nearly cohesionless backfill material. In order to study the effect of slight wall movements, a 45-degree skew abutment wall and its non-skew (straight) counterpart were investigated. For the skew-angled abutment, two types of backwall movements were considered: (*i*) rotation about the vertical axis, and (*ii*) sidesway. For all the studied cases, a 14cm lateral displacement was prescribed to the backwall. Along with this lateral movement, either a rotation or a sidesway was proportionally applied (for example, if the target maximum rotation or sidesway was set to 5 degrees, then this maximum rotation was simultaneously reached with maximum lateral displacement of 14 cm). It should be noted that often the lateral capacity was reached prior to reaching the target maximum displacement at which point the simulations were terminated, typically due to convergence issues (which are expected because even though the lateral wall displacement was prescribed, the majority of the finite element degrees of freedom were free, and thus, nonlinear equilibrium iterations were still needed).

Figures 4.8 and 4.9 display the results for various wall rotations and sidesways. It is clear that even small movements (in either mode) can reduce the lateral capacity to values below those exhibited by the corresponding straight abutment. This is the same trend observed by Rollins and Jessee in their tests. Even though Rollins and Jessee did not intend to allow any sideway movements or rotations to take place, they acknowledge that this has occurred by stating that, "*…because of the flexibility of the actuator piston, there was still a small amount of movement of the backwall at the soil-wall interface*."

Given the observations above, it is clear that further tests are required to quantify the sensitivity of the lateral capacity of a skew abutment with respect to transverse movements and rotations about the abutment's vertical axis. Due to the general eccentricity of a skew angled backfill's passive reaction to the center of stiffness of a bridge, the tendencies for such motions will directly increase with skew angle. Ultimately, such movements are inevitable in real bridges and as such, it is essential to develop passive abutment response models that take them into account. The model presented in this study considers only pure lateral movements. Although limited in scope, this simple predictive model can be used as a starting point to develop more complete models that take into account all three possible movements of the abutment (i.e., lateral movement, sidesway, and rotation).

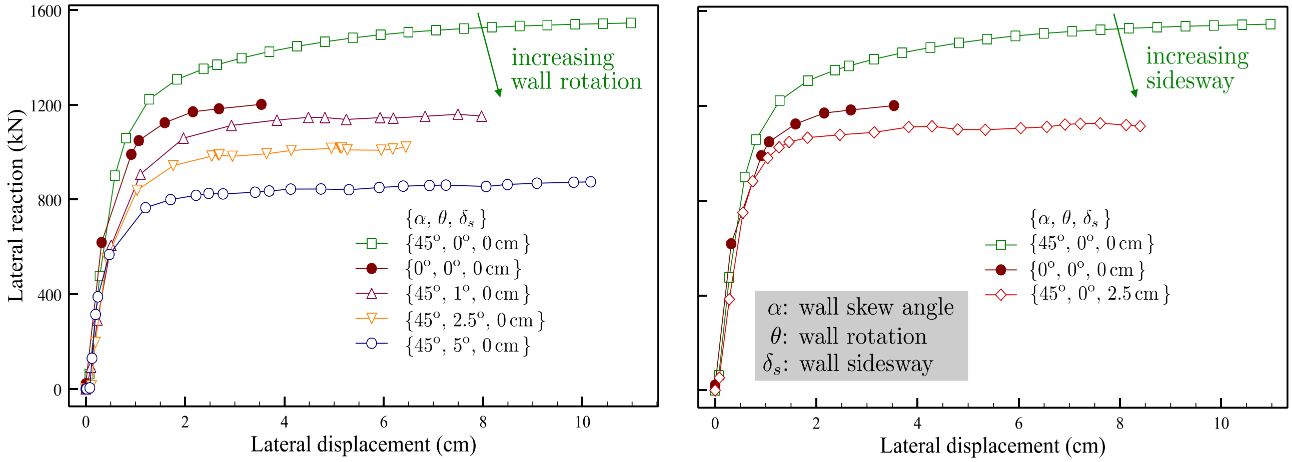

Fig. 4.8 Sensitivity of the response backbone curves to small rotations (left) and lateral sidesway (right) of the abutment.

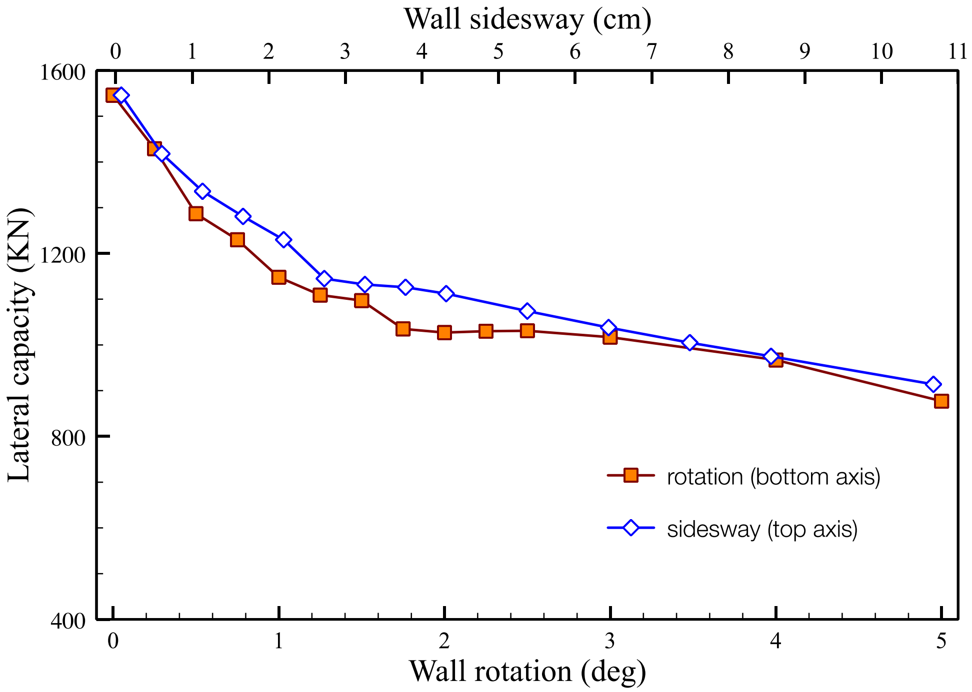

Fig. 4.9 The effects of slight wall sidesway and rotation on lateral capacity of a 45-degree skew abutment.

4.6 Some Remarks

This study provided a method to predict the lateral load-deformation behavior of seat-type skew bridge abutments under pure lateral displacements. This predictive model for skew abutments was based on two conjectures, which were put forth in the present study and tested for accuracy through numerical simulations with three-dimensional finite element models. These simulation models were identical to those that were validated against test data from a straight abutment given by Stewart *et al.* (2010), except for the abutment skew angle, which was gradually varied in systematic parameter studies. The results from these studies suggested the use of an optimal λ coefficient (with a recommended value of 0.6) with which the lateral load-displacement backbone curve of a straight abutment (as well as the lateral capacity) can be transformed into that of a skew-angled abutment given the skew angle (α). A previously verified and validated limit equilibrium method that uses physical parameters (such as the abutment backwall height, soil properties, etc.) supplies the lateral behavior of the corresponding straight abutment (Shamsabadi *et al.*, 2010; Khalili-Tehrani *et al.*, 2010).

A sensitivity study using 3D finite element model of 45-degree skew abutment indicated that the lateral reaction would reduce rapidly if the abutment rotates about its vertical axis or moves transversely (sidesway). Since these motions are inevitable, and will be exacerbated by increasing skew angles, it is essential to incorporate them into predictive models of skew-angled abutment responses. The simple model presented in this study considers only pure lateral movements. Although limited in scope, this predictive model can nonetheless be used as a starting point to develop a more complete model that takes all three possible movements of the abutment (i.e., lateral movement, sidesway, and rotation) into account.

Chapter 5

A Macroelement Model for Skew Abutments

5. A Macroelement Model for Skew Abutments

5.1 Methodology

The macroelement that will be developed herein is based on a resultant-base plasticity framework, and will provide a skew-angled abutment's passive reaction forces and moments under lateral and rotational motions. The vertical motions are not of interest, because the passive reactions are induced by bridge decks that are typically constrained against vertical rigid body movements. Also, additional features such as sub-elements to represent radiation damping, shear keys, and unseating-switches can easily be added to this present macroelement, but are out-of-scope in the present effort.

It is also expedient to note here the while PLAXIS had been sued in previous verification and validation studies, ABAQUS will be used in the development of the macroelement model here, because PLAXIS is not suitable for modeling contact conditions and prescribing displacement time-histories. On the other hand, ABAQUS does not feature an direct equivalent of the "Hardening Soil" model of PLAXIS (Schanz *et al.*, 1999), which was shown, in Chapter 3, to mimic passive backfill behavior very successfully." As such, the Modified Mohr-Coulomb model in ABAQUS was utilized and its *mobilized cohesion coefficient* was calibrated so that lateral load-deflection backbone curves obtained from ABAQUS and PLAXIS agreed.

The verified ABAQUS models are then used in parametric studies to probe the skew abutment behavior, and these results are interpreted and organized through the prism of the model obtained in Chapter 4 for a non-rotating backwall as well as other analytical considerations. During the process of loading in ABAQUS simulations, the deformation of the backfill is taken into account throughout the history of deformations, and the frictional contact as well as partial gapping between the backwall and the backfill is rigorously modeled. The backwall is assumed to be rigid.

5.2 Geometry and kinematics

Here, the geometric quantities that control the backwall kinematics are defined (see, Fig. 5.1). Deck width (*D*) the width of the bridge deck perpendicular to the traffic direction. Wall width (*W*) is defined as the total length of the abutment backwall. As such, $W = D\cos\alpha$ where α is the skew angle. The height of the backwall is denoted as *H*.

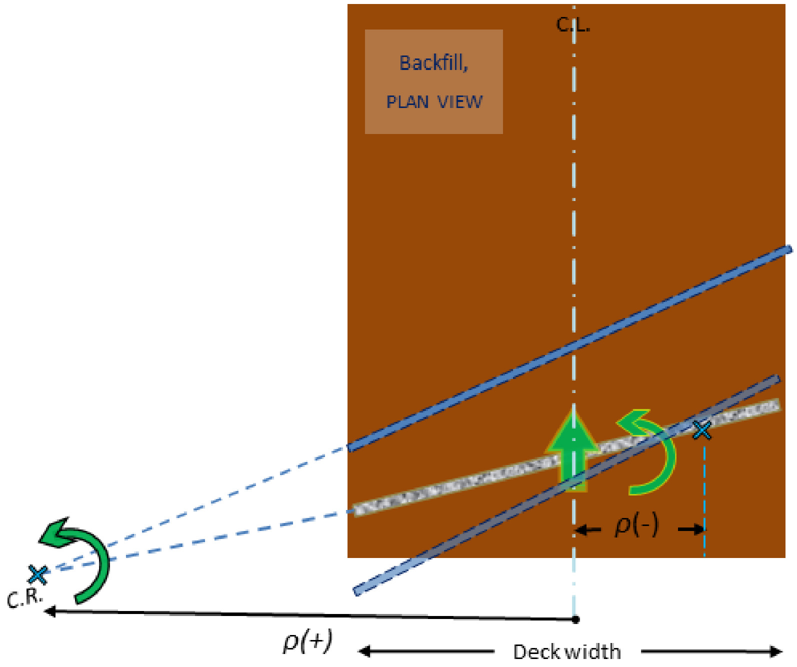

Fig. 5.1. Instantaneous center of rotation and radius ρ.

Taking into account only the lateral displacement and the vertical rotations of the wall, all the possible motions (kinematics) can be described by the displacement Δ, and rotation θ. Based on the incremental displacement and rotation, the Instantaneous Center of rotation (*IC*) can be determined with respect to which the entire motion of the wall can be described as a rotation only. It is important to note that IC is constantly changing throughout the loading history. The parameter ρ is introduced as the distance between the point of *IC* and the Center of wall *O*.

The sign convention we set for parameter ρ is defined through the expression $\overrightarrow{\theta_n^+} \times \overrightarrow{\Delta_n^+} = \overrightarrow{\rho_n^+}$ where θ_n is the *normalized rotation*. This implies, that the cross product from left-positive θ into positive Δ will yield the positive direction for ρ. Positive direction of θ is taken to be the rotation towards the acute corner of the wall, which is the rotation that increases the original skew angle. The positive direction for displacement is designated to be from the backwall towards the backfill.

It is important to mention that the axis of *IC*, which we parameterized here by ρ, is always perpendicular to the traffic direction, since we designate Δ to be the displacement along the traffic direction (Fig. 5.2). The determination of the traffic-direction reaction (F_x) will be the key value in determining the rest of the unknown reactions to the input displacement pair (displacement and rotation).

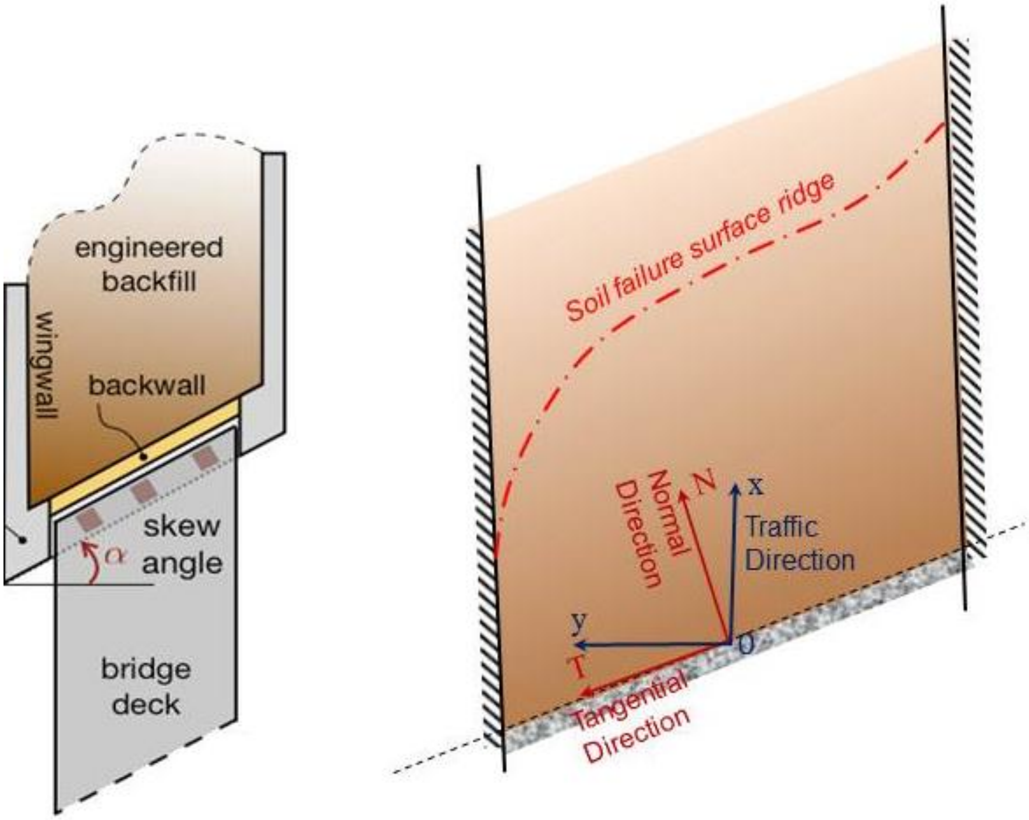

Fig. 5.2. **(**a) Typical seat type abutment (b) Traffic direction and the tangential coordinate system.

Given the aforementioned conventions, applying a positive displacement and positive rotation places the *IC* on the acute side of the wall from the wall center, hence produces a positive ρ. A positive displacement and negative rotation puts the *IC* on the obtuse side from the wall center, which means that

ρ is negative. A negative displacement combined with positive rotation causes a negative ρ, and placed the *IC* on the obtuse side. Finally, in case both negative displacement and rotation are imposed, the *IC* will lie on the acute side from the wall center, and ρ will be positive, which is given through the simple formula

$$\rho = \frac{\Delta}{\tan(\alpha+\theta) - \tan(\alpha)} \tag{5.1}$$

Eq. 4.1 describes ρ in terms of the traffic direction displacement of the backwall Δ, the skew angle α (which is the undeformed angle of the abutment), and the rotation angle θ.

5.4 Utilization of the straight non-rotating abutment model

The cornerstone of the skew abutment-backfill behavior model is the lateral reaction of its corresponding straight abutment (where the skew angle is zero). In our models, the results for the straight abutment will be obtained using the Generalized HFD (GHFD) model (Khalili-Tehrani *et al*., 2010). The GHFD model yields the backbone curve for the lateral passive reaction of a straight abutment backwall for any soil type and wall height. The no-rotation scenario obviously guarantees full contact between the backwall and backfill under monotonic lateral translations, as well as symmetry with respect to the centerline. Assuming that boundary effects (at wingwall locations) are negligible, the lateral reaction will be scalable by wall/deck-width, and thus lateral reaction per unit wall length will be a constant for a given wall height, skew angle, and backfill material.

Figure 5.3 displays results obtained from the LSH/GHFD method for a set of different soil types, for a 4.57m-wide (15 ft) and 1.67m-high (5.5 ft) wall. The soils considered in this figure range from cohesive to granular. In cohesive soils, the soil internal friction angle $\emptyset$ is low, and granular soils, the soil cohesion *c* is low. As described earlier in Chapter 3, the two typical backfills used in California abutments had been tested by groups at UC Davis (cohesive), and UCLA (granular) and capacity values measured in those tests are also shown in Fig. 5.3, for comparison.

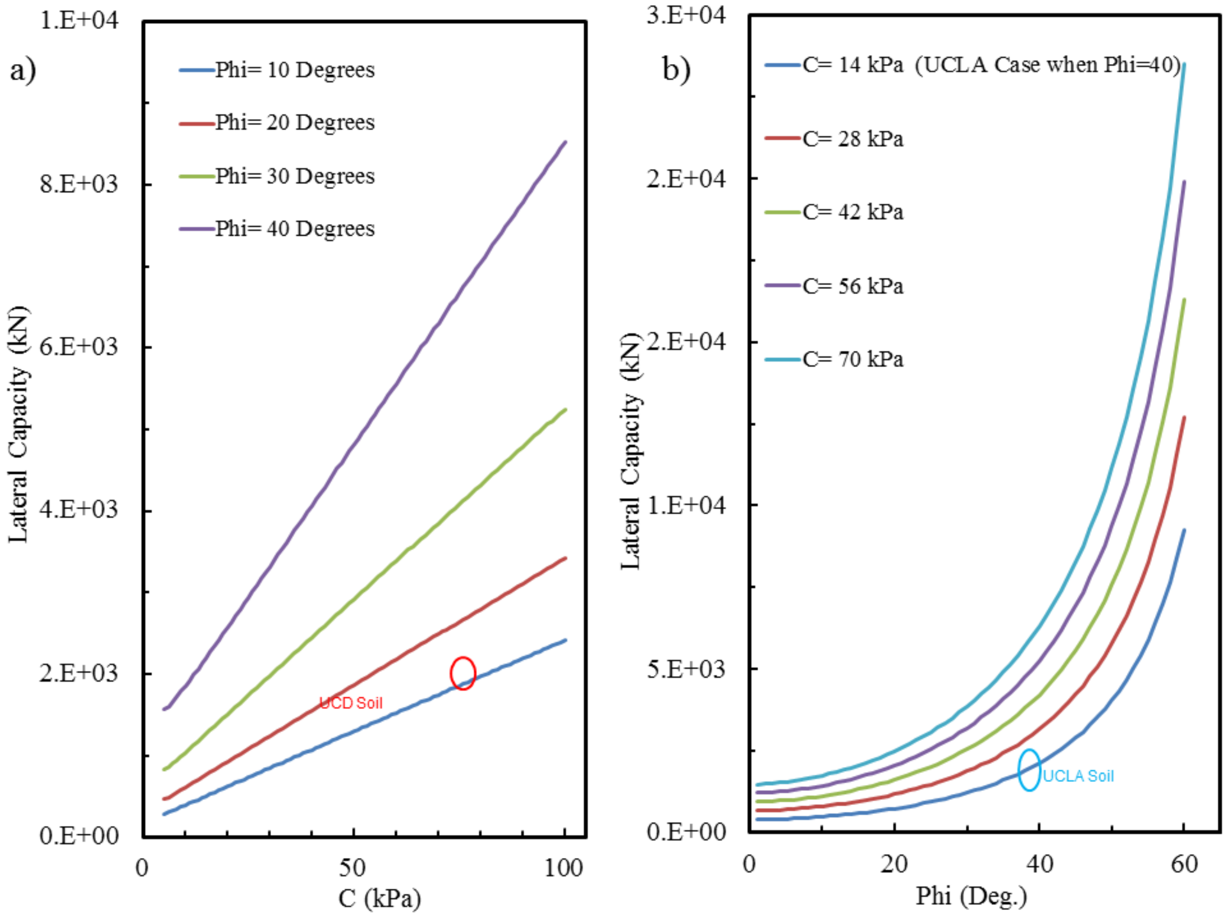

Fig. 5.3. Results from the GHFD model: effect of soil parameters on the backfill's ultimate reaction. (a) effect of cohesion for different internal soil friction angles (Phi) (b) vice versa.

The ability of the GHFD (thus, indirectly, of LSH) to rapidly yield lateral capacity values will be exploited here in devising the macroelement model. The GHFD model can easily be used to in combination with the correlation model (λ) described in Chapter 4 to extract the backbone curve (incidentally, the ultimate strength) of the backfill of any skew abutment, as long as there are no rotations. As it will be described below, the lateral reaction estimated thus from GHFD for a given skew angle will play a pivotal role in calculating the remaining elements of the unknown reaction set.

We begin that analysis by first defining lateral **c**apacity of the backfill normalized by the **a**rea of the **w**all for a given skew angle $\boldsymbol{\alpha}$ (henceforth referred to as CAW_{α}) as

$$CAW_{\alpha} = \frac{Capacity}{Area\ of\ the\ Wall} \tag{5.2}$$

In Eq. (5.2) "*Capacity*" denotes the ultimate capacity of the backfill in the traffic direction. We then define ratio of the **c**apacity of a skew wall with that of its nominal straight wall (i.e., Capacity-to-Nominal Ratio, or *CNR*).

$$CNR = \frac{CAW_{\alpha}}{CAW_{Nominal}} = \frac{Cap_{\alpha}}{Cap_{n}} \times \frac{A_{n}}{A_{\alpha}} \tag{5.3}$$

Here, the *nominal* wall corresponds to a straight wall that has the same deck-width as the skew wall (thus, the skew wall is the Upper-Bound wall to the nominal wall defined earlier in Chapter 4). Finally, we define the normalized skew angle as,

$$\nu = \frac{\alpha}{\pi/2} \tag{5.4}$$

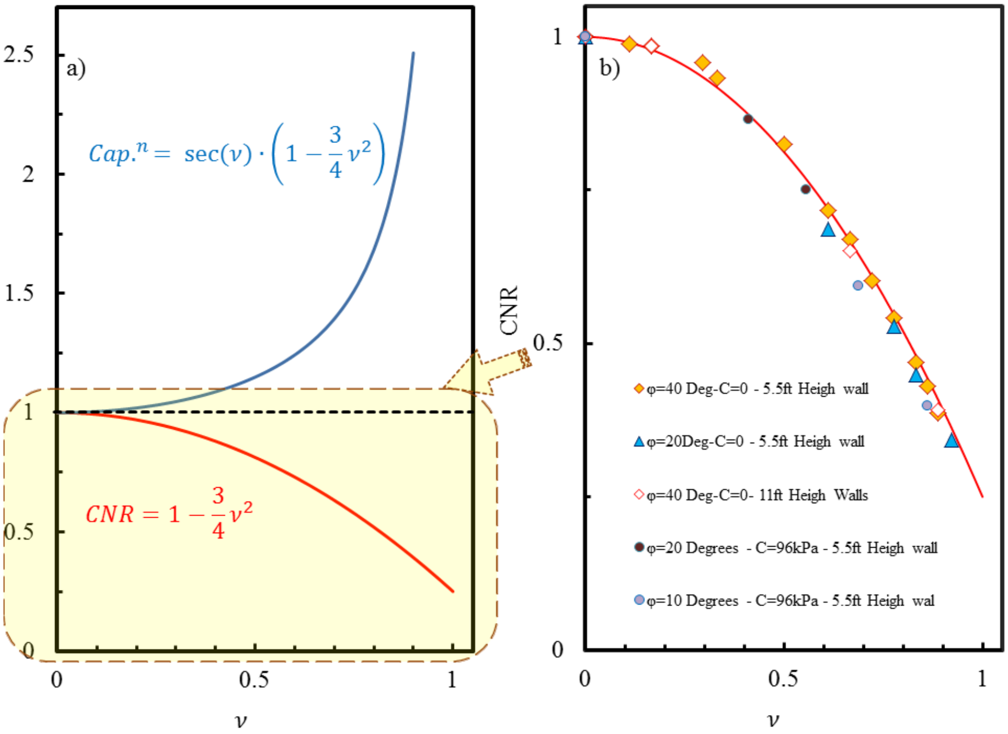

Fig. 5.4. CNR and normalized capacity versus the normalized skew angle (a), and CNR correlation with FE results for different geometries and soil types (b).

Fig 5.4(b) displays *CNR* values for a variety skew walls and for a broad range of backfill material types. These values are obtained through the use of the GHFD model as well as validated ABAQUS FEM simulations. It is interesting and fortuitous that the normalization scheme devised above yields such a regular trend in the *CNR*-versus-ν curves. To wit, the following simple formula

$$CNR = 1 - \frac{3}{4}\nu^2 \tag{5.5}$$

provides as excellent fit even up to normalized skew angles $\nu = 0.9$, as seen in Figure 5.4(b).

Note that in all these calculations, the backfill and the backwall are in full contact (no separation) and there is no rotation. The direction that *CNR* is calculated for is the lateral direction (*x*-direction), which is aligned with the traffic flow. Using Eq. (5.5) and *CNR* can be calculated for any skew angle. Then, the following identities can be used to determine the lateral capacity of a skew-angled backwall (Cap_α) as

$$Cap_\alpha = CNR \times \frac{A_\alpha \times Cap_n}{A_{nominal}} = CNR \times \frac{A_{nominal}/\cos(\nu)}{A_{nominal}} \cdot Cap_n$$

$$\rightarrow \qquad Cap_\alpha = CNR \times \sec(\nu) \times Cap_n \tag{5.6}$$

or equivalently,

$$\frac{Cap_\alpha}{Cap_n} = CNR \times \sec(\nu) = \sec(\nu)\left[1 - \frac{3}{4}\nu^2\right] \tag{5.7}$$

The ratio given in Eq. (5.7) is also plotted in Fig. 5.4(a). Thus, if the capacity of the nominal (straight) backwall (i.e., Cap_n) is known—which can be easily obtained using the GHFD formulae—then the lateral capacity of its non-rotating upper bound skew wall can be determined using Eq. (5.6).

5.5 Reactions for rotating skew abutments

In the discussion above, the response of a skew non-rotating bridge abutment is characterized. Introducing the backwall rotation will produce a more complicated scenario. As depicted earlier in Figure 5.2, for any general abutment wall there will be three reaction components—namely, the two in-plane perpendicular force reactions, and the out-of-plane moment reaction.

The backfill reaction calculations will begin by determining the correlation between the normal component of the abutment reaction (N) and the tangential component (T), using a parameter henceforth referred to as the *average mobilized friction coefficient* (μ_{avg}). This coefficient will be extracted from FE simulations. Once this relationship is established, it will be possible to refer to the lateral direction capacity (F_x), which can be computed using Eq. 5.6 for the no-rotation case, as well as the tangential reaction (F_y) through a simple coordinate transformation. FE simulations will also inform the pressure distribution pattern on the wall, including contact/gapping conditions, from which the moment reaction can be computed.

5.5.1 Elements of the rotating wall reactions

We begin by first transforming an unknown F_x and unknown F_y into N and T using the skew angle. Working in the backwall coordinate system that allows the utilization of the backwall-backfill frictional behavior as an auxiliary relationship. This auxiliary equation, as will be described in detail in the next section, will allow the correlation of the mobilized friction coefficient (μ_{avg}), the instantaneous radius of rotation (ρ), and the skew angle (α).

We define μ_{avg} to be the simply ratio of the tangential to the normal components of the backfill reaction, as in

$$\mu_{avg} = \frac{T}{N} \tag{5.8}$$

This coefficient is obviously a function of geometry and the loading kinematics (because of varying contact area). Since the mechanical friction coefficient between any backwall (most probably a concrete surface) and the backfill soil is a physical property that can be measured (e.g., by laboratory tests), then it is reasonable to normalize the average mobilized friction coefficient of surface reactions by that measurable constant maximum friction ratio, μ_{max}, to define

$$\mu^n = \frac{\mu_{avg}}{\mu_{max}} \tag{5.9}$$

Likewise, we can also define a normalized instantaneous center of rotation ρ^n using the kinematics we had defined above, as

$$\rho^n = \frac{\rho}{D} = \frac{\Delta/D}{tan(\alpha+\theta)-tan(\alpha)}\,. \tag{5.10}$$

Any correlation for normalized friction coefficient would be a function of skew angle (α) and the normalized instantaneous center of rotation ρ^n. We have the following bounds for these quantities:

$$\alpha \in \left[0, \frac{\pi}{2}\right[\quad \text{and} \quad \nu = \frac{\alpha}{\pi/_2} \;\rightarrow \nu \in [0, +1[\tag{5.12}$$

$$\rho \in \left[-\frac{D}{2}, +\infty\right] \;\rightarrow\; \rho^n \in \left[-\frac{1}{2}, +\infty\right] \tag{5.13}$$

Using these bounds as the feasible range of parameter space for the problem at hand, a series of FE simulations are carried out for a broad range of α and ρ^n values. Results of these simulations are shown in Figure 5.5. These results can be used to obtain the following simple formula for the normalized mobilized friction coefficient as a function of skew angle and instantaneous normalized radius:

$$\mu^n_{(\alpha,\rho^n)} = -\text{sign}(\rho^n) \times \tanh\left((2\nu)^2 \cdot |\rho^n|^{\frac{1}{2}}\right) + \frac{1}{5}\sin(\pi\nu) \tag{5.14}$$

Although the algebraic range for μ^n would span from $-\frac{4}{5}$ to $+1\frac{1}{5}$, since physically the average mobilized friction coefficient cannot surpass μ_{max} and ρ^n cannot physically attain values below-0.5, the feasible range for μ^n is

$$\mu^n \in \left[-\frac{4}{5}, +1\right]. \tag{5.15}$$

Thus, the expanded correlation relationship for the mobilized friction coefficient can be expressed as

$$\mu_{avg} = \mu_{max}\left\{-\mathrm{sign}\left(\frac{\Delta}{\tan(\alpha+\theta)-\tan(\alpha)}\right) \times \tanh\left(\frac{16\cdot\alpha^2}{\pi^2}\cdot\left|\frac{\Delta}{D[\tan(\alpha+\theta)-\tan(\alpha)]}\right|^{\frac{1}{2}}\right) + \frac{1}{5}\sin(2\alpha)\right\} \tag{5.16}$$

Although the mobilized friction coefficient results are theoretically asymmetric for pro- and counter-skew rotation scenarios, this variation is seen to be marginal in all FE simulations, and thus Eq. (5.16) offers a unique formula for both pro- and counter-skew motions of the wall.

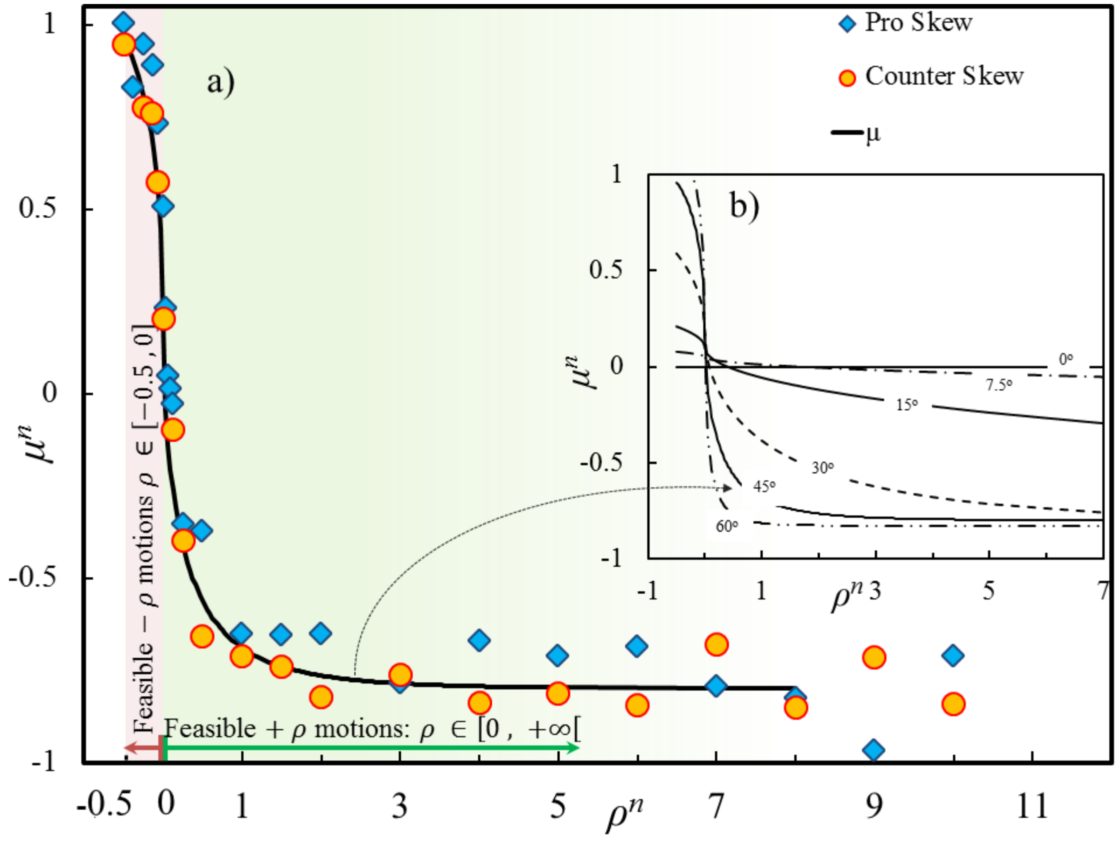

Fig. 5.5. The Normalized Average Mobilized Friction (μ^n) versus the normalized instantaneous radius (ρ^n) for a 60-degree to 0-degree skew backwalls (FE data for 45-degree wall is shown in detail).

Based on the coordinates described earlier, the relationships between the Fx and Fy, and T and N is simply

$$N = F_x \cos\alpha + F_y \sin\alpha, \tag{5.17}$$

$$T = F_y \cos\alpha - F_x \sin\alpha. \tag{5.18}$$

Since the following is true at all loading conditions,

$$T = N\,\mu_{avg} \tag{5.19}$$

Thus, Eqs. (5.17) through (5.19), together with (5.16), form a constitutive relationship that links the wall kinematics (Δ, θ) to the wall reactions (T, N). We also have

$$N_\alpha^{max} = \frac{F_x^{max}}{\cos\alpha - \mu_{avg}\sin\alpha}. \tag{5.20}$$

and note here that F_x^{max} can be directly computed using Eq. 5.6 for the no-rotation case.

5.5.2 The moment reaction

Having the normal effective force in hand, we finally arrive at the determination of the moment reaction, M_z, which we define, without loosing generality, with respect to the center of the wall. The reason for this choice is to avoid potential complications that may be encountered if we take either the acute or the obtuse-end of the wall as the reference point of the moment reaction.

By integrating the lateral incremental reactions of the backfill along the wall, we can calculate the moment reaction. The macroelement should take into account the effective area of contact between the backwall and backfill, which, at every time increment, can be calculated simply by updating the deformed shape of the backfill and by taking into account the displaced position of the backwall. While the said calculation (integration) is simple, we do not yet know the variation of the normal pressure along the length of the wall within the contacting areas. Determination of the said pressure will require utilization of FE simulation results, as well as adoption of a simplifying assumption.

One major difference between a straight abutment and a skew one is the simple fact that due to symmetry, the stress distribution along the face of a straight wall is uniform. Hence it can be deduced that a unit area of soil provides the same stiffness and strength for a straight wall. This is not true for skew backwalls, and as it will be presented later, the unevenness in the strength of different portions of the backfill increases with increasing skew angle.

The said trend was explored here to determine how different portions of the backfill react to the backwall's motions. The pressure at the bottom edge of every wall was chosen as a representative location for the mobilized pressure acting on the backwall. The bottom edge of the wall is more important than other locations on the wall because the ultimate failure surface originates from this location (see, for example, Stewart *et al*., 2007).

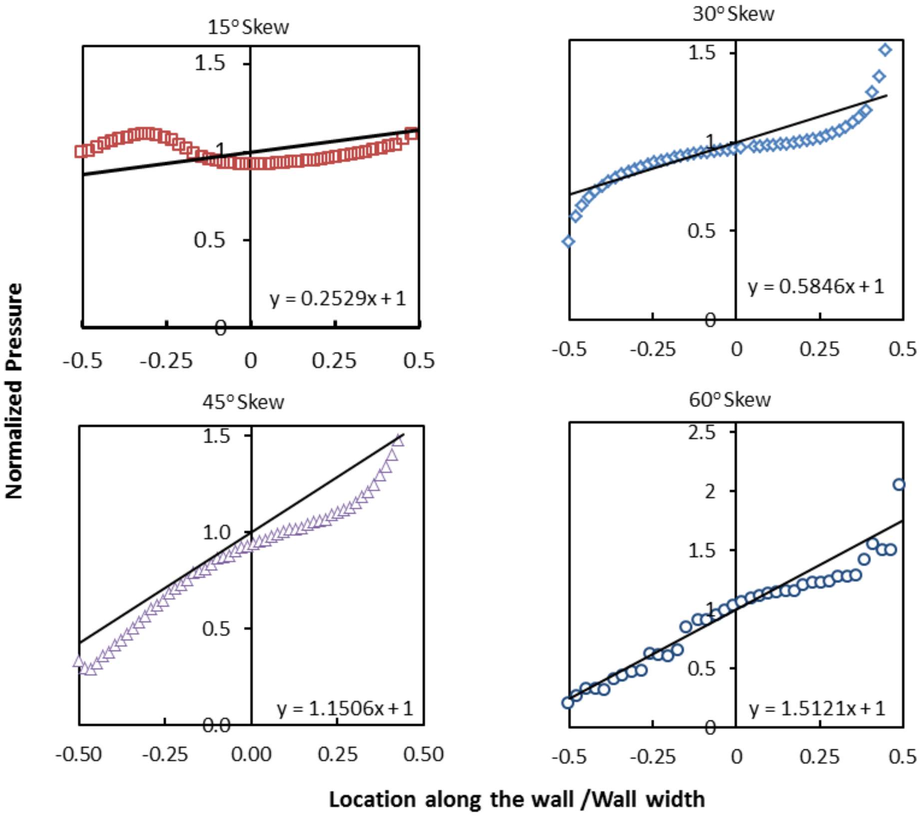

Fig. 5.6. Distribution of the normalized pressure over the normalized width of the wall.

Figure 5.6 displays how for four different increasing skew angle cases the pressure at the bottom edge of the backwall becomes more uneven and increase towards the obtuse-end of the backfill. For all the four cases, the horizontal axis is the distance from the center of the wall normalized by the wall width, and the vertical axis is the pressure values at different sampling points at the bottom edge normalized by the average pressure.

The results from this part of the study were used to devise a relationship that helps modeling the out-of-plane moment reaction in an approximate, albeit realistic manner. The pressure distribution for each studied FE simulation case was represent with the generic function, x_D^{nor} is the distance of every point from the center, normalized by the wall width,

$$p_{(x)}^{nor} = m_\alpha \cdot x_D^{nor} + 1 \tag{5.21}$$

where p^{nor} is the normalized pressure at every point of the bottom edge divided by the average pressure of the same edge, given by

$$p_{(x)}^{nor} = p_{(x)}/p_{avg} \tag{5.23}$$

x_D^{nor} is the distance of every point from the center, normalized by the wall width, given by

$$x_W^{nor} = {}^{x_W}\!/_{D}, \tag{5.22}$$

and m_α is the slope of the fit for every skew angle α. From these basic definitions we have the following identity,

$$\int_{-D/2}^{D/2} p_{(x)}^{nor}\, dx_D^{nor} = 1. \tag{5.25}$$

Figure 5.7 displays the relationship that is used to model the rate of increase for the backfill's strength for different skew angles. Every rate of increase in Fig. 5.7 (*m*, on vertical axis) is basically the slope in the associated part of Fig 5.6. In Fig. 5.6, the wall center is set as the origin of the *x*-axis. In order to reduce the number of unknowns in determining the pattern of pressure against the wall, it was assumed that the correlated pressure meets the average pressure observed in FE simulations, and that its distribution is linear along the wall width. Obviously, these assumptions are made to simplify the problem and more detailed study could be carried out to determine the actual distribution of pressure. Such a study would also allow the observation of the disturbing effects of the boundary elements (wingwalls) on the pressure distribution. That said, these additional studies are omitted here for the sake of keeping the model simple; and as it will be seen later, and adequate accuracy will be attained with the current simplifying assumptions in place.

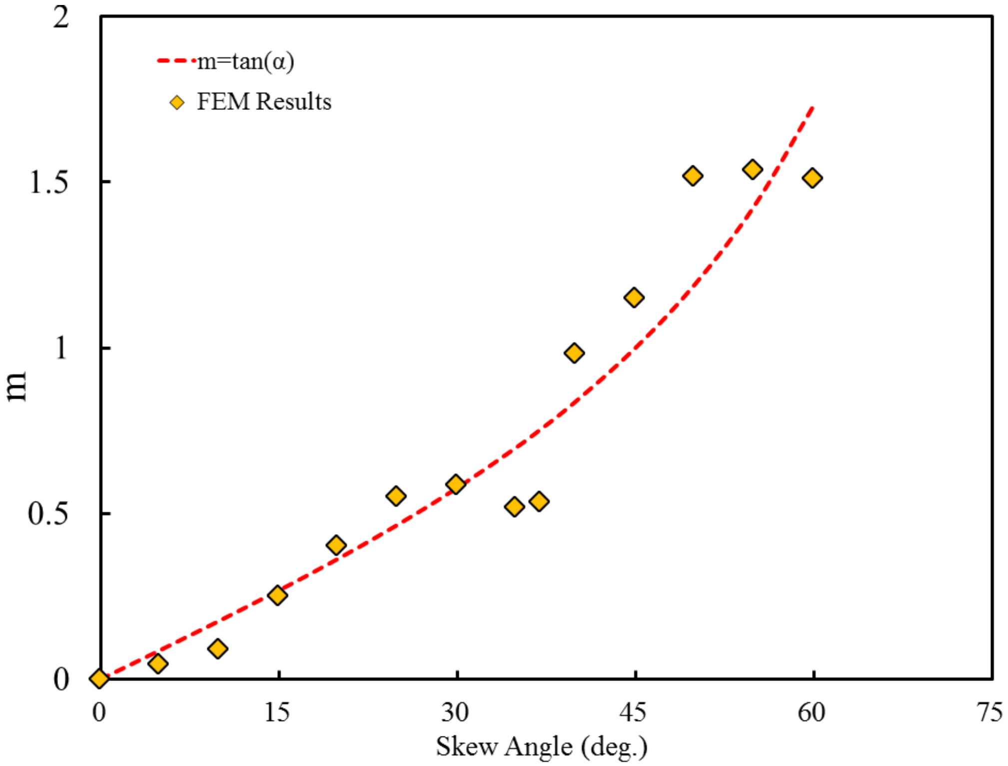

Fig. 5.7. Change rate of the pressure in FE model, and the regression-based model used for the macroelement.

The approach chosen from this point on is to use the pressure distribution obtained for the bottom edge of the wall to determine the normal force per length of the wall. That is,

$$n_{(x)} = N_{\alpha}^{max} \cdot p_{(x)}^{nor} \tag{5.26}$$

5.5.4 The effective versus full contact area

In order for the model to reproduce the reactions correctly, it should adaptively take into account the deformed shape of the backfill and the updated geometry of the wall. An adaptively changing contact area is needed between the wall and the surface of the (deformed) backfill soil. For the present model, we will keep track of the *effective contact area*.

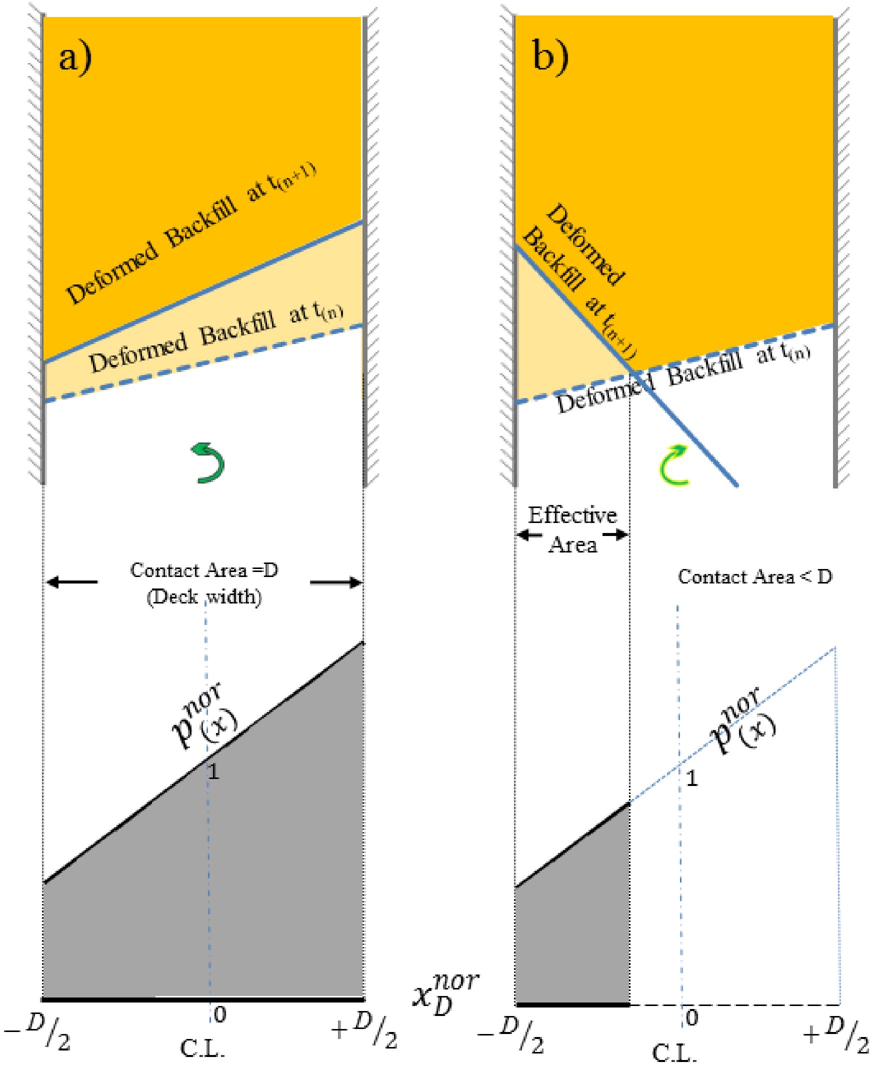

Fig. 5.8. Full area of the wall in contact with the backfill (a), versus reduced (effective) contact area (b).

When the length of in-contact segment is less than the deck-width, the longitudinal reaction (F_x) will not reach its maximum possible value (i.e., the backfill capacity will not be fully mobilized). Based on the distribution determined earlier for the normal stress on the face of the wall, the out-of-plane moment reaction can be calculated as follows,

$$M_z = \int_{A^{contact}} n_{(x)} x^{nor} dx = \int_{A^{contact}} N_\alpha^{max} p_{(x)}^{nor} x^{nor} dx \tag{5.27}$$

where N_α^{max} is the normal maximum reaction of the wall for a skew model. Both the ultimate capacity and the stiffness of soil in this model are assumed to vary by following same distribution function. This way, both the ultimate capacity and the stiffness of the soil, per length of the wall, will follow the same pattern of increase towards the obtuse end of the backfill.

5.5.5 Description of the overall model for macroelement

With the relationships at hand, it is now possible to devise an incremental displacement-driven procedure that produces the entire set of macroelement reactions, given the wall translations and rotation.

The entire process begins by acquiring the backfill soil's mechanical parameters and backwall's geometry. Based on those data and using the previously developed and validated methods such as GHFD (Khalili-Tehrani *et al*., 2010) or the LSH method (Shamsabadi *et al*., 2013) the maximum lateral reaction of the nominal wall (the counterpart straight wall to the given backwall with the same deck-width) can be calculated. Using this information, and the *CNR* relationship derived above (Eqs. 5.5 and 5.7) can be used to compute the lateral ultimate reaction of the skew wall, F_α^{max}.

With the ultimate normal capacity of the skew backfill calculated, the load combination parameter, ρ, and the previously calculated deformed shape of the backfill can now be used to determine the effective area of contact between the backwall and backfill at every time increment. A full knowledge of the loading scenario is needed to find the total mobilized friction coefficient between the backfill and the wall, μ. Using Eq. 5.20, the ultimate normal to the wall component of the backfill's reaction, N_α^{max}, can then be calculated.

In order to determine the moment reaction, the distribution of the resultant normal reaction along the wall has to be determined; which can be computed by using Eq. 5.21, which relates the skew angle, the slope of the distribution of the stiffness, and the strength normal to the face of wall as a function of position on the backwall, $p_{(x)}^{nor}$.

Based on this, the calculation of the normal stress distribution, $n_{(x)}$, can take place. After determining $n_{(x)}$, the out-of-plane normal moment, M_z, can be calculated through 5.27. This calculation would then yield the full set of resultants needed to complete one increment of loading. A flowchart for the calculations described above is shown in Fig. 5.9.

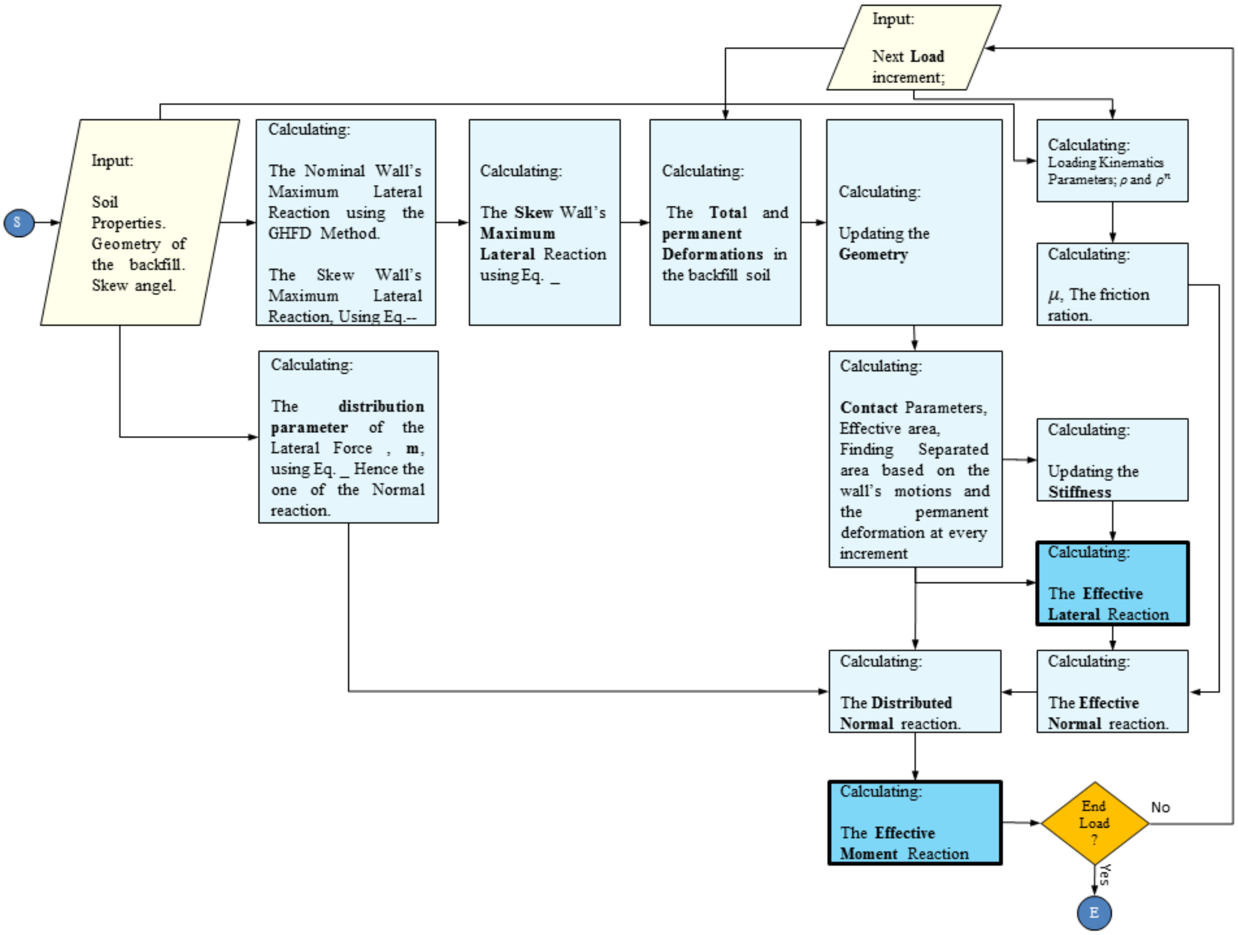

Fig. 5.9. Flowchart describing the proposed macroelement model.

5.6 Verification and validation of the macroelement model

5.6.1 Comparisons against test data and other validated models for straight walls

In order to evaluate validity the proposed macroelement model, UCLA full-scale backfill test (Shamsabadi *et al.*, 2010) results used. This is, of course, a partial validation, which tests the macroelement only for the no-rotation case, because the UCLA test was performed to mimic the behavior of a narrow straight abutment and no rotation was applied or permitted in the process of loading and unloading of the backfill. Present lack of data in this area postpones a complete validation in this regard.

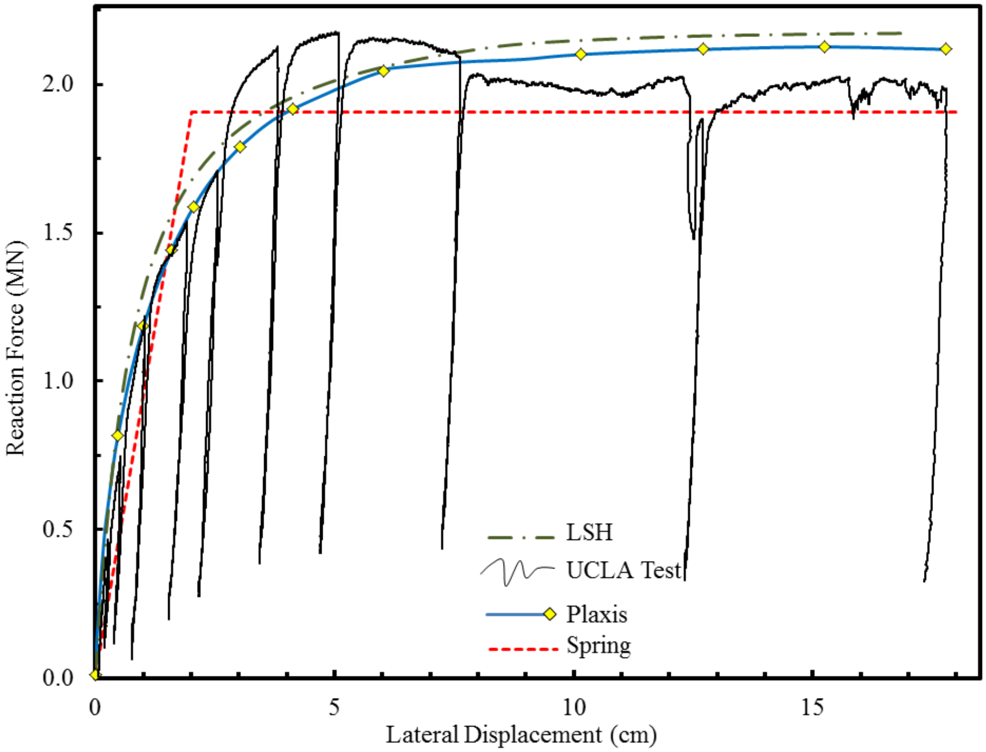

Fig. 5.10. Results for straight abutments; UCLA 15ft (4.57 m) wall full-scale test: results obtained with LSH, 3D FEM (Plaxis 3d foundation), and the macroelement model.

Figure 5.10 displays the measured data from the UCLA full-scale abutment test and predictions by different models. The other two simulations in this figure had also been shown earlier in Chapter 3, which were obtained using the Log-Spiral Hyperbolic (LSH) method (Shamsabadi *et al.*, 2010) and a three-dimensional finite element model developed and analyzed with PLAXIS 3D FOUNDATION (v.2.1) software. The Hardening Soil properties used in the Plaxis model as well as the properties of the soil used for LSH model were described in Table 3.1, previously.

As these results indicate, the macroelement model offers adequate accuracy. Naturally, the macroelement model exhibits an elastic-perfectly plastic behavior, whereas the other two numerical simulations show a gradual decrease in the tangent stiffness of the lateral reaction. Again, this comparison serves as a partial validation of the proposed macroelement model (one that is limited to non-rotating walls).

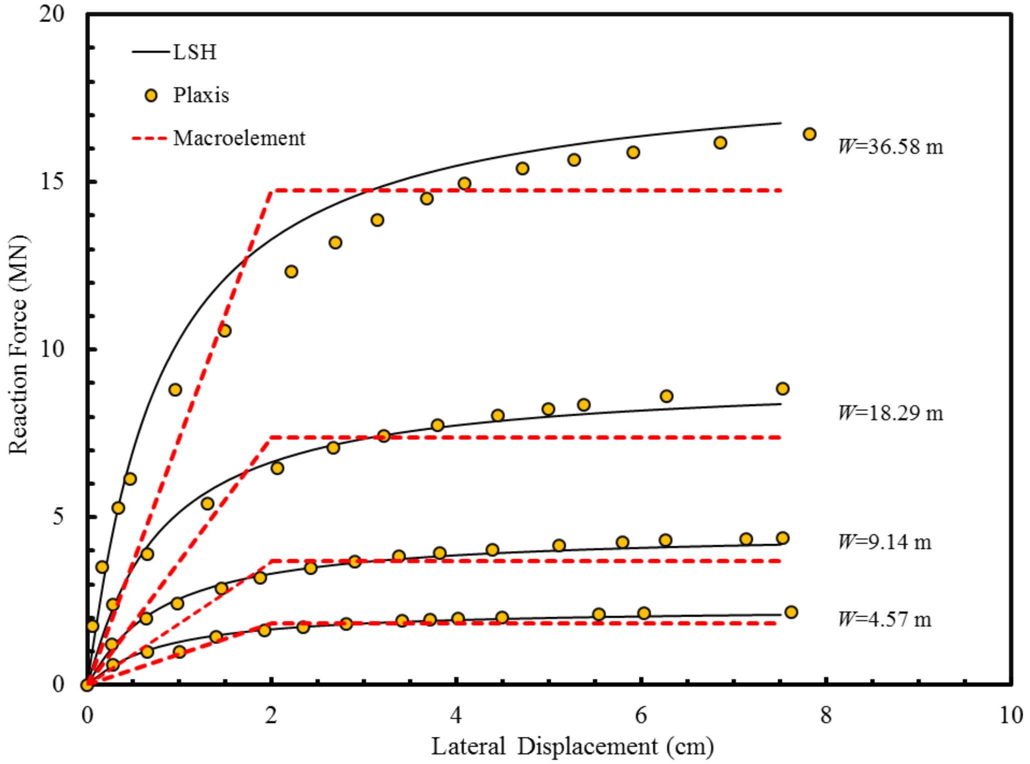

Fig. 5.11. Straight abutments with 1.65m height and various lengths: LSH, FEM, and macroelement results.

The macroelement model is also evaluated for a set of backwalls with 1.65m height and different deck widths varying from 4.5m to 36.5m, having the backfill of UCLA soil (properties previously presented in Table 3.1). These results are compared with those obtained using PLAXIS 3D FOUNDATION as well as LSH in 5.11, and good agreement is observed. Again, the constitutive behavior of the macroelement is elastic-perfectly plastic, and the backfill is pushed uniformly (plane-strain) in all wall models. This explains why all macroelement models for different walls widths fail at the same deflection. The failure deflection is 2 cm for all macroelement models for all skew angles. In this study, the potential variation of the failure deflection with wall width is not considered, however results from FEM analyses and the developed macroelement, suggest that studies on the variation of the failure deflection Δ^f could be considered in the future to further improve the model. Apart from this issue, the results obtained by the macroelement model as very good and provides a *verification* that the model can automatically take into account the wall height.

5.6.1 Model verification under cyclic loading for a straight abutment

All of the comparisons above involved the use of PLAXIS. For the subsequent comparisons, the results obtained from the macroelement model will be compared against FE models constructed and analyzed using the ABAQUS (v.6.11). This switch is made, because ABAQUS allows cyclic and displacement-controlled loadings, and has robust models of frictional contact between the backwall and the backfill, which are features that were lacking in PLAXIS at the time of the presentation of this document.

The macroelement model results under the cyclic loading scenarios are compared to ABAQUS FE models with approximately 600K degrees-of-freedom. All the models and the designed problems in this sub0section are for non-skew backwalls. The goal here is to see first how much the complication of the loading scenario can affect the results, especially to see if for higher number of load cycles, the error in the macroelement model results relative to FE model results blows up or not. Results show that not only for larger deformations of the backfill the error remains bounded, but also they remain highly accurate.

The first comparison involves the UCLA test configuration again. This involves a straight abutment with 5.5ft height (1.65m), and 30ft length (9.1m), displacing a cohesionless backfill with properties described previously. Various loading scenarios are considered, as described below:

A pure lateral push test

An increasing amplitude cyclic push/pull-only load pattern was applied to compare macroelement and ABAQUS results, which are shown in Figure 5.12. Again since the loading is push/pull-only, the response of the macroelement is elastic-perfectly plastic. The discrepancy between the two models is larger in small deformations, especially when the macroelement model is still in its elastic regime. Also because the backwall is straight, symmetric with respect to centerline, there is no out of plane moment mobilized in the FE model, and this also is taken care of, since the distribution parameter m in the macroelement model is zero ($\mathrm{m} = \tan\alpha$) for a non-skew model.

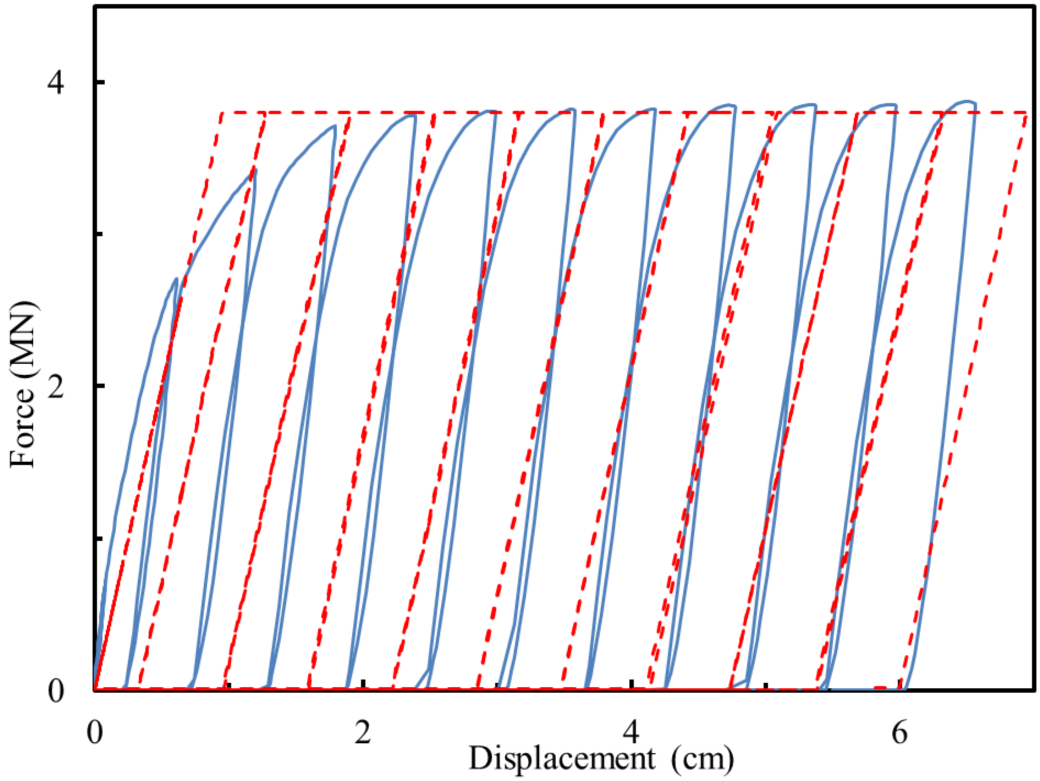

Fig. 5.12. Push-only test ($\rho = \infty$).

A pure rotation rest

In order to test the behavior of the macroelement moel in the rotation only load cases, a cyclic-rotation-only loading scenario was devised. The loading is symmetric in positive and negative directions, and is applied around the center of the wall. Results are shown in Fig. 5.13. Obviously, a pure rotation in the wall will cause moment and lateral force reactions simultaneously. Again, the FE and macroelement results are in very good agreement.

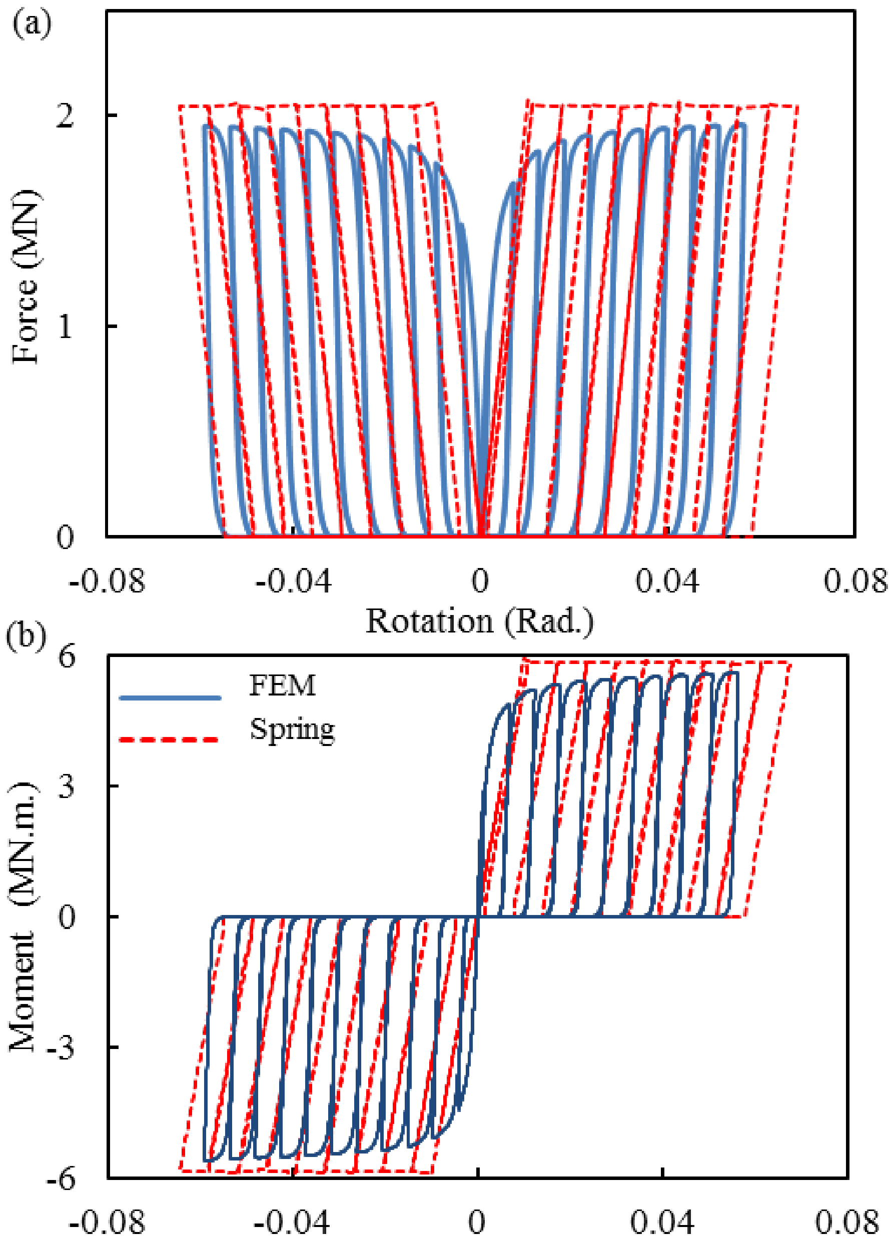

Fig. 5.13. Pure rotation test ($\rho = 0$).

A combined cyclic loading test

To further study the performance of the proposed model, a combined harmonic displacement and rotation scenario is devised. Figure 5.14 shows the force versus displacement, moment versus rotation, and force-moment diagrams for both the FE and the macroelement model simulations. The applied displacement was made sure to maintain positive values, but the cyclic rotation was symmetric with respect to wall center. Again one can observe that the discrepancy in small deformations is more significant, but the overall agreement is very good.

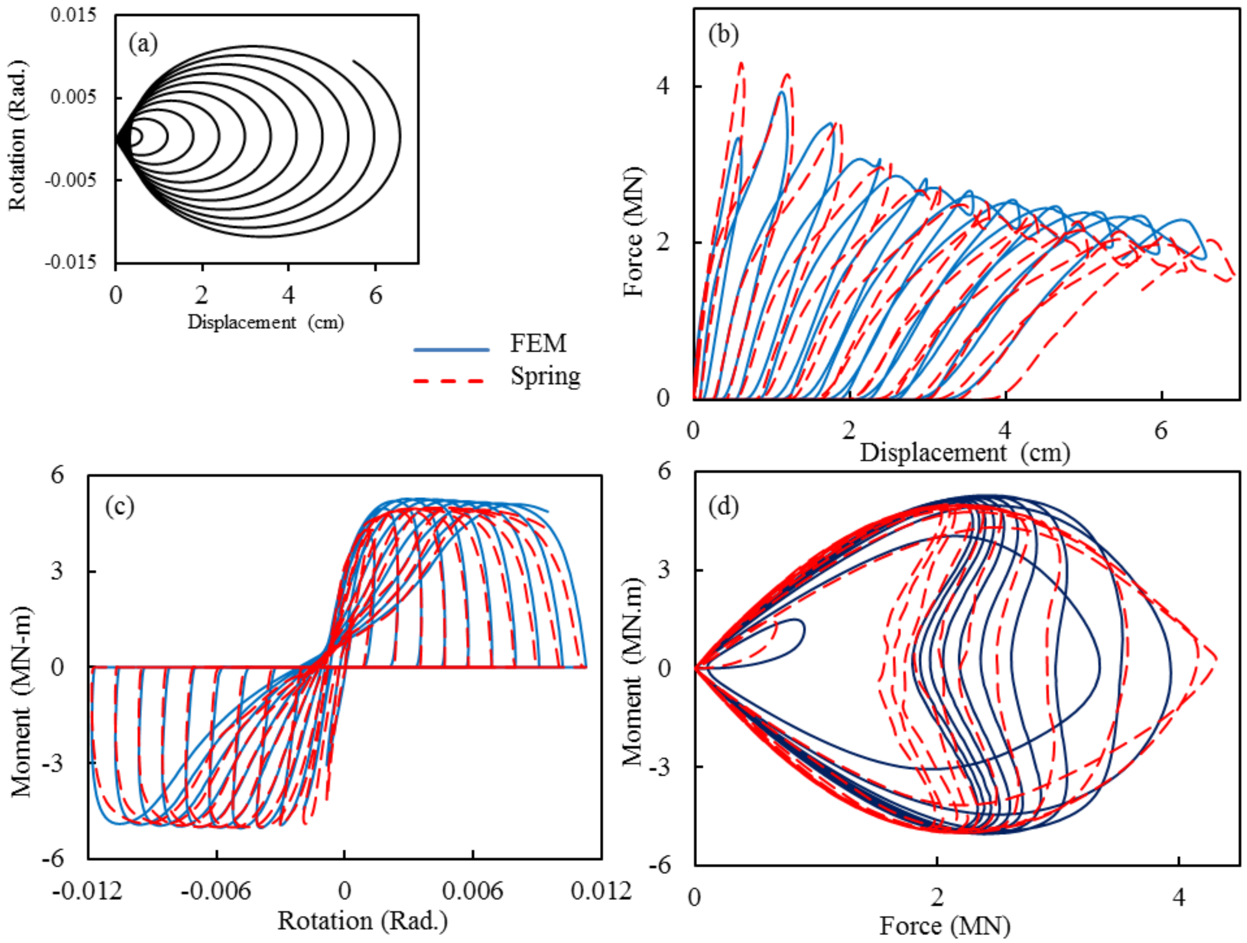

Fig. 5.14. Straight wall cyclic load combination.

5.6.2. Model verification under cyclic loading for a skew abutment

Here, results are presented from the analysis of the 45-degree skew abutment backwall of a 1.65m-high and 9.1m-wide deck.

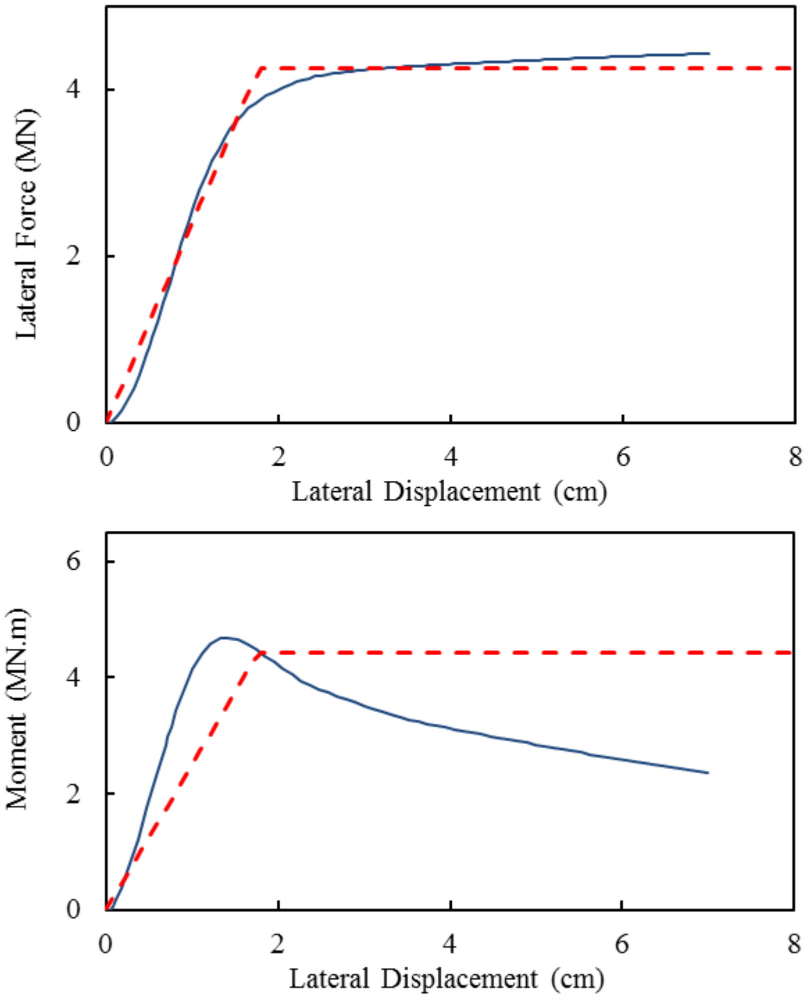

Fig. 5.15. Force and Moment reactions of a 45-degree skew wall under a monotonic-push-only load.

Pure push and rotation tests

A push-only monotonic analysis was performed to examine the behavioral differences in the macroelement and FE models. As opposed to the straight abutment case, a pure push can cause a moment reaction in abutments with nonzero skew angles. Figure 5.15 displays the results from the two models. Pure rotation analyses were also performed using the both FE and macroelement models. Figure 5.16 shows the results. Since the abutment is skew, neither the lateral force nor the moment reactions are symmetric with respect to the wall center. The results for both pure-push and pure-rotation cases indicate that the macroelement model provides very good accuracy. It is noted that the macroelement model does not exhibit the moment-softening response in the pure push case. While such a shortcoming can be fixed by introducing additional features into the macroelement model, such an extension is not warranted because the moment in a pure push case is a secondary effect compared to the lateral and transverse reactions, and can typically be neglected all together.

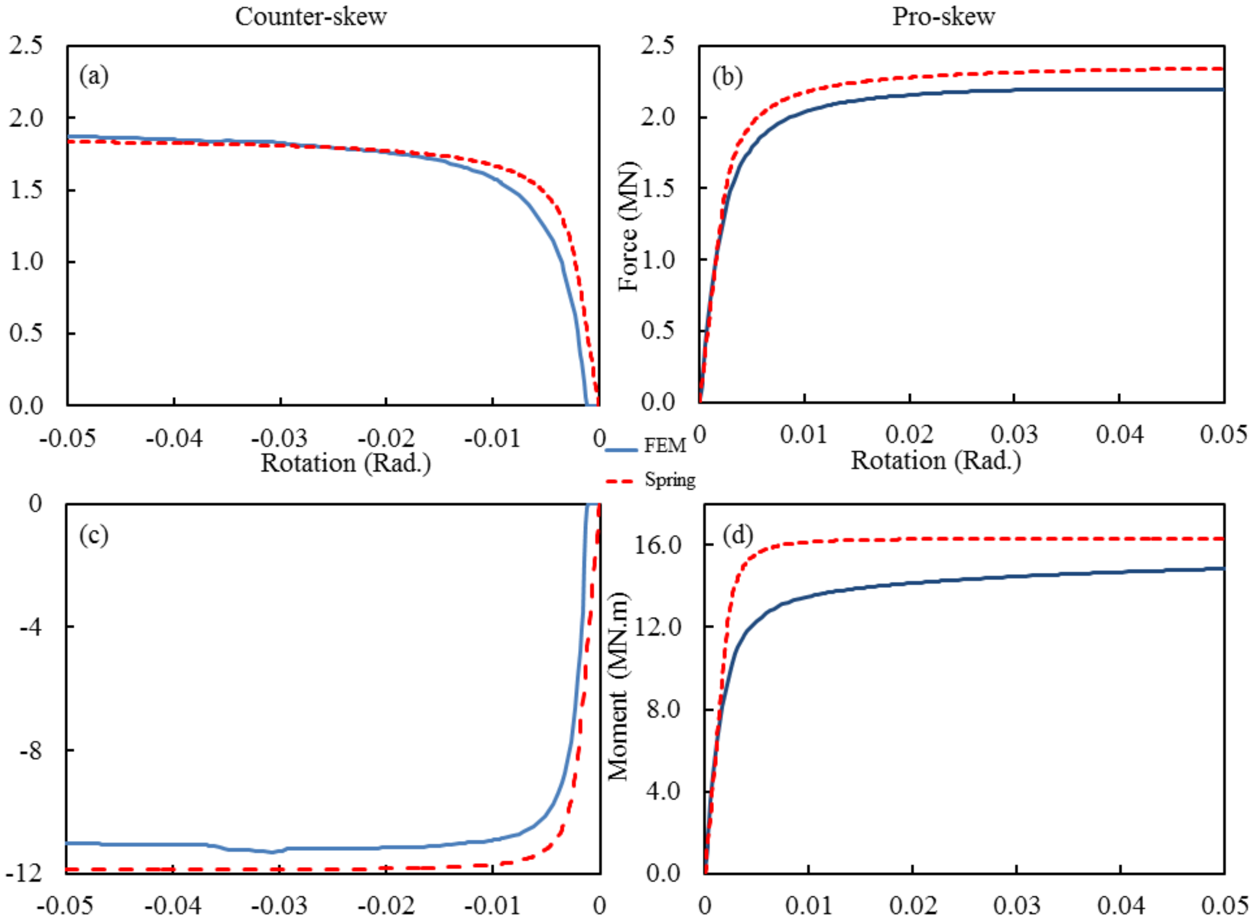

Fig. 5.16. Force and Moment reactions of a 45-degree skew wall under a monotonic-rotation-only load.

Combined cyclic loading test

A combined harmonic displacement and rotation scenario was also applied to a 45-degree skew abutment model. Figure 5.16 shows the force-displacement, moment-rotation, and force-moment diagrams for both the FE and the macroelement models. Displacements applied were kept within the positive range of motion, but the cyclic rotation was symmetric with respect to the wall-center. Results indicate that while there is some discrepancy in small deformations, the overall agreement between the two models is very good for the broad range of motions considered.

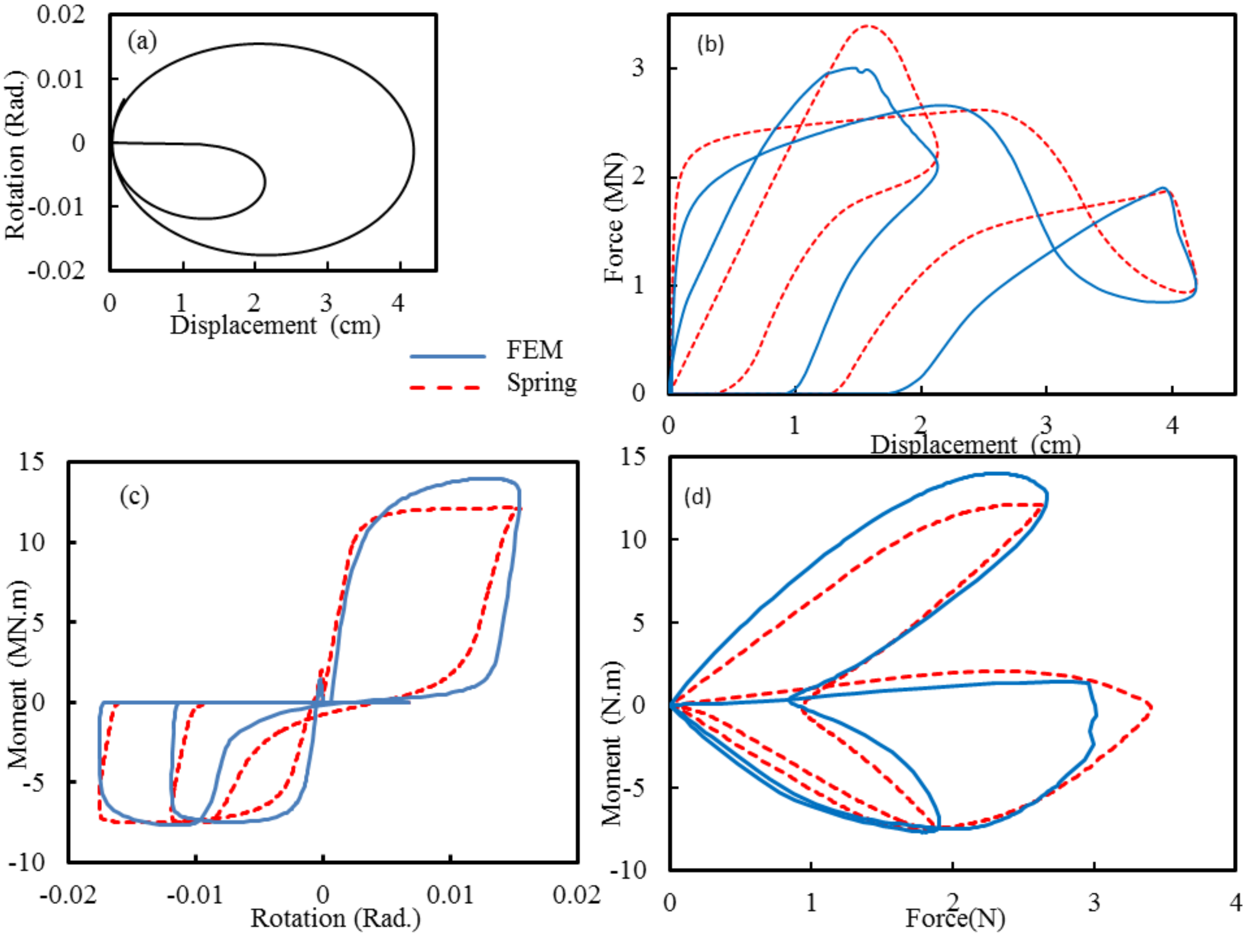

Fig. 5.17. Force and moment reactions of a 45-degree skew wall under a cyclic displacement and rotation combination load; (a) loading scenario (b) lateral reaction versus displacement, (c) moment reaction versus rotation (d) moment versus force.

Quasi-seismic motion test

In order to further study the behavior of a skew abutment, both degrees-of-freedom (DOF) were subjected to earthquake-like motions. The displacement diagram chosen to be applied onto the lateral displacement DOF was the El Centro EW (El Centro 270N), and in order to apply rotation, the displacement of the El

Centro NS (El Centro 180N) was applied to a hypothetical 3.50m-distant point from the wall center. This created the out-of-plane rotation applied to the wall center (Fig. 5.17). Since the load scenarios in two degrees of freedom were independent, the analysis mimicked a random rotation and displacement set of input that could be acting on a actual bridge during a real earthquake. Figure 5.18 displays the results from the FE and macroelement model simulations. Again, the agreement is very good. It is expedient to note here that while the FE simulations take more than a day on a desktop computer, the macroelement computations are almost instantaneous.

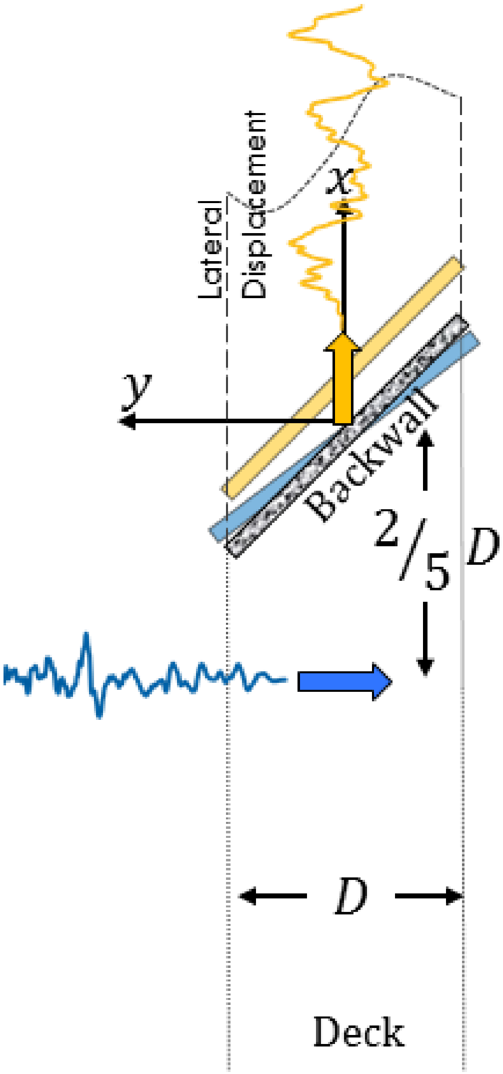

Fig. 5.18. Modeling a both lateral displacement and rotational excitation at the backwall.

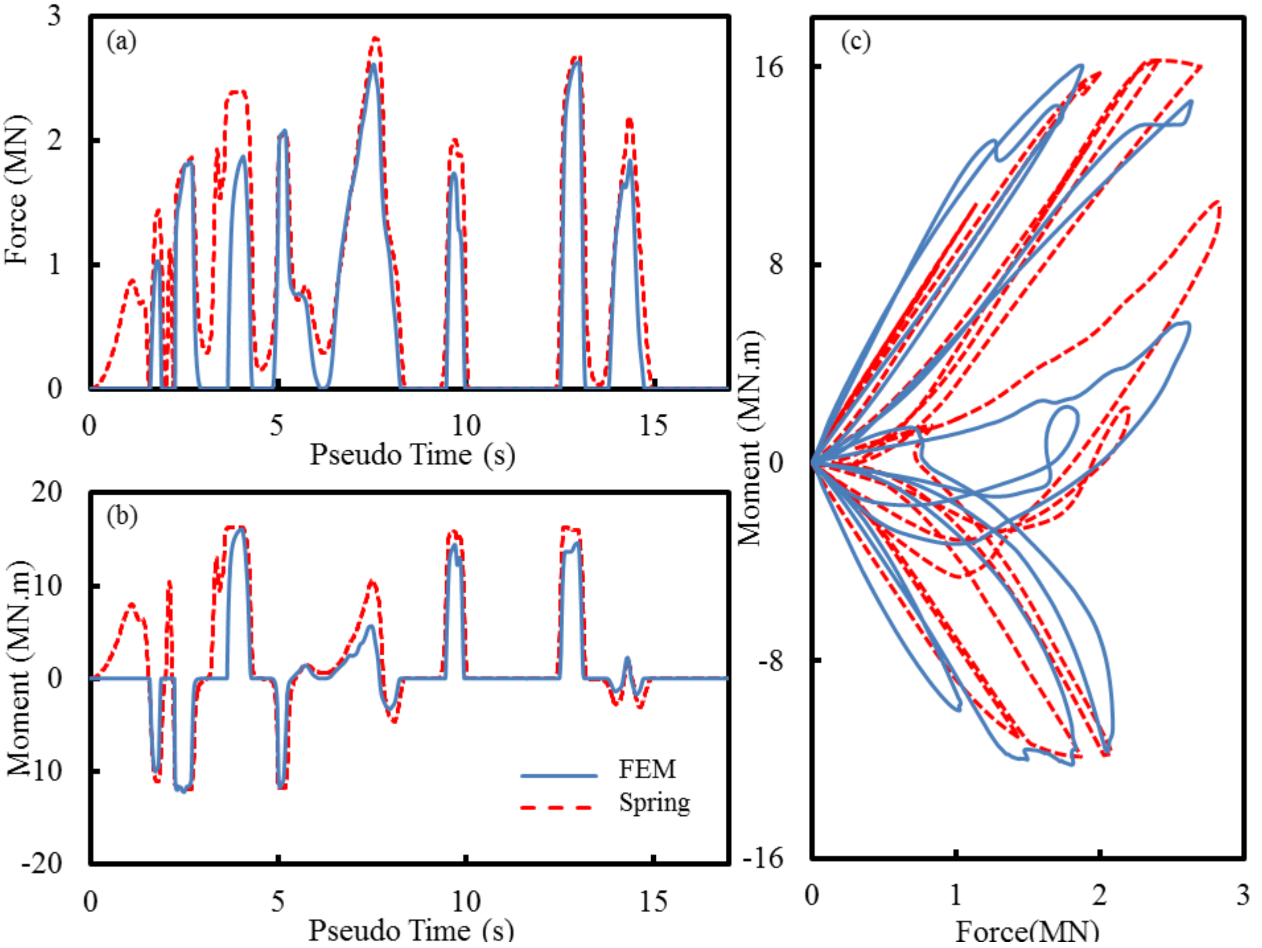

Fig. 5.19. A 45-degree skew wall with 30ft deck under EW El Centro for longitudinal displacement and 1/350 of the SN El Centro displacement as rotation. (a) Force reaction and (b) and Moment reactions vs. pseudo.

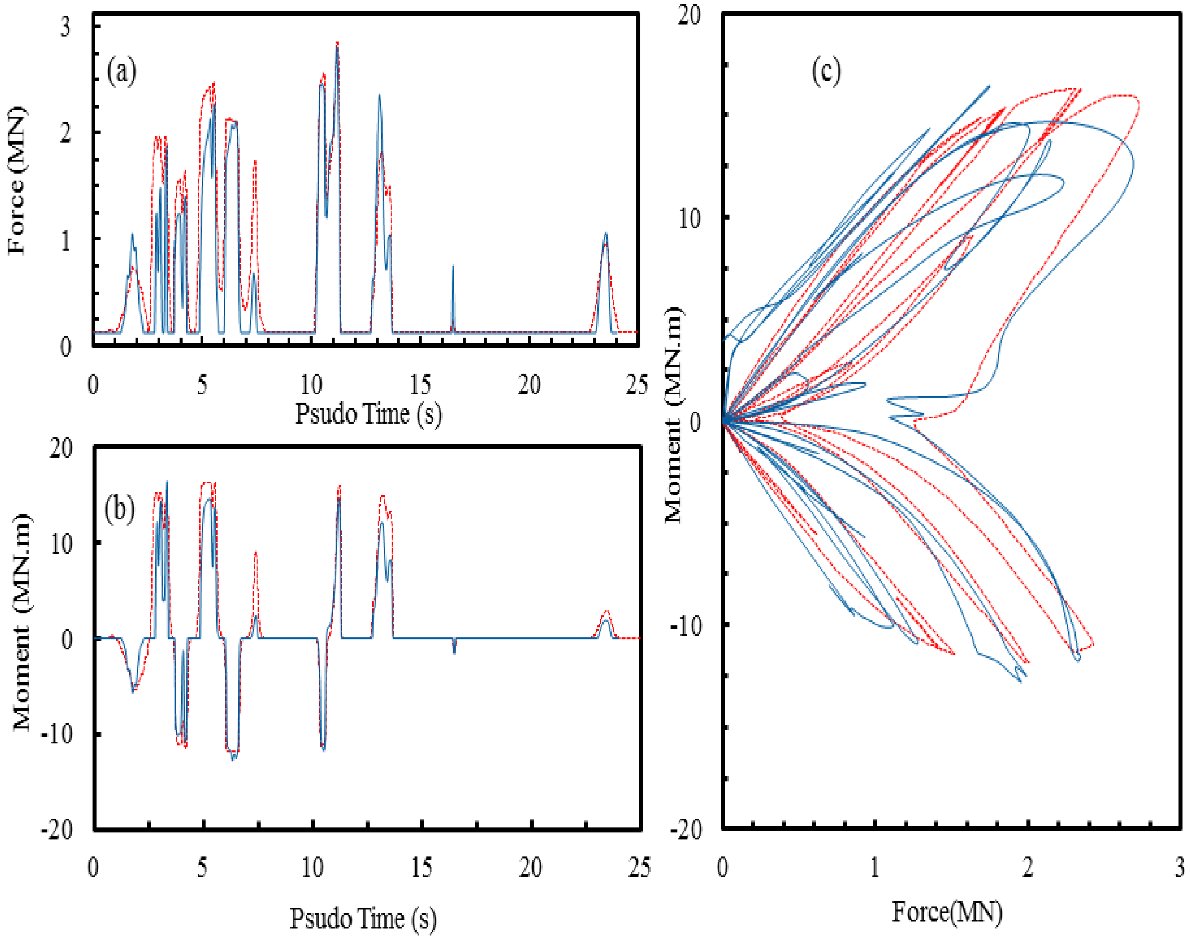

Fig. 5.20. A 45-degree skew wall with 30ft deck under Imperial Valley displacement for longitudinal displacement and 1/350 of the Kobe displacement as rotation: (a) Force reaction and (b) and moment versus force.

Chapter 6

Summary and Recommendations for Future Research

6. Summary and Recommendations

This study offered a method to solve for the reactions of skew bridge abutments in the form of a macroelement that accounts for the nonlinear contact-gapping between the backwall and the backfill and the backfill's highly inelastic behaviors. The entire set of reactions (lateral, transverse, and moment) is deduced from a knowledge of the lateral reaction and a phenomenological model of the distribution of pressures that form this lateral reaction. Given these, as well as the physical parameters of the abutment system, the transverse reaction and moment could be computed.

Two methods were offered for the calculation of the lateral reaction itself—these were, namely (*i*) an interpolation method (see, §4.1-§4.4) that produced the lateral reaction from that of a solution for a straight abutment, which could be obtained using a physically parameterized and (*ii*) a another regression-based model that was based on the observation that capacity-per-unit-wall-area exhibited a consistent variation for a broad range of skew angles when normalized by the capacity of a straight wall that has the same deck-width as the skew one (see, §5.4). Both methods were verified against detailed FE solutions and produced consistently accurate results.

In the macroelement model the distribution pattern of the stresses in the backfill was assumed to be linear where the slope was found to be primarily a function of the skew angle; however this study also identified that further investigation and quantification of this stress distribution would yield more accurate and general models.

Nevertheless, the resulting overall macroelement model was based, by-and-large, on physical parameters that included the backfill soil's internal friction angle and cohesion, backwall height, and skew angle. It was shown to accurately produce the normal and tangential reactions as well as the moment caused by the backwall movements under a large variety of adequately general displacement-controlled tests, in comparisons against results obtained using detailed FE models.

The model is computationally efficient compared to an FE model by several orders of magnitude—in that a macroelement model takes only a few seconds to produce results whereas nonlinear FE simulation involving soil plasticity and frictional contact takes hours. As such, the macroelement model is amenable to repetitive nonlinear time-history analyses required for performance-based seismic design.

Several research topics could be mentioned here to follow up with the present effort. These are:

- Implementation of the model into a general analysis package, such as OpenSees, and investigation of the response of bridges with skew abutments. While there have been studies in this area (see, for example, Kaviani et al. 2012, 2014), they were all based on heuristic models of the skew backfill behavior.

- Investigation of the effects of wingwalls on the overall behavior. While for large deck-widths, the wingwall contributions are deemed minor, for narrow abutments, these effects may not be negligible.
- Validation of the macroelement model through field- and/or laboratory testing. The only feasible (low-cost) approach to achieving this validation appears to be through hybrid testing wherein the two skew abutments of a bridge, and the bridge superstructure form the physical, and virtual portions of the test specimen, respectively.

Appendix: Matlab Codes

This appendix provides the reader with the Matlab codes for the macroelement described in Chapter 5.

```
clc; clear all; close all
tic

DeckWidth= 30*.3048      ; % Wall Width in m (example 30ft wall =30*0.3048)
WHeight  = 1.65          ; % Wall Height (example: to be 5.5 ft (1.67m))
alpha    = 45/ 180 * pi  ; % Skew Angle
miumax   = 0.35          ; % Maximum mobilizable Friction Angle

xNRMD    = 0:0.01:10     ; % xNRMD = Normalized x , xNRMD=x/x_max *10

% i= HALF the number of Integration Points 0:30  =>60 total Integration Points
% FNRMD  = C * xNRMD./(1+D*xNRMD);
FultUNIT = 2.2E6 /(15*.3048) ; % N/m*1m
cowar    = -0.8712*(alpha/pi)^2 + 0.0893 *(alpha/pi) + 1;

% Capacity Over Wall Area Ratio
% COWAR  = Capacity of Skew Wall over the Wall Area Normalized by that
% of the non-skew wall case with the same wall height

UnitWallStiffness = 4e8 / (15*.3048)    ;
IntegralPt =  200                       ;
ElemWid    =  DeckWidth / IntegralPt    ;
KElem    =  ElemWid * UnitWallStiffness ;
FultElm  =  ElemWid * FultUNIT * cowar  ;

[e,time] = DispDriver ()           ;% Applies Displacement Control loading by calling DispDriver

force    = zeros(1,size(e,2))      ;
Nforce   = zeros(1,size(e,2))      ;
mom      = zeros(1,size(e,2))      ;

theta    = e(2,:)                  ;
dis      = e(1,:)                  ;

plasd    = zeros(IntegralPt,size(e,2)) ;
GapElem  = zeros(IntegralPt,size(e,2)) ;

fElm     = zeros(IntegralPt,size(e,2)) ;
dfElm    = zeros(IntegralPt,size(e,2)) ;
NElem    = zeros(IntegralPt,size(e,2)) ;

miu      = zeros(1,size(e,2))          ;
fibx     = zeros(IntegralPt,1)         ;

    for i=1: IntegralPt
         fibx (i)  = ((ElemWid * (i-1/2) - DeckWidth/2) )   ;
          NArm(i)  = fibx(i)   / cos(alpha)                 ;
        WallWidth  = DeckWidth / cos(alpha)                 ;
         fibxnrm(i)= fibx(i)   / WallWidth                  ;
    end


[ KElemVar, FultElemVar ] = Stifness( alpha, KElem, FultElm, fibxnrm ) ;

% miu     = -0.35* ones (1,size(e,2))  ;
  miu     =  MiuFinder( e, DeckWidth, alpha, miumax  ) ;
  % This is the function that finds the appropriate Mu at every load increment.
```

```
  % This is based on the load scenario and the Maximum Friction coefficient between the
  % concrete backwall and the backfill soil (this should be
  % reported/obtained from lab experiments) and Deckwidth.

for t=1:size(e,2)-1

    for i=1: IntegralPt
        dispElm(i,t+1) = (tan(e(2,t+1)+alpha)-tan(alpha)) * fibx (i) + e(1,t+1) ;
        ddispsl(i,t+1) = dispElm(i,t+1)-dispElm(i,t) ;

         if  dispElm(i,t+1)< GapElem(i,t+1)  % if you want the gap be active
              fElm (i,t+1)=0 ;
             dplasd(i,t+1)=0 ;
         else
              dfElm (i,t+1) = KElemVar(i) *  ddispsl(i,t+1)   ;
               fElm (i,t+1) = fElm (i,t) + dfElm (i,t+1)     ;
             if fElm (i,t+1)>= FultElemVar(i)
                 fElm (i,t+1) = FultElemVar(i) ;
                 dplasd(i,t+1)=ddispsl(i,t+1)  ;
             else
                 dplasd(i,t+1)=0;
             end

             if fElm (i,t+1) < 0; fElm (i,t+1) = 0 ; end
             if dispElm(i,t+1)<0; fElm (i,t+1) = 0 ; end
         end

        NElem(i,t+1) = fElm(i,t+1) / (cos(alpha) - miu(t+1) * sin(alpha));

        force(t+1)     = force(t+1)  + fElm(i,t+1);
        Nforce(t+1)    = Nforce(t+1) + NElem(i,t+1);
        mom(t+1)       = mom(t+1)    + ( NElem(i,t+1) * NArm(i) );
        plasd(i,t+1)   = plasd(i,t)  + dplasd(i,t+1);
        GapElem(i,t+2) = plasd(i,t+1);

    end

% -----------------------   Live Deformation Monitor ----------------------
headway=(t+1)/size(e,2)*100;
LiveMonit( IntegralPt, DeckWidth, alpha , e(1,t+1) ,e(2,t+1), GapElem(:,t+2),...
                                                                 headway  )

%v = VideoWriter('KobeImperial.avi','Uncompressed AVI');
% -------------------------------------------------------------------------

end

dispAV=sum(dispElm,1)/IntegralPt ;

x=0:size(e,2)-1;

figure (2)
    subplot(2,1,1)
    plot( dispAV , force )
     xlabel('Displacement at Wall Center (m)')
     ylabel('Resultant Force (N)')
    subplot(2,1,2)
    plot( x , force )
     xlabel('Time')
     ylabel('Resultant Force (N)')

figure (3)
    subplot(2,1,1)
    plot( theta, mom ,'g')
     xlabel('Rotation (Rad.)')
     ylabel('Moment (N.m)')
    subplot(2,1,2)
```

```
    plot( x, mom, '-g')
     xlabel('Time')
     ylabel('Moment (N.m)')

figure (4)
    surf(dispElm)
     xlabel('Time Increment')
     ylabel('Elem#')
     zlabel('Elem Displacement')

figure (5)
    surf(fElm)
     xlabel('Time Increment')
     ylabel('Elem#')
     zlabel('Elem Reaction')

figure (6)
    plot(force, mom)
     xlabel('F_X')
     ylabel('Moment')

figure (7)
    plot(x, Nforce)
     xlabel('Time')
     ylabel('Normal Force')

figure (8)
    plot(force, Nforce)
     xlabel('F_X')
     ylabel('Normal Force')

figure (9)
    plot( dispAV , theta )
     xlabel('Displacement (m)')
     ylabel('Rotation (Rad.)')
toc
```

This is the function **`MiuFinder`**. Miu the the mobilized friction coefficient. This function takes the full loading scenario and the geometry of the wall—i.e., deck-width (DeckWidth) and the skew angle (alpha) as well as the maximum friction coefficient between the concrete surface of the backwall and the backfill soil, which is a parameter that can be obtained from field or laboratory tests.

```
function [ miu ] = MiuFinder( e , DeckWidth, alpha, miumax )
% MIU is the "Mobilized Friction Angle"
% The Mobilized Friction Angle between the abutment wall and the backfill
% miu = F_T/F_N
% _______________________________________________________________________ %
%%{

miu=-miumax * ones (1,size(e,2));

for iii=1:size(e,2)
    if e(2,iii)==0
     miu(iii)= -1/5*miumax*sin(2*alpha) ;
    else
     roo = e(1,:)/( tan(alpha+e(2,:))-tan(alpha));
     roN = roo / DeckWidth                      ;
     miu(iii) = miumax *( -sign(roo) * tanh(16*(alpha/pi)^2 *  ...
             (abs(roN))^0.5) + 1/5 *sin(2*alpha) )                  ;
    end
 end

end
```

This is the function **`DispDriver`**. It returns a 2 by n array for the displacement and rotation and a 1 by n vector for time associated with the motion vector. It does not need any input:

```
function [e,t] = DispDriver ()
% - - - - - - - - - - - - - - - - - - - - - - - - - - - - - - - - - - - - - %
%            This is a Library For Load combinations                        %
%
%
%
%                  Linear monotonic push;I'm pushing 10cm here.
%   t = 0.0 : 0.001 : 0.1;
%   e = zeros(2,size(t,2));    e(1,:) = t;   e(2,:)=0.0*pi/6*t;
%
%
%Linear monotonic Rotation;I'm Rotating -.03 Radiants
%(0.03 Rad CounterSkew here.
%           t = 0.0 : 0.00001 : 0.01;
%           e = zeros(2,size(t,2));    e(1,:) = 0.0*t;   e(2,:)=5*t;
%
                       % Sinusoidal Loading
%
%   t = 0.0 : 0.0025 : 0.1;
%   e = zeros(2,size(t,2));    e(1,:) = 5*t;   e(2,:)=10*pi/6*t.*sin(49*t);

%                     %  Push till failure and Then Rotation
%     t = 1 : 1 : 100 ;  e(1,1:50) = 0.07/50 * t(1:50) ; e(1, 51:100) = 0.07;
%                        e(2,1:50) = 0; e(2, 51:100) = pi/180*15/50*(t(51:100)-50);

%  et=[0,0;0.025,0;0.07,0;0.12,0;0.01,0;-0.01,0;-0.1,0;-0.15,0;-.05,0;.01,0]; e=et';
%  et=[0,0;0,0.025;0,0.07;0,0.12;0,0.01;0,-0.01;0,-0.1;0,-0.05;0,0.01];  e=et';
%   et=[0,0;0.01,0.025;.015,0.07;0.03,0.10;0.05,0.01;0.05,-0.01;.005,-0.07;.01,-0.05;0,0]; e=et';

%     t = 0.0 : 0.0250 : 5.0;  e(1,:) = 0.5*t./70 ; e(2,:) =10*t./10;

%
%     t = 0.0 : 0.001: 5.0;  e(1,:) =0.05*(5*t./(t+1)).*(.505+.50*cos(5*t))   ; e(2,:) =0*t;

%     t = 0.0 : 0.005 : 5.0;  e(1,:) = t./30 ; e(2,:) = t./20;

%     t = 0.0 : 0.0070 : 7.0;  e(1,:) = t./70+0.1* t.*cos(10*t); e(2,:) = 0.01*t.*sin(1*t);

%      t = 0.0 : 0.0070 : 7.0;  e(1,:) = 0.01*t.*(.505+.50*cos(10*t))  ; e(2,:) =
0.00175*t.*sin(10*t); % this is the analysis being run by ABAQUS as well
%      t = 0.0 : 0.0010 : 7.0;  e(1,:) = 0.01*t.*(.505+.50*cos(10*t))  ; e(2,:) =
0.00175*t.*sin(10*t);

% this is the analysis being run by ABAQUS as well for the most Skew models:
        t = 0.0 : 0.25 : 100.0  ;
        e(1,:) = 0.07*0.01*t.*(.505+.50*cos(0.21*t))  ;
        e(2,:) = 0.07*0.00175*t.*sin(0.21*t);

%      t = 0.0 : 0.001 : 7.0;  e(1,:) = 0.01*t.*(.405+.50*cos(10*t))  ; e(2,:) =
zeros(1,size(t,2)) ;

%     t = 0.0 : 0.001 : 7.0;  e(1,:) = zeros(1,size(t,2))            ; e(2,:) = -
0.00175*t.*sin(10*t); % ABAQUS  Pure Rotation test
%    t = 0.0 : 0.01 : 7.0;  e(1,:) = zeros(1,size(t,2))            ; e(2,:) = -
0.00100*t.*sin(2.5*t);

%      t = 0.0 : .1 : 100.0  ;   e(1,:) = 0.07*0.01*t.*(.505+.50*cos(7*0.035*t))  ; e(2,:) =
0.07*0.00175*t.*sin(7*0.035*t); % Skew Model Abaqus , this is the analysis being run by ABAQUS as
well for the most Skew models

%     t = 0.0 : .1 : 100.0   ;   e(1,:) = 0.07*0.01*t.*(.505+.50*cos(7*0.035*t))  ; e(2,:) = -
0.07*0.00175*t.*sin(7*0.035*t);
```

```
%      t = 0.0 : .5 : 100.0   ;   e(1,:) =21* 0.07*0.010*(t.^0.25).*(.505+.50*cos(7*0.014*t))  ;
e(2,:) =21* -0.07*0.0040*(t.^0.25).*sin(7*0.014*t);

%      t = 0.0 : 0.05 : 100.0   ;   e(1,:) =21* 0.07*0.010*(t.^0.25).*(.505+.50*cos(7*0.014*t))
; e(2,:) =21* -0.07*0.0040*(t.^0.25).*sin(7*0.014*t);


%      t = 0.0 : .1 : 100.0  ;   e(1,:) = 0.07*0.015*t.*(.505+.50*cos(7*0.035*t))  ; e(2,:) =
0.07*0.00175*t.*sin(7*0.035*t);

%      t = 0.0 : 0.00250 : 7.0;  e(1,:) = zeros(1,size(t,2))           ; e(2,:) = -
0.01000*t.*sin(10*t); % ABAQUS  Pure Rotation test/pushing more
%       t = 0.0 : 0.00010 : 7.0;  e(1,:) = zeros(1,size(t,2))           ; e(2,:) = -
0.01000*t.*sin(10*t);
%      t = 0.0 : 0.0010 : 10 ;  e(1,:) = 0.01*t.*(.25+.25*cos(100*t))  ; time=[0, e(2,:) =
interp1p(

%       t = 0.0 : 0.1 : 30 ;
%       tm=[0 , 2.5 , 5, 7.5] ; rot=[0 , .4 , 0, -0.4 ];    % This is a Loading simply ...
%       e(1,:) = zeros(1,size(t,2));  e(2,:) = interp1q (tm',rot',t') ;    % ...   and unloading
Rotation

%       t = 0.0 : 0.5 : 100 ;
%       td=[0, 50, 75, 90, 100]; dis=[0, 0, 0, 0, 0.07];
%       tm=[0 , 20 , 30, 45,50, 100] ; rot=[0 , .4 , 0, -0.4, 0, 0 ];
%       e(1,:) = interp1q (td',dis',t') ;  e(2,:) = interp1q (tm',rot',t') ;

%     t = 0.0 : 0.0070 : 7.0;  e(1,:) = 0.021*t.*(.32+.68*cos(10*t))  ; e(2,:) =
zeros(1,size(t,2));  %Only Push, Periodic
%     t = 0.0 : 0.0010 : 7.0;  e(1,:) = 0.01*t.*(.505+.50*cos(10*t))  ; e(2,:) =
zeros(1,size(t,2));
%     t = 0.0 : 0.025 : 10.0;  e(1,:) = 0.035*t.*(sin(1.5*t))         ; e(2,:) =
zeros(1,size(t,2));
%     t = 0.0 : 0.025 : 10.0;  e(1,:) = 0.035*(t+5.0).*(sin(5*t))     ; e(2,:) =
zeros(1,size(t,2));
%     t = 0.0 : 0.025 : 10.0;  e(1,:) = 0.032*(t+5.0).*(sin(.7*t))    ; e(2,:) =
zeros(1,size(t,2));

%    t = 0.0 : 0.025 : 10.0; e(1,:) = zeros(1,size(t,2)); e(2,:) = -0.0021*(t+10.0).*(sin(1.4*t))
;

%       t = 0.0 : 0.01 : 10.0;   e(1,:) = zeros(1,size(t,2))   ; e(2,:) = -0.0750 * sin(3*t); %
e(2,:) = -0.0021*t.*sin(3*t);
% ------------------------------------------------------------------------
%            t1=0:333     ; e1(1,:)=( -abs(t1-1000/6)+1000/6)*6/1000*0.03 ;
%            t2=333:666   ; e2(1,:)=( abs(t2-1000/3)-1000/3)*6/1000*.03   ;
%            t3=666:1000  ; e3(1,:)=( -abs(t3-5000/3)+1000/6)*6/1000*0.07 ;
%               for t=1:1000
%                   if t<1000/3
%                       e(1,t)=e1(1,t);
%                   end
%                   if t<=666 && t>333
%                       e(1,t)=e2(1,t-333);
%                   end
%                   if t>666
%                       e(1,t)=e3(1,t-666);
%                   end
%
%               end
%               e(2,t)=zeros(1,size(t,2));
% ------------------------------------------------------------------------
%  t = 0.0 : 0.0070 : 7.0;  e(1,:) = 0.01*t.*cos(10*t)   ; e(2,:) = 0.0018*t.*sin(10*t);
%  t = 0.0 : 0.0070 : 7.0;  e(1,:) = 0.01*t.*(cos(10*t))  ; e(2,:) = 0.00175*t.*sin(10*t);
%  t = 0.0 : 0.070 : 7.0;  e(1,:)=0.01*sin(1*t)       ; e(2,:)=0.01*t.*cos(1*t);

%  t = 0.0 : 0.0010 : 7.0;  e=0.01*t.*t.*sin(7*t);
%  t = 0.0 : 0.0070 : 7.0;  e=0.1*sin(t)+.15/7*t;
```

```
%  t = 0.0 : 0.0070 : 7.0;  e=0.05*sin(1.7*t)+.14/7*t;
%  t = 0.0 : 0.0001 : 0.25; e = 0.125 - abs( t - .1250 );
%  t1= 0.0 : 0.00005: 0.25; e1 = 0.125 - abs( t1 - .1250 );
%  t2= 0.25: 0.00005: 0.50; e2 = 0.125 - abs( t2 - .1250 );

%      ElCENTRO DISPLACEMENT (m) BaseLine Corrected
% disptest=textread('ElCentroCorrectDis.txt');
% t=0:0.01:(0.01*(size(disptest,1)-1));
% e(1,:) = -2 * disptest'      ;
% e(2,:) = 1/450 * e(1,:)      ;

%{
% SHOWING THE ULTIMATE SURFACE
t      = textread('TimeUltimateSurfaceFinding.txt');
dispm  = textread('DispUltimateSurfaceFinding.txt');
rotrad = textread('RotUltimateSurfaceFinding.txt') ;
e(1,:) = dispm'  ;
e(2,:) = -rotrad'  ;
%}

%{
t=0:0.01:21.25;  % Same Analysis as the one by Abaqus
dispcm = textread('ElCent270cm.txt');
rotcm  = textread('ElCent180cm.txt');
e(1,:) = 0.01 * dispcm(1:size(t,2))'  ;
e(2,:) = -1/350 * rotcm(1:size(t,2))'  ;
%}

%{
 dispm = textread('ImperialValleyDISPm.txt');
 rotRad  = textread('KobeRotationRad.txt');
t=0:0.01:size(dispm,1);  % Same Analysis as the one by Abaqus
e(1,:) = dispm'  ;
e(2,:) = rotRad'  ;
%}

% %      ElCENTRO DISPLACEMENT (m)
% disptest=textread('ElCentroDIS.txt')
% t=0:0.02:(0.02*(size(disptest,1)-1));
% % e(1,:) = -2 * disptest'      ;
% e(1,:) = -2 * disptest'      ;
% e(2,:) = 0.0 *t          ;
% %
%%{ SHOWING THE ULTIMATE SURFACE
%%}
End
```

This is the function **`LiveMonit`**. It provides the user a view of the progress in the analysis, as well as the deformed shape and plastic deformations in the backfill and the motion of the backwall.

```
function   [ ] = LiveMonit(SlcNum, WWidth, alpha, e1,e2 , GapVector, headway)
        xw     =  -WWidth/2:0.01:WWidth/2 ;
        yUnd   = (tan(alpha))* xw  ;

        exager = 50 ; % Deformation Exaggeration for illustration purposes

        xwgap  = -WWidth/2:WWidth/(SlcNum-1):WWidth/2 ;
        xgapt  = xwgap';
        deform = ( tan( e2 +alpha ) - tan(alpha) )* xgapt + e1 ;
        yUndG  = (tan(alpha))* xgapt  ;
        yExage = yUndG + exager * deform ;
        yGap   = yUndG + GapVector*exager ;

        figure (1)
        plot(xgapt,yExage)
        hold on
```

```
        plot(xgapt,yGap,'-.r')
        plot(xw,yUnd,'k')

        z=legend( [sprintf('Wall Motion, Progress =%.0f', headway) '%'],...
                   'Soil Plastic Deformation', 'Undeformed Shape',...
                                            'location','southeast' );
        title...
        (sprintf('Wall and Soil Motion, Exaggerated by a factor of =%u',...
                                                           exager) );
        hold off

end
```

This is the function **`Stiffness`**. It takes the skew angle, alpha, and procudes the element stiffness and strength.

```
function [ KSliceVar, FultSlcVar ] = Stiffness( alpha, KSlice, FultSLC, fibxnrm )
%STIFNESS Calculates the stiffness of the Slice
%        m = tan(alpha)     ;
        m = 2/3 * tan(alpha)     ;

    knorm = m * fibxnrm +1 ;
%  knorm     = ones(1,size(fibxnrm,2));
%    knorm = (0.5 * m * fibxnrm +1) ;  % ??? I have to find a better way to
%    :

%KSliceVar = KSlice * knorm ;
KSliceVar = .300 * KSlice * knorm ;

FultSlcVar= FultSLC* knorm ;

end
```

References

Abdel-Mohti A, Pekcan G (2008). Seismic response of skewed RC box-girder bridges. Earthq Eng Eng Vib, 7(4): 415-26.

ASTM Standard D155 (2009). *Standard Test Methods for Laboratory Compaction Characteristics of Soil Using Modified Effort*, ASTM International, West Conshohocken, PA.

Aviram A, Mackie KR, Stojadinović B (2008). Guidelines for nonlinear analysis of bridge structures in California. *PEER Report 2008/3*, Pacific Earthquake Engineering Research, Berkeley, US. 2008. (available online at http://peer.berkeley.edu/publications/peer_reports/reports_2008/reports_2008.html).

Bozorgzadeh A, Ashford SA, Restrepo JI (2006). Effect of backfill soil type on stiffness and ultimate capacity of bridge abutments: large-scale tests. 5th National Seismic Conference on Bridges and Highways, San Francisco, Paper No. B01; 2006.

Bozorgzadeh A, Megally S, Restrepo JI, Ashford SA (2006). Capacity evaluation of exterior sacrificial shear keys of bridge abutments. Journal of Bridge Engineering (ASCE), 11(5): 555-65.

Brinkgreve, R. B., and Broere, W. (2008). Plaxis 3D Foundation Manual v.2.2, The Netherland: Delft University of Technology and Plaxis.

Caltrans SDC (2010). *Caltrans Seismic Design Criteria version 1.6*. California Department of Transportation, Division of Engineering Services, Office of Structure Design, Sacramento, CA.

Caltrans SDC, ver. 1.6 (2010), Caltrans seismic design criteria version 1.6. California Department of Transportation, Sacramento.

Chatzigogos CT, Pecker A, Salencon J (2009). Macroelement modeling of shallow foundations, *Soil Dynamics and Earthquake Engineering*, 29, 765-781.

Cremer C, Pecker A, Davenne L (2001). Cyclic macro-element for soil–structure interaction: material and geometrical nonlinearities. Int J Num Anal Methods Geomech, 25, 1257–1284.

Cruz CA, Saiidi M (2010). Experimental and analytical seismic studies of a four-span bridge system with innovative materials. Technical Rep. No. CCEER-10-04, Center for Civil Engineering Earthquake Research, Nevada, Reno, US.

Dimitrakopoulos EG (2011). Seismic response analysis of skew bridges with pounding deck-abutment joints. Eng Struct, 33(3): 813-26.

Dubrova, GA (1963). Interaction of soil and structures. *Izd. Rechnoy Transport*, Moscow, USSR.

Duncan JM, Chin-Yung C (1970). Nonlinear analysis of stress and strain in soils. *Journal of the Soil Mechanics and Foundations Division* 96.5: 1629-1653.

Duncan, JM, and Chang CY (1970). Nonlinear analysis of stress and strain in soil. *J. Soil Mech. Found. Div., ASCE*, 96, 1629–1653.

Earth Mechanics (2005). Field Investigations Report for Abutment Backfill Characterization, Response Assessment of Bridge Systems-Seismic, Live, and Long Term Loads. *Report to Dept. of Structural Engineering, University of San Diego, La Jolla* (2005).

Gajan S, Kutter BL, Phalen JD, Hutchinson TC, Martin GR (2005). Centrifuge modeling of load–deformation behavior of rocking shallow foundations. Soil Dyn Earthquake Eng., 25, 773–283.

Ghobarah AA, Tso WK (1974). Seismic analysis of skewed highway bridges with intermediate supports. *Earthquake Eng Struct Dyn*, 2(3): 235-48.

Gottardi G, Houlsby GT, Butterfield R (1999). Plastic response of circular footings on sand under general planar loading. Geotechnique, 49(4), 453–69.

Japan Road Association (JRA). (1996). Design specification for highway bridges, *Part V: seismic design*, Tokyo, Japan.

Kalantari A, Amjadian M (2010). An approximate method for dynamic analysis of skewed highway bridges with continuous rigid deck. Eng Struct, 32(9): 2850-60.

Kapuskar M (2005). Field investigations report for abutment backfill characterization, response assessment of bridge systems—Seismic, live, and long term loads. *Earth Mechanics, Inc., Task 3, RTA Contract No. 59, Report to Dept. of Structural Engineering,* Univ. of California, San Diego, La Jolla, Calif.

Kaviani P, Zareian F, Taciroglu E (2012). Seismic behavior of reinforced concrete bridges with skew-angled abutments, *Engineering Structures*, 45, 137-150.

Kaviani P, Zareian F, Taciroglu E (2014). Performance-based seismic assessment of skewed bridges, PEER Report No. 2014/1, Pacific Earthquake Engineering Research Center, Berkeley, CA.

Kawashima K, Unjoh S, Hoshikuma J, Kosa K (2011). Damage of Bridges due to the 2010 Maule, Chile, Earthquake, *Journal of Earthquake Engineering*, 15: 1036-1068

Kawashima K, Unjoh S, Hoshikuma J, Kosa K. Damage of transportation facility due to 2010 Chile earthquake (April 5, 2010). Bridge Team Dispatched by Japan Society of Civil Engineers. 2010. (available online at http://peer.berkeley.edu/publications/chile_2010/reports_chile.html).

Khalili-Tehrani P, Taciroglu E, Shamsabadi A (2010). Backbone curves for passive lateral response of walls with homogeneous backfills. *Soil-Foundation-Structure Interaction, R.P. Orense, N. Chouw, N., and M. J. Pender, eds., University of Auckland, New Zealand, vol. 2, 149–154*.

Kotsoglou A, Pantazopoulou S (2010). Response simulation and seismic assessment of highway overcrossings, *Earthquake Engineering and Structural Dynamics*, 39(9), 991–1013.

Le Pape Y, Sieffert JG (2001). Application of thermodynamics to the global modelling of shallow foundations on frictional material. Int J Num Anal Methods Geomech, 25, 1140–377.

Mackie K, Stojadinovic B (2007). Performance-based seismic bridge design for damage and loss limit states, *Earthquake Engineering and Structural Dynamics*, 36(13), 1953-1971.

Mackie K, Wong J, Stojadinovic B (2008). Integrated probabilistic performance-based evaluation of benchmark reinforced concrete bridges. *Technical Report 2007/09*, Pacific Earthquake Engineering Research Center, University of California, Berkeley, CA.

Maragakis EA, Jennings PC (1987). Analytical models for the rigid body motions of skew bridges. *Earthquake Eng Struct Dyn*. 15(8): 923-44.

Martin CM, Houlsby GT (2000). Combined loading of spudcan foundations on clay: laboratory tests. Geotechnique, 50(4), 325–38.

Matlab: Users' manual (version 5.1) (1997). Mathworks, Inc., Natick, Mass.

McKenna F, Fenves GL, Scott MH (2000). Open system for earthquake engineering simulation. University of California Berkeley, California, <http://opensees.berkeley.edu>, Version 2.2.2.

Meng JY, Lui EM (2000). Seismic analysis and assessment of a skew highway bridge. *Eng Struct*. 22(11): 1433-52.

Meng JY, Lui EM (2002). Refined stick model for dynamic analysis of skew highway bridges. Journal of Bridge Engineering (ASCE), 7(3): 184-94.

Mitoulis S (2012). Seismic design of bridges with the participation of seat-type abutments, *Engineering Structures*, 44: 222-233.

NBI—National Bridge Inventory (2002). *Bridge Information System* http://www.fhwa.dot.gov/bridge/886nbi.htm (last accessed, July 2014).

Nova R, Montrasio L (1999). Settlements of shallow foundations on sand. Geotechnique, 41(2), 243–256.

Omrani R, Mobasher B, Liang X, Gunay S, Mosalam KM, Zareian F, Taciroglu E (2015). "Guidelines for Nonlinear Seismic Analysis of Ordinary Bridges: Version 2.0," Caltrans Final Report No. 15-65A0454.

Ovesen NK (1964). Anchor slabs, calculation methods, and model tests. *Danish Geotechnical Institute, Bulletin No. 16*, Copenhagen, Denmark.

Paolucci R (1997). Simplified evaluation of earthquake-induced permanent displacements of shallow foundations. J Earthquake Eng, 1(3), 563–79.

Paolucci R, Shirato M, Yilmaz MT (2007). Seismic behaviour of shallow foundations: shaking table experiments vs. numerical modelling. Earthquake Eng Struct Dyn.

Rollins K, Jessee S (2013). Passive force-deflection curves for skewed abutments. *J. Bridge Eng.*, 18(10), 1086-1094.

Rollins KM, Cole, RT (2006). Cyclic lateral load behavior of a pile cap and backfill. *J. Geotech. Geoenviron. Eng.*, 132(9), 1143–1153.

Romstad K, Kutter B, Maroney B, Vanderbilt E, Griggs M, Chai YH (1995). Experimental measurements of bridge abutment behavior. *Rep. No.* UCD-STR-95-1, Dept. of Civil and Environmental Engineering, University of California, Davis, CA.

Romstadt K, Kutter B, Maroney B, Vanderbilt E, Griggs M, Chai YH (1995). Experimental measurements of bridge abutment behavior. Report No UCD-STR-95-1, University of California Davis, Structural Engineering Group.

Rowe PW (1971). “Large scale laboratory model retaining wall apparatus.” *Proc., Roscoe Memorial Symp.*, Cambridge Univ., Cambridge, U.K., 441–449.

Schanz T, Vermeer PA, Bonnier PG (1999). “The hardening soil model—Formulation and verification.” *Proc. Plaxis Symp.: Beyond 2000 in Computational Geotechnics,* R. B. J. Brinkgreve, ed., Balkema, Rotterdam, The Netherlands, 281–296.

Shamsabadi A, Kapuskar M, Martin GM (2006a). Nonlinear seismic soil-abutment-structure interaction analysis of skewed bridges. 5th National Seismic Conference on Bridges and Highways, San Francisco, Paper No. B18.

Shamsabadi A, Kapuskar M, Zand A (2006b). Three-dimensional nonlinear finite element soil-abutment-structure interaction model for skewed bridges. 5th National Seismic Conference on Bridges and Highways, San Francisco, Paper No. B15.

Shamsabadi A, Khalili-Tehrani P, Stewart JP, Taciroglu E (2010). “Validated simulation models for lateral response of bridge abutments with typical backfills,” *ASCE J. of Bridge Eng.*, 15(3), 302-311.

Shamsabadi A, Rollins KM, Kapuskar M (2007). "Nonlinear soil-abutment-bridge structure interaction for seismic performance-based design." *ASCE J. Geotech. & Geoenv. Eng.*, 133(6), 707-720.

Shamsabadi A, Xu S, Taciroglu E (2013). “A generalized log-spiral-Rankine limit equilibrium model for seismic earth pressure analysis,” *Soil Dynamics and Earthq. Engineering,* 49:197–209.

Simo JC, Hughes TJR (1998). *Computational Inelasticity*. New York: Springer.

Stewart JP, Taciroglu E, Wallace JW, Ahlberg ER, Lemnitzer A, Rha CS, Khalili-Tehrani P, Keowen S, Nigbor RL, Salamanca A (2007). "Full scale cyclic testing of foundation support systems for highway bridges. Part II: Abutment backwalls," Report No. UCLA-SGEL 2007/02, Structural and Geotechnical Engineering Laboratory, University of California, Los Angeles.

Vermeer PA, Brinkgreve RBJ (1998). *Plaxis: Finite-element code for soil and rock analyses (version 7.1)*, Balkema, Rotterdam, The Netherlands.

Wakefield RR, Nazmy AS, Billington DP (1991). Analysis of seismic failure in skew RC bridge. Journal of Structural Engineering (ASCE), 117(3): 972-86.

Zakeri B, Padgett JE, Amiri GG (2014). Fragility analysis of skewed single-frame concrete box-girder bridges, *ASCE J. Performance of Constructed Facilities*, 28(3): 571-582.

Zareian F, Kaviani P, Taciroglu E (2015). Multi-phase performance assessment of seismic response of structures, *ASCE Journal of Structural Engineering*, 141(11): 04015041.